Full-wave Analysis of Large Conductor Systems over Substrate

by

Xin Hu

Submitted to the Department of Electrical Engineering and Computer Science
in partial fulfillment of the requirements for the degree of

Doctor of Philosophy in Electrical Engineering and Computer Science

at the

MASSACHUSETTS INSTITUTE OF TECHNOLOGY

January 2006
[February 2006]

Author .....
Department of Electrical Engineering and Computer Science
January 13, 2006

Certified by .....
Jacob K. White
Professor
Thesis Supervisor

Certified by .....
Luca Daniel
Assistant Professor
Thesis Supervisor

Accepted by .....
Arthur C. Smith
Chairman, Department Committee on Graduate Students

Full-wave Analysis of Large Conductor Systems over Substrate

by

Xin Hu

Submitted to the Department of Electrical Engineering and Computer Science
on January 13, 2005, in partial fulfillment of the
requirements for the degree of
Doctor of Philosophy in Electrical Engineering and Computer Science

Abstract

Designers of high-performance integrated circuits are paying ever-increasing attention to minimizing problems associated with interconnects such as noise, signal delay, crosstalk, etc., many of which are caused by the presence of a conductive substrate. The severity of these problems increases as integrated circuit clock frequencies rise into the multiple gigahertz range. In this thesis, a simulation tool is presented for the extraction of full-wave interconnect impedances in the presence of a conducting substrate. The substrate effects are accounted for through the use of full-wave layered Green's functions in a mixed-potential integral equation (MPIE) formulation. Particularly, the choice of implementation for the layered Green's function kernels motivates the development of accelerated techniques for both their 3D volume and 2D surface integrations, where each integration type can be reduced to a sum of 1D line integrals. In addition, a set of high-order, frequency-independent basis functions is developed with the ability to parameterize the frequency-dependent nature of the solution space, hence reducing the number of unknowns required to capture the interconnects' frequency-variant behavior. Moreover, a pre-corrected FFT acceleration technique, conventional for the treatment of scalar Green's function kernels, is extended in the solver to accommodate the dyadic Green's function kernels encountered in the substrate modeling problem. Overall, the integral-equation solver, combined with its numerous acceleration techniques, serves as a viable solution to full-wave substrate impedance extractions of large and complex interconnect structures.

Thesis Supervisor: Jacob K. White
Title: Professor

Thesis Supervisor: Luca Daniel
Title: Assistant Professor

Acknowledgments

Foremost I would like to acknowledge professor Jacob White and Professor Luca Daniel for their endless support and dedication. I consider myself extremely lucky to have two such wonderful advisors who have not only nurtured me intellectually, but also provided me with the confidence to face whatever challenges in life. I sincerely thank both for their effort to maximize my technical potentials and yet being completely supportive when I decided to pursue an alternative career. I would like to acknowledge Professor Michael Perrott as a reader on my thesis committee. I value his insightful advice and suggestions. I couldn't ask for a nicer or better member on my committee than Dr. Perrott.

I would like to acknowledge my lab mates: Jaydeep Bardhan, Bradley Bond, Carlos Pinto Coelho, Bo Kim, Tom Klemas, Shihhsien Kuo, Junghoon Lee, Tarek El Moselhy, Kin Cheong Sou, Dimitry Vasilyev, and Dave Willis. I also like to acknowledge our administrative assistant Chad Collins who is just amazing. I like to thank Kin for lending me his expertise in optimzation and Junghoon for assisting me in accelerated integration techniques as well as in pFFT. I appreciate the enthusiastic and extremely lively style with which Carlos participated in our discussions of the treatment of dyadic Green's functions in pFFT. Thank you all for the interesting discussions, the impromptu get-togethers, and the offers of friendship. I am especially grateful to my officemates for putting up with my seemingly incessant cell phone rings over the years.

I would like to thank Anne Vithayathil for always being there for me as a friend and being my partner in crime during many memorable occasions. I consider myself extremely lucky to have such a warm, generous and dependable person in my life. Another friend who immediately comes to mind is Jay Bardhan. His sense of humor, intense intellect and unique perspectives have definitely spiced up my daily life in the lab. I would like to thank Sara Su for being the best roommate ever. I cannot believe the patience with which she has tolerated all my foibles in the last two years. I am going to miss her and her pastry-making skills which have kept me very well fed.

I want to thank Chris LaFrieda for his endless encouragements, especially at times when I was ready to give up. I would not have made it through the Ph.D. program without him. His patience, humor and awesome personality are truly appreciated. I want to thank Alberto Ortega, Vikas Sharma, Dave Willis and Michele Dvorak for being such wonderful friends to me. I can always count on them for terrific advice, interesting conversations, or just cheering me up whenever I am down. I would also like to thank Merrie Ringel, who has been my friend since high school. Even though she is on west coast, the bond of our friendship is as strong as ever. Last but not least, I would like to thank my family. Without their love and support I would never be where I am today. I am deeply appreciative for all they have done for me. This thesis is dedicated to them.

Finally I would like to acknowledge the financial support from the National Department of Defense, the Intel Corporation, the MARCO Interconnect Focus Center and the Semiconductor Research Corporation.

Contents

List of Figures

Chapter 1

Introduction

1.1 Motivation

The integration of RF, analog and digital circuitry on a single integrated-circuit substrate, or system-on-chip (SoC), has become a popular solution for various mixed-signal applications. However, there are many challenges associated with this design paradigm where circuits of dissimilar nature, operating modes and functionality are integrated on a common substrate.

One of these challenges is to ensure the correct operations of all the SoC components in the presence of a conductive substrate. The semiconducting silicon substrate used in most SoC systems permits noise injection and propagation, thereby exposing circuitry to ubiquitous substrate noise coupling, leading to altered circuit performance and partial or complete loss of system functionality. The severity of the substrate effects only worsens as operating frequencies increase. For instance, the induced eddy currents in the substrate may degrade the quality factor of high-frequency RF inductors, thus leading to poor analog performance. Substrate noise plagues digital circuitry as well, severely impacting critical path delays [4].

In addition to substrate losses, conductor skin and proximity effects may impact current return paths in a network of closely-spaced conductors. Skin effect is manifested as the non-uniform distribution of current within individual conductors at high signal frequencies. This phenomenon occurs due to the fact that electro-

magnetic waves are attenuated as they penetrate a conductor's volume, resulting in current flows close to the material surface [3]. The thickness of this penetration depth is determined by signal frequency as well as material conductivity. A different cause of non-uniform current distribution between neighboring conductors is the proximity effect. Current flows through path of least impedance [3]. This implies that at low frequencies current distributes evenly across the entire cross-section of a conductor in order to minimize the dominating resistance. However, as frequency increases, the inductive contribution to the impedance dominates, leading to the minimization of loop inductance in order to reduce the overall impedance. Therefore current returns closer to the signal line at higher frequencies. Another area of problem is the occurrence of radiated electromagnetic interferences (EMI) in the SoC system, which transmits disturbances by means of propagation electromagnetic waves. In this case, distances between conductors are no longer insignificant in comparison to signal wavelength. For example, the on-chip power and ground wires of lengths comparable to the wavelength are potential sources of long-distance EMI emissions.

In order to avoid all the above problems in a circuit design, a simulation tool is needed that can accurately and efficiently extract full-wave conductor impedances in the presence of a conducting substrate. The solver described in this thesis accomplishes just that. In the solver, the substrate effect is accounted for through the use of the well-developed complex image theory [9, 14, 1, 28], which generates a set of closed-form, full-wave, 3D layered vector and scalar Green's functions for a two-layered medium. These layered media Green's functions are then incorporated into a mixed-potential integral equation (MPIE) formulation, as shall be explained in the body of this thesis, in order to compute the 3D vector and scalar conductor potentials. Since the substrate effect is already captured by the layered media Green's functions, the MPIE formulation performs 3D conductor impedance extraction without the need to discretize the substrate's volume or surface. In the MPIE formulation, the choice of the closed-form, full-wave layered media Green's function kernels motivates the development in this thesis of a set of novel, accelerated volume and surface integration schemes. These schemes reduce the 3D volume or 2D surface integrations of the lay-

ered media Green's function kernels to a sum of 1D line integrals. These techniques dramatically improve the efficiency of the solver, thus making the combination a viable approach to extracting full-wave substrate impedance of complex interconnect structures.

Moreover, a set of specialized high-order basis functions is developed in the context of the electromagnetic solver with the purpose of dramatically reducing the number of unknowns in comparison to the use of piecewise constant basis functions. At an ever increasing operating frequencies, using piecewise constant basis functions has proven to be computationally expensive for the accurate evaluation of conductor currents in the presence of frequency-dependent phenomenon such as skin and proximity effects. In this thesis, a procedure is presented in which a set of basis functions, unique to a conductor's cross-sectional geometry, is developed that parameterizes the frequency-dependent behavior of a conductor's cross-sectional current variation over a wide range of frequencies. This frequency-parameterizing nature allows the development of system matrices that are much reduced in size in comparison to that of piecewise constant basis functions. These higher-order basis functions themselves, however, are frequency-independent, therefore guaranteeing the following favorable conditions:

1 These basis functions do not complicate the volume integrations in a Galerkin technique for the solution of the MPIE. In fact, their use still permits the application of the aforementioned accelerated volume integration schemes.

2 These basis functions only need to be computed once for each conductor cross-section type for a given range of operating frequencies.

3 These basis functions are reusable with a minimal storage cost.

Overall, these frequency-independent basis functions promote the rapid and accurate simulation of any frequency-variant system.

The novel techniques developed in this thesis are implemented in an electromagnetic integral equation solver that extracts the impedance of any large and intricate conductor system in the presence of a substrate and over a wide range of frequencies.

A pre-corrected FFT (pFFT) scheme is incorporated into the Fastsub implementation with the purpose of accelerating matrix-vector products, which, when combined with an iterative method such as GMRES, is capable of achieving a solve cost of merely $O(n \log n)$, with n being the total number of system unknowns. The novelty of our pFFT scheme rests on the fact that it has been extended from the implementation of [84], which only accommodates scalar Green's function kernels, to the accommodation of dyadic Green's function kernels that are encountered in the substrate modeling problem of this thesis.

To summarize, novel contributions made by this thesis include: i.) the incorporation of layered Green's functions in the MPIE formulation to account for substrate effects; ii.) the development of accelerated volume and surface integration schemes involving full-wave Green's function kernels; iii.) the extension of pFFT method to accelerate the matrix-vector products involving dyadic Green's function kernels; and iv.) the development of specialized basis functions to minimize the number of unknowns needed to model the EM behavior of a conductor system.

1.2 Dissertation Outline

The body of this dissertation is organized as follows: Chapter 2 presents an overview of the different types of field solvers, including the MPIE, for the analysis of conductor systems. Chapter 3 provides a detailed derivation of the MPIE formulation with emphasis on the general construction of basis functions for the representation of current and charge densities of a conductor system. This chapter also contains a summary of the mesh analysis technique for the computation of current and charge density solutions of the MPIE. To account for substrate effect in the MPIE, Chapter 4 introduces the concept of vector and scalar potential layered Green's functions and derives their components in terms of semi-infinite Sommerfeld integrals. Subsequently, Chapter 5 approximates each one of these integrals based on the Complex Image Theory, according to which each integral can be expressed as a combination of analytical expressions referred to as images. Chapter 6 demonstrates how these

image approximations of the layered Green's functions can be numerically incorporated into the MPIE in order to provide solutions of conductor current and charge densities in the presence of a semi-conductive substrate. This chapter also seeks to enhance the usability of the MPIE solver by introducing a set of accelerated volume and surface integration schemes of the Green's function kernels in a Galerkin technique. Chapter 7 further enhances the efficiency of the solver by introducing a set of specialized basis functions that dramatically reduces the resulting system matrix size in comparison to the use of piecewise-constant basis functions. Chapter 8 highlights the implementation of a precorrected-FFT scheme, which, when combined with an iterative solver, is capable of reducing the computational complexity of solving the system involving dyadic Green's function kernels to $O(n \log n)$. Finally, examples are presented in Chapter 8 to validate the accuracy and efficiency of the numerous impedance extraction techniques outlined in this thesis.

Chapter 2

Background: Three-dimensional Field Solvers

In computational electromagnetic theory, field solutions for three-dimensional(3D) interconnect systems are obtained by solving some form of Maxwell equations. Analytical solutions of the Maxwell equations for simple or simplified interconnect geometry can be used when accuracy is less important than speed. However, when the configuration becomes complex and accuracy demands do not allow simplification, numerical solution of the appropriate form of Maxwell's equations must be employed.

2.1 Differential-equation vs. Integral-equation Methods

Many numerical methods have been developed in recent years for large interconnect structural analysis, and they can be broadly categorized into two approaches, one being differential-equation based and the other being integral-equation based.

Each Maxwell equation can be expressed in a differential form. The differential-equation based approach exploits this differential form by solving discretized versions of the Maxwell equations. Two of the most common approaches in this class are the Finite Difference Method (FDM) [46] and the Finite Elements Method (FEM) [69].

These methods require a mesh over the entire problem domain for the purpose of field quantity expansions. The versatility of these methods makes them advantageous for analysis of inhomogeneous materials. The resulting system matrices are large but sparse and can be solved by sparse linear solution methods such as the Conjugate Gradient algorithm [72]. However, one distinct disadvantage of FDM or FEM is that it is quite computationally expensive when dealing with open structures because it requires the discretization of the entire problem domain and the explicit truncation of unbounded regions.

For the material homogeneous (or piecewise homogenous) case, differential Maxwell equations can be rewritten as integral equations. This class of integral equation methods requires only the discretization of the sources of electromagentic field. Those sources can be physical quantities such as surface charge density or volume current density. A common approach in this class of methods is the Partial Element Equivalent Circuit (PEEC) Method [59]. The resulting system matrices from such methods are much smaller than those produced by differential-equation based methods, but they are dense. In recent years, many efforts [19, 34, 35, 51, 55, 68] have been focused on developing accelerated algorithms to solve systems with dense matrices. One particular development that has enjoyed much success in recent years is the combination of a Krylov subspace iterative technique with a precorrected-FFT [55] fast matrix-vector-product scheme, which, in most cases, achieves an almost linear order of complexity for both time and memory. Fortunately, the advantages of using these integral-equation based methods directly complement those of the differential-equation based approaches. Mainly, the integral-equation based approaches are much more efficient for the analysis of problems with homogenous materials and unbounded regions. For computational electromagnetic analysis of VLSI or analog circuits, one often encounters problems under these conditions. Therefore integral-equation based techniques are generally preferred.

2.2 PEEC Formulation: Volume vs. Surface

For the analysis of arbitrarily-shaped interconnects in VLSI or analog circuits, the PEEC method based on Mixed-Potential Integral Equation (MPIE) formulation has been extensively used. This formulation solves for unknown field quantities utilizing current and charge as state variables. More specifically, conductor surfaces are discretized into panels to capture charge accumulation or displacement current. Conductor volumes are discretized into filaments to capture conductor current and frequency-related effects such as skin and proximity effects. Details regarding the MPIE formulation can be found in the next chapter.

The volume based MPIE formulation seems to be suitable for the mixed simulation of electromagnetic and circuit behavior [13]. Surface integral equation formulations such as [18, 57, 84] have been developed to avoid the explicit discretization of the interior of conductors. However, these methods are plagued by problems of low-frequency system instability. Hence, for the sake of robustness and ease of implementation, a volume integral formulation is optimal for interconnect analysis.

Chapter 3

Background: Frequency-domain Integral Equation Formulation

In this chapter, a detailed derivation of the frequency-domain Mixed Potential Integral Equation (MPIE) formulation is presented and solved for the unknown current and charge densities in a large network of conductors. We start the derivation by introducing a set of differential equations for the potentials which are subsequently reformulated into integral forms using Green's theorem [37]. This mixed-potential integral equation formulation is then discretized to yield a system of linear equations. Finally, each physical quantity in the system is mapped to an element in an equivalent-circuit network, and mesh analysis is applied to solve for the system unknowns.

3.1 Potential Differential Equations

As with all computational electromagnetic theory, the starting point of our analysis, as developed in [32] for example, is the following set of Maxwell equations written in

the frequency domain:

$$\nabla \times \overline{H} = j\omega\epsilon\overline{E} + \overline{J} \tag{3.1}$$

$$\nabla \times \overline{E} = -j\omega\mu\overline{H} \tag{3.2}$$

$$\nabla \cdot \epsilon\overline{E} = \rho \tag{3.3}$$

$$\nabla \cdot \mu\overline{H} = 0, \tag{3.4}$$

where $\omega = 2\pi f$ is the temporal frequency, H and E are magnetic and electric fields, respectively, J and ρ are current density and charge density, respectively, ϵ is the dielectric constant, and μ is the magnetic permeability.

Equation(3.4) may be used to express magnetic field H in terms of magnetic vector potential A such that,

$$\overline{B} = \mu\overline{H} = \nabla \times \overline{A}. \tag{3.5}$$

Substituting (3.5) into (3.2) yields the following equation:

$$\nabla \times (\overline{E} + j\omega\overline{A}) = 0, \tag{3.6}$$

which is used to define the electric scalar potential ϕ as:

$$-\nabla\phi = \overline{E} + j\omega\overline{A}. \tag{3.7}$$

Equation (3.1) can thus be expressed in terms of state variables A and ϕ by substituting the relations defined in (3.5) and (3.7) for H and E, respectively. That is:

$$\nabla \times \nabla \times \overline{A} = j\omega\mu\epsilon(-\nabla\phi - j\omega\overline{A}) + \mu\overline{J}. \tag{3.8}$$

Using the Laplacian identity:

$$\nabla \times \nabla \times \overline{A} = \nabla(\nabla \cdot \overline{A}) - \nabla^2\overline{A} \tag{3.9}$$

and the Lorenz gauge:

$$\nabla \cdot \overline{A} = -j\omega\mu\epsilon\phi, \tag{3.10}$$

equation (3.8) is transformed to a Helmholtz equation relating current density J to vector potential A:

$$(\nabla^2 + \omega^2\mu\epsilon)\overline{A} = -\mu\overline{J}. \tag{3.11}$$

Similarly, (3.3) can be express in term of state variable ϕ using the relation in (3.7) and the Lorenz gauge in (3.10), thus yielding the following Helmholtz equation:

$$(\nabla^2 + \omega^2\mu\epsilon)\phi = -\frac{\rho}{\epsilon}, \tag{3.12}$$

which relates charge density ρ to scalar potential ϕ.

3.2 Green's Functions for the Potentials

The solution of the Helmholtz equation (3.11) for vector potential A can be constructed by introducing a dyadic Green's function G_A which, in turn, is the solution of another Helmholtz equation:

$$(\nabla^2 + \omega^2\mu\epsilon)\overline{\overline{G}}_A(r, r') = -\mu\overline{\overline{I}}\delta(r - r'), \tag{3.13}$$

where I is an unit dyad that can be represented by an unit diagonal matrix. In the above vector equation, G_A is a Green's function that characterizes the vector potential response at position r due to a current dipole excitation at r'. More specifically, x-, y- and z- directed dipoles at position r' contribute to each scalar potential component of $\overline{A}$, namely A_x, A_y, and A_z, at position r. By the principle of linearity, the general solution to (3.11) for the magnetic vector potential A at position r due to current density distribution J in a volume v can be written as

$$A(r) = \int_v \overline{\overline{G}}_A(r, r')\overline{J}(r')dr'. \tag{3.14}$$

Evidently the vector potential Green's function G_A is useful in expressing magnetic vector potential A in terms of its current sources.

By the same token, a Green's function for the scalar potential may be defined by the differential equation:

$$(\nabla^2 + \omega^2\mu\epsilon)G_\phi(r, r') = -\frac{\delta(r - r')}{\epsilon}. \tag{3.15}$$

The Green's function G_ϕ characterizes the scalar potential response at position r due to a point charge excitation at r'. Applying the concept of linearity again, the general solution to (3.12) for the electric scalar potential ϕ at position r due to charge distribution ρ on a surface s can be written as:

$$\int_s G_\phi(r, r')\rho(r')dr' = \phi(r). \tag{3.16}$$

In this case, the scalar potential Green's function G_ϕ expresses electric scalar potential ϕ in term of its surface charge source ρ.

In a homogenous medium where a dipole radiates in an unbounded space, a spatially-unbounded Green's function in the form of $\frac{e^{-jk|r-r'|}}{|r-r'|}$ can be used to capture potential fields due to source excitations, where k is a wave number defined as $k^2 = \omega^2\mu\epsilon$. However, if the field medium is not uniformly homogeneous due to the presence of layered materials such as a layered substrate, the solution can be modified by choosing the appropriate Green's function representations for G_A and G_ϕ. This topic shall be explored in depth in the next chapter.

3.3 Mixed-potential Integral Equation Formulation

For a system of conductors, the constitutive relation for the conductor electric field is $\overline{E} = \sigma\overline{J}$, where σ is the material conductivity. Substituting this constitutive relation and equation (3.14) into (3.7) yields the electric field integral equation in (3.17). The system of equations composed of (3.17), (3.18) which is the electrical scalar potential integral equation, (3.19) which ensures current conservation in the

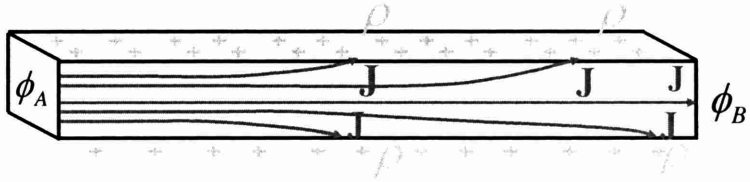

Figure 3-1: Structural distributions of current density J and charge density ρ [7].

interior of conductors, and (3.20) which ensures charge conservation on the surface of conductors, constitutes the entire MPIE formulation.

In summary, the set of integral equations (3.17)-(3.20) can be used to obtain the solutions of volume current density J and surface charge density ρ. Fig. 3-1 shows the volume and surface distributions of J and ρ, respectively, for a conductor structure.

$$\frac{\overline{J}(r)}{\sigma} + j\omega \int_V \overline{\overline{G}}_A(r,r')\overline{J}(r')dr' = -\nabla\phi(r) \tag{3.17}$$

$$\int_s G_\phi(r,r')\rho(r')dr' = \phi(r) \tag{3.18}$$

$$\nabla \cdot \overline{J}(r) = 0 \tag{3.19}$$

$$\hat{n} \cdot \overline{J}(r) = j\omega\rho(r), \tag{3.20}$$

where v and s are the union of conductor volumes and surfaces, respectively, and ϕ is the electric scalar potential on the conductor surfaces.

3.4 Discretization

To solve (3.17)-(3.20) numerically for the conductor-volume current density J and conductor-surface charge density ρ, one approximates each type of unknown by a weighted sum of a finite set of basis functions such that:

$$\overline{J}(r) \approx \sum_j \overline{m}_j(r) I_j \tag{3.21}$$

$$\rho(r) \approx \sum_m v_m(r) q_m, \tag{3.22}$$

where $m_j(r) \in C^3$ is a current density basis function, and I_j is its corresponding basis function weight. Similarly, $v_m(r) \in C$ and q_m respectively denote a charge density basis function and its weight.

A standard Galerkin technique [23] can then be used to generate a discrete system of equations for the weights. This technique entails the substitution of the basis function approximations of J (3.21) and ρ (3.22) into (3.17) and (3.18), respectively. The approximation error generated as a consequence of such substitution is then enforced to be orthogonal to the basis functions themselves, hence yielding:

$$\left\langle \frac{\sum_j \overline{m}_j(r) I_j}{\sigma} + j\omega \int_v \sum_j \overline{\overline{G}}_A(r,r') \overline{m}_j(r') I_j dr' + \nabla\phi(r), \overline{m}_i(r) \right\rangle = 0 \quad (3.23)$$

$$\left\langle \int_s \sum_m G_\phi(r,r') v_m(r') q_m dr' - \phi(r), v_\ell(r) \right\rangle = 0, \quad (3.24)$$

with the inner products defined as:

$$\left\langle \overline{f}(r), \overline{m}_i(r) \right\rangle = \int_v \overline{f}(r) \cdot \overline{m}_i(r) dr$$

$$\left\langle g(r), v_\ell(r) \right\rangle = \int_s g(r) v_\ell(r) dr,$$

where m_i and v_ℓ are current and charge density basis functions, respectively. Consequently the following matrix system of linear equations is obtained:

$$\begin{bmatrix} R + j\omega L & 0 \\ 0 & P \end{bmatrix} \begin{bmatrix} I \\ q \end{bmatrix} = \begin{bmatrix} V \\ V_\phi \end{bmatrix}, \quad (3.25)$$

where I and q are unknown vectors of current and charge density weights, respectively,

and

$$R_{ij} = \frac{1}{\sigma}\int_v \overline{m}_i(r)\cdot\overline{m}_j(r)dr \tag{3.26}$$

$$L_{ij} = \int_v\int_v \overline{\overline{G}}_A(r,r')\overline{m}_i(r)\cdot\overline{m}_j(r')dr'dr \tag{3.27}$$

$$P_{m\ell} = \int_s\int_s G_\phi(r,r')v_m(r)v_\ell(r')dr'dr \tag{3.28}$$

$$V_i = -\int_v \nabla\phi(r)\cdot\overline{m}_i(r)dr \tag{3.29}$$

$$V_{\phi_\ell} = \int_s \phi(r)v_\ell(r)dr. \tag{3.30}$$

A centroid-collocation technique [23] can also be used to generate a discrete system of equations for the weights. Both the Galerkin and the collocation methods produce a discretized system of equations by enforcing the difference between the actual and approximated solutions, or residual, to be orthogonal to a set of test functions. In the Galerkin method, these test functions are the same as the basis functions used to represent the unknowns. Hence, the Galerkin method seeks to minimize the average approximation error over the entire compact physical support of each basis function. On the other hand, the centroid-collocation method uses as test functions the centroids of the basis functions' physical supports. Thus the collocation method is typically less accurate than the Galerkin technique in that it minimizes the approximation error only at the centroid of each compact support.

3.4.1 Basis Functions for Current Density

To motivate the use of basis functions for the representation of current density J, consider that on an integrated circuit, the path taken by electric currents are usually very long and do not often form small closed loops. Therefore it becomes convenient if the computation of inductance can be broken down in such a way so that partial inductances can be associated to portions of a conducting loop without having to determine the loop path apriori. This introduces the concept of partial inductance [60] that defines a unique approach to the evaluation of open-loop inductance.

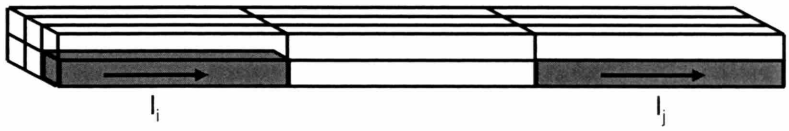

Figure 3-2: A conductor volume is discretized into thin filaments for the support of current density basis functions, where each basis function coefficient represents the total current through a filament.

To facilitate the application of partial inductance for a large system of conductors, the conductor volumes are discretized into N individually conducting filaments along their length and cross-sections. For each discretized filament of volume V_j and cross-sectional area a_j, a constant current I_j is assumed to flow length-wise in the direction of $\hat{l}_j = [l_x, l_y, l_z]$. This concept is illustrated in Fig. 3-2. For the sake of accuracy, discretization should be fine enough so that the resulting filaments are of appropriate dimensions restricted by wavelength as well as skin and proximity effects.

We can thus express the current density for all filaments by the collection of these constant filament currents as:

$$\overline{J}(r) = \sum_{j=1}^{N} \overline{m}_j(r) I_j,$$

where m_j is a current density basis function supported by the jth filament, and I_j is its corresponding coefficient. In addition, I_j is explicitly designated as the total current flowing through the jth filament. This explicit definition of I_j is necessary at the mesh analysis stage as shall be demonstrated in the next few sections. Therefore care must be taken to properly define basis function m_j so as to uphold the interpretation of basis coefficients as filament currents.

If piecewise-constant current density basis functions are used, then

$$\overline{m}_j(r) = \begin{cases} \frac{\hat{l}_j}{a_j} & \text{if } r \in V_j; \\ 0 & otherwise. \end{cases} \tag{3.31}$$

These piecewise-constant basis functions are normalized by cross-sectional area a_j so as to ensure that each basis function coefficient represents the actual filament current. On the other hand, if higher-order basis functions are used:

$$\overline{m}_j(r) = \begin{cases} \frac{W_j(r)\hat{l}_j}{\int_{a_j} W_j(r)dr} & \text{if } r \in V_j; \\ 0 & otherwise, \end{cases} \tag{3.32}$$

then basis function normalization by $\int_{a_j} W_j(r)dr$ is enforced for the same reason.

Respectively substituting the piecewise-constant and higher-order basis function representations into the first equation of the MPIE formulation (3.17) yields:

$$\sum_{j=1}^{N} \frac{\hat{l}_j I_j}{\sigma a_j} + j\omega \sum_{j=1}^{N} \frac{I_j}{a_j} \int_{V_j} \overline{\overline{G}}_A(r,r')\hat{l}_j dr' = -\nabla\phi(r) \tag{3.33}$$

for piecewise-constant basis functions, and

$$\sum_{j=1}^{N} \frac{W_j(r)\hat{l}_j I_j}{\sigma \int_{a_j} W_j(r)dr} + j\omega \sum_{j=1}^{N} \frac{I_j}{\int_{a_j} W_j(r)dr} \int_{V_j} \overline{\overline{G}}_A(r,r')W_j(r')\hat{l}_j dr' = -\nabla\phi(r) \tag{3.34}$$

for higher-order basis functions.

The Galerkin procedure outlined in (3.23)-(3.30) is then individually applied to (3.33) and (3.34) to generate a discrete linear system for the solution of the unknowns, producing

$$\left[\frac{\ell_i}{a_i\sigma}\right] I_i + j\omega \sum_j \left[\frac{1}{a_i a_j} \int_{V_i}\int_{V_j} \overline{\overline{G}}_A(r,r')\hat{l}_j \cdot \hat{l}_i dr' dr\right] I_j = \frac{1}{a_i}\int_{V_i} -\nabla\phi(r)\cdot\hat{l}_i dr \tag{3.35}$$

for piecewise-constant basis functions, and

$$\left[\frac{\int_{V_i} W_i^2(r)dr}{\sigma(\int_{a_i} W_i(r)dr)^2}\right] I_i + j\omega \sum_j \left[\frac{\int_{V_i}\int_{V_j} \overline{\overline{G}}_A(r,r')W_j(r)\hat{l}_j \cdot W_i(r')\hat{l}_i dr' dr}{\int_{a_j} W_j(r)dr \int_{a_i} W_i(r)dr}\right] I_j$$
$$= \frac{1}{\int_{a_i} W_i(r)dr}\int_{V_i} -\nabla\phi(r)\cdot W_i(r)\hat{l}_i dr \tag{3.36}$$

for higher-order basis functions. Equations (3.35) and (3.36) can be individually

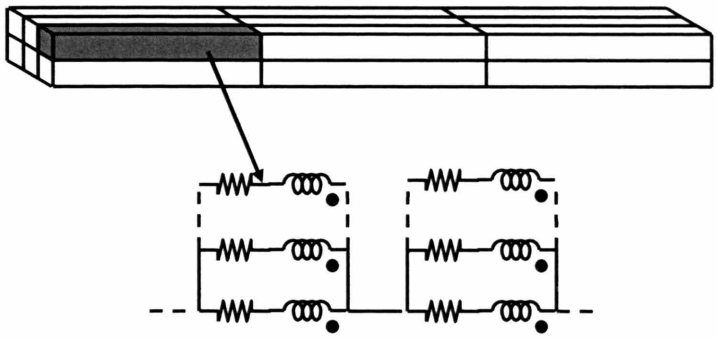

Figure 3-3: Each discretized conductor filament is modeled by a resistor in series with a group of partial inductors in an equivalent circuit network. Overall, the entire system of filaments can be mapped to a corresponding circuit topology.

casted into the general form:

$$R_{ii}I_i + j\omega \sum_j L_{ij}I_j = V_i, \tag{3.37}$$

where R_{ii} corresponds to the quantity in the first bracket of (3.35) or (3.36) and is an element of the resistance coefficient matrix R in (3.25) for the group of open wired segments. Similarly, L_{ij} in (3.37) corresponds to the second bracketed expression of (3.35) or (3.36) and is an entry of the partial inductance coefficient matrix L in (3.25). Finally V_i in (3.37) corresponds to the right-hand side expression of (3.35) or (3.36) and is an entry of the right-hand side vector in (3.25). From a physical perspective, (3.37) formulates the average voltage across a filament as a sum of voltages across a resistor and a series of inductors. Hence, the internal impedance of a filament can be represented by a resistive and an inductive effect as shown in Fig. 3-3.

3.4.2 Basis Functions for Charge Density

Consider the complex geometries typical of today's VLSI circuits, the calculation of capacitance on such conductor surfaces can be rather difficult. Using the partial capacitance technique [60] that is similar in concept to the partial inductance method,

one can replace the single conductor surface capacitance problem with a multi-surface problem for a set of simpler surfaces. These surfaces are obtained by discretizing the union of all conductor surfaces S into m rectangular panels of area S_m with the assumption that a constant charge resides on each panel. An example of such conductor surface discretization is shown in Fig. 3-4. The assumption of constant panel charge translates to the following condition:

$$q_m = \int_{S_m} \rho(r) dr. \tag{3.38}$$

Surface charge density can then be represented by the collection of such panel charges as defined in (3.22)

$$\rho(r) = \sum_m v_m(r) q_m.$$

If piecewise-constant basis functions are used:

$$v_m(r) = \begin{cases} \frac{1}{S_m} & \text{if } r \in S_m; \\ 0 & otherwise. \end{cases} \tag{3.39}$$

Alternatively, for higher-order basis functions:

$$v_m(r) = \begin{cases} \frac{u_m(r)}{\int_{S_m} u_m(r) dr} & \text{if } r \in S_m; \\ 0 & otherwise. \end{cases} \tag{3.40}$$

Basis function normalization by S_m in the piecewise constant case and by $\int_{S_m} u_m(r) dr$ in the higher order case is for the purpose of preserving the relationship between ρ and q so that basis function coefficients q_m have the definition of panel charge.

Respectively substituting the different basis function representations of charge into the MPIE equation (3.18) yields

$$\phi(r) = \sum_m \frac{q_m}{S_m} \int_{S_m} G_\phi(r, r') dr' \tag{3.41}$$

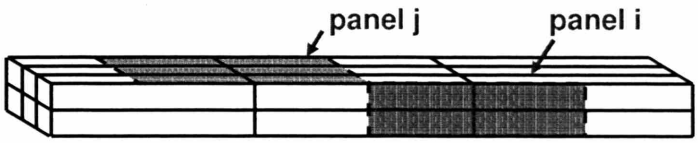

Figure 3-4: A conductor surface is discretized into panels so as to support current charge basis functions, where each basis function coefficient represents a panel charge [13].

for piecewise-constant basis functions, and

$$\phi(r) = \sum_m \frac{q_m}{\int_{S_m} u_m(r)dr} \int_{S_m} G_\phi(r, r')u_m(r')dr' \tag{3.42}$$

for higher-order basis functions.

The approach to produce a system of discrete linear equations for the unknown weights, or panel charges q_m, differs between piecewise-constant basis functions and higher-order basis functions. A centroid-collocation scheme is sufficient for (3.41) in order to produce a system with reasonable accuracy. For a single panel ℓ, this approach is equivalent to the computation of a point potential V_{ϕ_ℓ} at panel centroid r_ℓ due to a distribution of panel surface charge. More specifically,

$$V_{\phi_\ell} = \phi(r_\ell) = \left[\sum_m \frac{1}{S_m} \int_{S_m} G_\phi(r_\ell, r')dr' \right] q_m. \tag{3.43}$$

For the higher-order basis function representation in (3.42), a Galerkin technique can be applied to generate a system of equations for the unknowns. That is:

$$\begin{aligned} V_{\phi_\ell} &= \int_{S_\ell} \frac{u_\ell(r)}{\int_{S_\ell} u_\ell(r)} \phi(r)dr \\ &= \sum_m \left[\frac{1}{\int_{S_m} u_m(r)dr \int_{S_\ell} u_\ell(r)dr} \int_{S_\ell} \int_{S_m} G_\phi(r, r')u_\ell(r)u_m(r')dr'dr \right] q_m \end{aligned} \tag{3.44}$$

The quantity in bracket (3.43) or (3.44) forms an element in a potential coefficient matrix P. Equation (3.25) shows how matrix P fits into the overall matrix system

through the relation:

$$Pq = V_\phi, \tag{3.45}$$

where q is a vector of unknown panel charges, and V_ϕ is a vector of panel centroid potentials if piecewise-constant basis functions are used or a vector of average panel potentials if higher-order basis functions are used.

3.5 Branch Equation System Formation

After discretization, a system matrix equation is assembled with the unknowns being the filament currents in vector I and panel charges in vector q as shown in (3.25). In order to effectively map the problem into an equivalent-circuit network so as to facilitate the computation of the system unknowns, it is convenient to model surface charge accumulation q as displacement current I_p defined by the relation $I_p = j\omega q$. This yields the following modified matrix equation:

$$\begin{bmatrix} R + j\omega L & 0 \\ 0 & \frac{P}{j\omega} \end{bmatrix} \begin{bmatrix} I \\ I_p \end{bmatrix} = \begin{bmatrix} V \\ V_\phi \end{bmatrix}. \tag{3.46}$$

A system of branch equations can be established with each branch representing a physical filament or panel from the discretization of a conductor network. The impedance in a filament-type branch is represented by a resistor and several partial inductors or current-controlled voltage sources in series, while the impedance in a panel-type branch is modeled by a capacitor or several voltage-controlled current sources in parallel. An example of such equivalent-circuit mapping is shown in Fig. 3-5. The relationship between the branch impedance matrix Z_{em}, branch current vector I_b, and branch voltage vector V_b is given by

$$Z_{em} I_b = V_b, \tag{3.47}$$

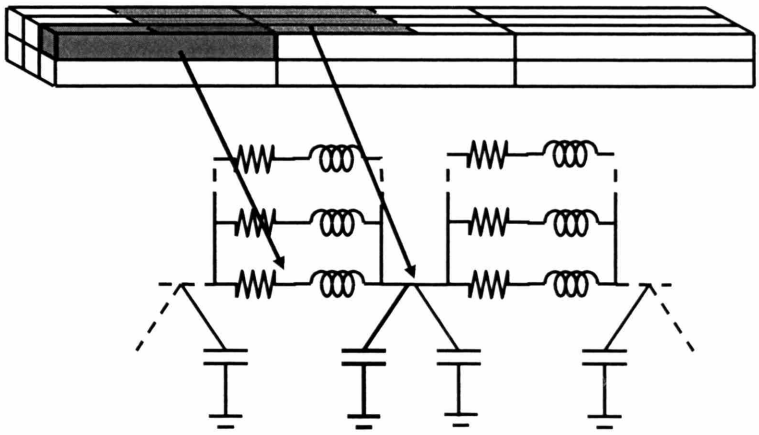

Figure 3-5: Mapping of discretized conductor filaments and panels to their respective circuit elements [13].

where

$$Z_{em} = \begin{bmatrix} R + j\omega L & 0 \\ 0 & \frac{P}{j\omega} \end{bmatrix}, I_b = \begin{bmatrix} I \\ I_p \end{bmatrix}, V_b = \begin{bmatrix} V \\ V_\phi \end{bmatrix}, \tag{3.48}$$

where I, I_p, V, and V_ϕ are all defined in (3.46). Conceptually, the system of equations in (3.46) can be considered to be effectively mapped to a circuit topology containing a network of resistors, inductors, capacitors, and voltage sources. Equations of dynamic fields are thus transformed by circuit theory into a circuit network with known solution algorithms. The following section attempts to explore one such algorithm in particular.

3.5.1 Mesh Analysis

Equations (3.17) and (3.18) have been shown to produce a linear system of branch equations. Equations (3.19) and (3.20) impose current and charge conservations on the MPIE, which, in circuit theory principle, correspond to the imposition of Kirchoff Voltage Law (KVL) on each closed loop in the equivalent circuit network or Kirchoff Current Law (KCL) at each node in the same network. If KVL analysis were applied

to the equivalent circuit, a set of loop currents, containing both displacement current and mesh current, becomes the new system unknown. The advantage of using these loop currents is the explicit guarantee of current conservation in the system. This also implicitly guarantees charge conservation when charge accumulation on the surface of the conductors is modeled as displacement current.

As KVL is applied to the closed-loop connection of branches shown in Fig ??, one needs to define a relationship between the voltage on each branch, V_b, to the voltage in a closed loop composed of that branch, V_m:

$$MV_b = V_m, \tag{3.49}$$

where the mesh matrix M of size $\#_{loops} \times \#_{branches}$ imposes KVL through each row of the M matrix, hence introducing mesh voltages in V_m for each closed loop in the network. Evidently both matrix M and vector V_m are sparse. In addition, according to the circuit network theory, the same mesh matrix M also maps each branch current in vector I_b to its corresponding mesh current in vector I_m through the relation:

$$I_b = M^T I_m. \tag{3.50}$$

Substituting (3.49) and (3.50) into (3.47) generates the following meshed system:

$$\left[MZ_{em}M^T\right] I_m = V_m, \tag{3.51}$$

where the system unknowns in I_b has been transformed to mesh currents in I_m.

Once vector I_m is determined by solving (3.51), one can easily determine branch currents and branch voltages using the relations:

$$I_b = M^T I_m \tag{3.52}$$

$$V_b = Z_{em} I_b, \tag{3.53}$$

which will in turn yield solutions for current density J and charge density ρ.

According to [58], mesh analysis yields a relatively stable discrete system at low frequencies. An essential requirement for maintaining numerical stability at very low frequencies is to keep inductive and capacitive contributions decoupled from each other. Mesh analysis accomplishes that by splitting loops into two sets where the first set is composed of inductive branches and the second set includes capacitive branches. In this context, the mesh analysis approach bears similarities to the "divergence-free" and "curl-free" basis functions as described in [58] where the divergence-free component of current responsible for magnetic field and the curl-free component responsible for the electric field are modeled independently so as to improve the stability of numerical solutions at low frequencies while maintaining solution accuracy.

3.5.2 Justification for Explicit Basis Function Normalization

The normalization in (3.32) and (3.40) complicates basis generation, but is essential if the resulting basis functions are used in a mesh analysis. This section establishes the necessity of such basis function normalization.

Branch-level Analysis

Given a matrix branch equation:

$$ZI_b = V_b, \tag{3.54}$$

where Z represents an impedance matrix obtained from normalized basis functions, and vector I_b contains the basis function weights that represent the physical currents carried by the basis functions. In contrast, consider the case where basis functions are not normalized. Hence the entries in vector $\tilde{I}_b$ are no longer physical branch currents, but are related to the branch currents through the relation:

$$I_b = N\tilde{I}_b, \tag{3.55}$$

where N is a diagonal matrix containing basis function normalization factors. Substituting (3.55) into (3.54) yields the following equation:

$$V_b = ZN\tilde{I}_b. \tag{3.56}$$

If we define $\tilde{Z} = ZN$, then $\tilde{Z}$ is effectively the impedance matrix obtained from the un-normalized basis functions. Equations (3.56) and (3.54) are thus equivalent:

$$\tilde{Z}\tilde{I}_b = ZI_b = V_b, \tag{3.57}$$

suggesting that normalization of basis functions is not necessary in branch analysis.

Mesh-level Analysis

In mesh analysis, the mesh current vector I_m is related to the physical branch current vector I_b by the relation:

$$I_b = M^T I_m. \tag{3.58}$$

To use mesh analysis for the un-normalized basis functions, there should be a similar relation of the form:

$$\tilde{I}_b = M^T \tilde{I}_m. \tag{3.59}$$

In an attempt to derive such a branch-mesh relation for the un-normalized basis functions, multiply (3.58) by N^{-1} on both sides yields:

$$\tilde{I}_b = N^{-1} I_b = N^{-1} M^T I_m. \tag{3.60}$$

Since N^{-1} does not commute in a non-square matrix multiplication, one can conclude that, in general, such $\tilde{I}_m$ doesn't exist. Therefore explicit basis function normalization is necessary if mesh analysis is applied to solve the discretized system.

Chapter 4

Background: Representation of Spatial-domain Layered Green's Functions

4.1 Introduction

In a VLSI or analog circuit, stratified media such as a layered substrate is ubiquitous. Therefore fields in stratified media have been a topic of intense study for many years, with numerous numerical techniques developed especially for the purpose of substrate analysis. Some of these techniques [61, 70, 15] use finite-element methods (FEM) to determine field solutions in the substrate, either by simulation of a 3D mesh of the substrate or by lumped-element circuit simulation. In [5, 63], substrate modeling is accomplished by applying finite-difference time-domain (FDTD) methods to a finely-discretized substrate, which can be quite computationally expensive. Moreover, integral-equation approaches such as the one used in [83] also requires the explicit discretization of a substrate volume. Alternatively, [66, 75, 20] utilize the more efficient boundary-element methods which only require the discretizzation of the surface of each layered region.

The most computationally efficient technique for the characterization of fields in a planar-stratified medium is the method of layered Green's functions which avoids the discretization of the substrate altogether. Instead, a set of pertinent Green's functions is

determined to capture the effect of the layered medium. These layered Green's functions are extremely versatile in that they can be easily integrated into any numerical technique such as an integral equation formulation to provide an efficient approach to interconnect modeling. Therefore, the construction of these multi-layered Green's functions has received frequent attention in literature, and numerous treatments have been proposed. The purpose of this chapter is to present a complete summary of the derivation of the layered Green's functions through a comprehensive survey of the recent literature on this topic.

As it is widely known, the Green's functions in the spatial domain do not generally exist in closed forms. Their spectral counterparts, obtained in the Fourier transform (spectral) domain, however, are readily available and can be derived in closed forms. In the spectral domain, the problem is equivalent to formulating the vertical dependence of the fields in the source region as a sum of vertically traveling TE and TM waves due to the reflections from the layer boundaries [67, 2, 76], and the field solutions at the observation layer can then be iteratively obtained based on the waves at the source layer. More generally formulated, the problem can be reduced to an equivalent transmission line network along the vertical direction for both TE and TM waves [45]. In this chapter, a detailed derivation of the layered Green's functions associated with arbitrarily-directed ($\hat{x}$, $\hat{y}$ or $\hat{z}$) electric source excitations is derived in the spectral domain for a half-space structure. The derivation is easily extensible to a medium with any number of planar layers.

Once all the spectral domain components have been determined,they should be transformed into the spatial domain using an inverse Fourier transform. In the context of layered media, this operation is often times referred to as Sommerfeld integrals. The integrals tend to be highly oscillatory, and hence, computationally expensive to evaluate. Two major evaluation approaches have been developed which include direct numerical algorithms with accelerated techniques for convergence [49, 26] and approximation of Sommerfeld integral kernels using Sommerfeld Identity [1]. In interconnect-analysis areas, the latter of the two methods is preferred for reasons as shall be explained.

4.2 Layered Green's Function Derivation Preliminaries

There exists a considerable amount of advantages to using the MPIE formulation for the field characterization of a layered medium. This is due to the fact that since the MPIE only involves the potential forms of the Green's functions as oppose to field forms, the Sommerfeld-type integrals of the Green's functions converge faster than those presented in any other form [22, 44]. Therefore, in our work, we are only concerned with the derivation of layered-medium magnetic vector potential Green's function G_A and layered-medium electric scalar potential Green's function G_ϕ.

We can now formulate a goal for our Green's function computation in view of its applicability to our interconnect analysis problem. Broadly speaking, we need to be able to obtain the potential field at observation point r given an elementary source with an arbitrary excitation located at point r'. Tailoring this understanding to our interconnect application, we see that the elementary sources of excitation are generated by conductor currents and charges in the topmost unbounded region of a multilayered structure as shown in Fig. 4-1. The substrate is modeled by all the subsequent layers. According to this framework, it is only logical to assume that each source excitation position denoted by r' is confined to the topmost region of the multilayered structure. Similarly, we are only interested in determining the potential fields created in the region where the interconnects reside. Therefore, the position of each observation location denoted by r is indigenous to the topmost region as well.

We will now provide a more detailed examination of the planar-layered medium in Fig. 4-1, whose properties of ϵ and μ vary along a normal direction taken as the z-coordinate. Coordinates x and y span a horizontal plane of the medium. As an aid to the proceeding computation, we shall first define free-space permittivity $\epsilon^0 \approx 8.85 \times 10^{-12}$ and free-space permeability $\mu^0 \approx 4\pi \times 10^{-7}$. Hence free-space wave-number becomes $k^0 = \omega\sqrt{\mu^0\epsilon^0}$. Now for an arbitrary layer i with conductivity σ_i, its complex permittivity $\hat{\epsilon}_i$ can be defined in relation to the free-space permittivity as:

$$\hat{\epsilon}_i = \frac{\epsilon_i}{\epsilon^0} = \epsilon_{r_i} - j\frac{\sigma_i}{\epsilon^0\omega}, \tag{4.1}$$

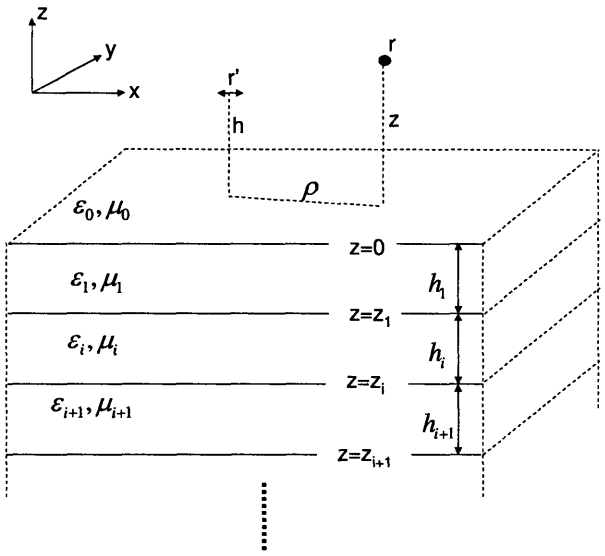

Figure 4-1: A source dipole and an evaluation point in the topmost layer of a multi-layered planar medium.

where ϵ_{r_i} is the relative permittivity for the ith homogenous medium. Using the assumption that $\mu_i = \mu^0$, the wave-number for the ith layer follows as:

$$k_i = \omega\sqrt{\mu_i \hat{\epsilon}_i \epsilon^0} = k^0\sqrt{\hat{\epsilon}_i}. \tag{4.2}$$

4.2.1 Boundary Conditions

The choice of components in the dyadic vector layered Green's function G_A, which directly effects the value of the scalar Green's function G_ϕ, is dictated by the boundary conditions between layers. That is, the planar-stratified medium introduces boundary conditions in the x-y planes located at $z = z_i$, where layer properties, ϵ_i and μ_i, vary across the interface as demonstrated in Fig. 4-1. Therefore boundary conditions must be enforced through the choice of components of the dyadic vector layered Green's function in order to guarantee field continuity. In general, the following set of continuity conditions must be enforced at

the interface between the ith and the $i+1$th layer interfaced at $z = z_i$:

$$\hat{n} \times (\overline{E}_{i+1} - \overline{E}_i) = 0 \tag{4.3}$$

$$\hat{n} \times (\overline{H}_{i+1} - \overline{H}_i) = \overline{J}_s \tag{4.4}$$

$$\hat{n} \cdot (\overline{B}_{i+1} - \overline{B}_i) = 0 \tag{4.5}$$

$$\hat{n} \cdot (\overline{D}_{i+1} - \overline{D}_i) = \rho_s, \tag{4.6}$$

where $\hat{n}$ is the normal surface vector, J_s is the electric surface current on the boundary, and ρ_s is the electric surface charge distribution. If there is no free charge or free current at the interface z_i, then:

$$\overline{E}_i^{\parallel} = \overline{E}_{i+1}^{\parallel} \tag{4.7}$$

$$\overline{H}_i^{\parallel} = \overline{H}_{i+1}^{\parallel} \tag{4.8}$$

$$\mu_i \overline{H}_i^{\perp} = \mu_{i+1} \overline{H}_{i+1}^{\perp} \tag{4.9}$$

$$\epsilon_i \overline{E}_i^{\perp} = \epsilon_{i+1} \overline{E}_{i+1}^{\perp}, \tag{4.10}$$

where $\parallel$ indicates field components parallel to the interface and $\perp$ indicates normal field components. Both E and H fields can be expressed in terms of vector potential A and scalar potential ϕ according to relations provided in (3.5) and (3.7), which are in turn related to G_A and G_ϕ, through (3.14) and (3.16), respectively. Hence the above boundary conditions can be used to derive the general forms of dyadic Green's function G_A and scalar Green's function G_ϕ as demonstrated in the next section.

4.2.2 Magnetic Vector Potential Layered Green's Function

Let G_{A_i} represent the dyadic Green's function in region i due to an unit-strength, arbitrarily-oriented current dipole in region j. Then the solution for this Green's function can be found by solving the set of inhomogeneous Helmholtz equation for each layer, subjected to the continuity conditions across the interfaces between layers. For example, consider a half-spaced problem in Fig. 4-2, consisting of two unbounded regions R_0 and R_1 interfaced at z=0. Assume that the source dipole is located in the topmost layer, then the set of Helmholtz

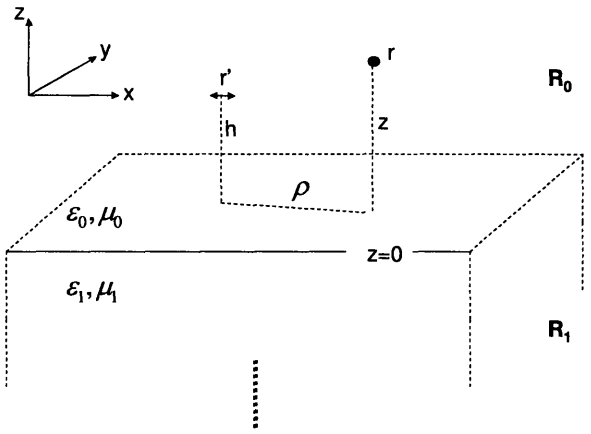

Figure 4-2: A source dipole and an evaluation point in a two-layered medium.

equations becomes:

$$r \in R_0 \quad : \quad (\nabla^2 + k_0^2)\overline{\overline{G}}_{A_0}(r, r') = -\mu_0 \overline{\overline{I}}\delta(r - r') \tag{4.11}$$

$$r \in R_1 \quad : \quad (\nabla^2 + k_1^2)\overline{\overline{G}}_{A_1}(r, r') = \overline{\overline{I}}0, \tag{4.12}$$

where k_i is defined by (4.2). Note that $\overline{\overline{I}}\delta(r - r')$ in (4.11) represents the unit-strength current generated by an arbitrarily-oriented dipole source located in R_0.

Boundary conditions (4.7)-(4.10) cannot be satisfied if we assume that vector potentials are strictly parallel to the orientation of source dipoles, meaning that the general form of the dyad G_A cannot be represented as a diagonal matrix. For a planar layered medium, there are actually several choices possible for the representation of G_A [44], all of which would satisfy the boundary conditions in (4.7)-(4.10). Depending on which form is selected, the value of the scalar Green's function G_ϕ is different. It is not surprising that both G_A and G_ϕ have multiple representations since the potentials themselves are not uniquely determined. As a matter of fact, if we define two quantities A' and ϕ' such that

$$\overline{A}' = \overline{A} + \nabla f \tag{4.13}$$

$$\phi' = \phi + j\omega f, \tag{4.14}$$

where f is a scalar function, then it is verifiable that the set A and ϕ produces the same

fields as the set A' and ϕ'. This condition is called gauge invariance. It is exactly due to gauge invariance that boundary conditions in (4.7)-(4.10) can be upheld for different combinations of G_A and G_ϕ. It has been proven in [44] that one particular combination, called the Sommerfeld choice [67], is much better suited than all others for the application of the MPIE. The Sommerfeld choice of G_A consists of:

$$\overline{\overline{G}}_A = \begin{bmatrix} G_A^{xx} & 0 & 0 \\ 0 & G_A^{yy} & 0 \\ G_A^{xz} & G_A^{yz} & G_A^{zz} \end{bmatrix}, \tag{4.15}$$

where a generic dyad element, G^{uv}, denotes the v-component of the field created by an u-directed unit source. Therefore, according to the above definition of G_A, a x-directed source dipole would generate a field G_A^{xx} in the x direction and a field G_A^{xz} in the z direction, a y-directed source dipole would generate a field G_A^{yy} in the y direction and a field G_A^{yz} in the z direction, and a z-directed dipole would generate a field G_A^{zz} in the z direction. Detailed derivation of these scalar Green's function components will be examined in the next few sections.

In addition, the following symmetry properties [50] apply to the components of G_A and are helpful in simplifying their subsequent mathematical manipulations:

- **Translational symmetry:**

  For a generic scalar component of a dyadic Green's function $\overline{\overline{G}}(r, r')$, where $r = (x, y, z)$ and $r' = (x', y', z')$, the layered medium is invariant along the x and y coordinates. Hence

  $$G\big((x, y, z), (x', y', z')\big) = G((x - x', y - y', z, z'). \tag{4.16}$$

- **Symmetry of revolution:**

  It is only necessary to obtained the fields created by a x-directed dipole and a z-directed dipole. The field crated by a y-directed dipole can be easily obtained from

those of a x-directed source using the following relations:

$$\begin{aligned} Let\ X &= x - x';\quad Y = y - y'; && (4.17)\\ G^{yy} &= G^{xx}\big(X \to Y; Y \to -X\big) && (4.18)\\ G^{yz} &= G^{xz}\big(X \to Y; Y \to -X\big). && (4.19) \end{aligned}$$

4.2.3 Electric Scalar Potential Layered Green's Function

Care must be taken when dealing with scalar potential Green's function G_ϕ. For instance, the Lorenz gauge in (3.10) between vector and scalar potentials does not hold between their Green's function counterparts, meaning that

$$G_\phi \neq -\frac{\nabla \cdot \overline{\overline{G}}_A}{j\omega\mu\epsilon}. \tag{4.20}$$

The following proof verifies the assertion in (4.20) and offers, instead, a relationship that is valid between the scalar and vector layered Green's functions. Rewriting the Lorenz gauge between the potentials yields:

$$\begin{aligned} \phi(r) &= \frac{j}{\omega\mu\epsilon}\nabla \cdot \overline{A}(r)\\ &= \frac{j}{\omega\mu\epsilon}\int \big(\nabla \cdot \overline{\overline{G}}_A(r,r')\big)\overline{J}(r')dr'. && (4.21) \end{aligned}$$

The scalar potential can also be expressed through the Green's theorem as shown in (3.16) where

$$\phi(r) = \int G_\phi(r,r')\rho(r')dr'.$$

Substituting the charge conservation equation in (3.20), where $\rho(r) = -\frac{1}{j\omega}\nabla \cdot \overline{J}(r)$, into the above equation for ρ yields an alternative solution for ϕ:

$$\begin{aligned} \phi(r) &= \frac{j}{\omega}\int G_\phi(r,r')\nabla \cdot \overline{J}(r')dr'\\ &= -\frac{j}{\omega}\int \big(\nabla' G_\phi(r,r')\big)\overline{J}(r')dr', && (4.22) \end{aligned}$$

where ∇' indicates a gradient operation with respect to r'. Equating the parenthesized

expressions in (4.21) and (4.22) engenders the following relationship [21]:

$$\nabla' G_\phi(r, r') = -\frac{1}{\mu\epsilon} \nabla \cdot \overline{\overline{G}}_A(r, r'). \tag{4.23}$$

In view of (4.23), an important conclusion can be drawn regarding the physical nature of the electric source excitation that produces G_ϕ. By the charge conservation law in (3.20), ϕ is defined as the potential associated with a unitary dipole. More specifically, ϕ is associated with the two separate charges of equal magnitude and opposite signs at the extremes of the unitary dipole. In contrast, G_ϕ is the potential associated with an isolated unit point charge, or a "quasi-dipole". Even though there readily exists a physical explanation for ϕ, there isn't one possible for G_ϕ, which is viewed as a contrived quantity purely for the sake of mathematical convenience.

Upon close examination of (4.23), one readily concludes that even though G_ϕ is a scalar quantity, it still has directional properties associated with the dipole it belongs to. Moreover, [44] has demonstrated that each choice of G_A, which, in our case is the Sommerfeld choice in (4.15), leads to an unique value of G_ϕ that varies for different orientation of source dipoles. For the Sommerfeld choice of G_A, the same scalar potential is generated by a $\hat{x}$- or $\hat{y}$-directed dipole source, but it differs from the potential generated by a $\hat{z}$-directed source. This observation will be further collaborated in a later section.

4.3 Sommerfeld Integrals

Due to the translational symmetry property of (4.16) exhibited by G_A along the x-y plane, it is convenient at this point to introduce the concept of a 2D Fourier transform [2] where

$$G(x - x', y - y') = \frac{1}{2\pi} \int_{-\infty}^{\infty} \int_{-\infty}^{\infty} \tilde{G}(k_x, k_y) e^{jk_x(x-x')} e^{jk_y(y-y')} dk_x dk_y \tag{4.24}$$

$$\tilde{G}(k_x, k_y) = \frac{1}{2\pi} \int_{-\infty}^{\infty} \int_{-\infty}^{\infty} G(x - x', y - y') e^{-jk_x(x-x')} e^{-jk_y(y-y')} dx dy. \tag{4.25}$$

In (4.24) and (4.25), the primed coordinate is associated with the position of a source dipole whereas the unprimed coordinate is associated with the position of an observation point. Quantity $\tilde{G}$ denotes the Fourier-domain or spectral-domain counterpart to the spatial quantity G. Values of k_x and k_y are taken as the x and y components, respectively, of the

propagation-wave vector $\hat{k}$ where

$$\hat{k} = \hat{x}k_x + \hat{y}k_y + \hat{z}k_z. \tag{4.26}$$

Incidentally, The magnitude of the propagation-wave vector can be written as the wave-number k:

$$k = \sqrt{k_x^2 + k_y^2 + k_z^2} = \frac{2\pi}{\lambda}, \tag{4.27}$$

where λ is the propagation wavelength.

Due to the apparent rotational symmetry around the z-axis, (4.24) can be simplified to a single integral in the cylindrical coordinate system in terms of spatial radial coordinate $\rho = \sqrt{(x-x')^2 + (y-y')^2}$ and spectral radial coordinate $k_\rho = \sqrt{k_x^2 + k_y^2}$ as:

$$G(\rho) = \int_0^\infty \tilde{G}(k_\rho) J_0(k_\rho \rho) k_\rho dk_\rho, \tag{4.28}$$

where J_0 is a 0th-order Bessel function. Equation (4.28) is known as a Sommerfeld integral that provides functional transformation from spectral to spatial domain. A more generalized form of the Sommerfeld integral [21] is defined as:

$$S_n[\tilde{G}(k_\rho)] = \int_0^\infty \tilde{G}(k_\rho) J_n(k_\rho \rho) k_\rho^{n+1} dk_\rho. \tag{4.29}$$

For a three-dimensional field possessing two-dimensional translational symmetry, Sommerfeld integral of (4.29) is used for the representation of the following 3D spatial-domain Green's function:

$$S_n[\tilde{G}(k_\rho, z, z')] = \int_0^\infty \tilde{G}(k_\rho, z, z') J_n(k_\rho \rho) k_\rho^{n+1} dk_\rho. \tag{4.30}$$

As a special case, consider that in the absence of a stratified medium, field of a dipole radiating in an unbounded space can be obtained from a Green's function in the form of: $\frac{e^{-jk|r-r'|}}{|r-r'|}$, where $|r-r'| = \sqrt{\rho^2 + (z-z')^2}$. The Fourier transformation of this spatially-unbounded Green's function is accomplished using the well known Sommerfeld Identity [37]:

$$\frac{e^{-jk|r-r'|}}{|r-r'|} = \int_0^\infty \frac{e^{-jk_z|z-z'|}}{jk_z} J_0(k_\rho \rho) k_\rho dk_\rho. \tag{4.31}$$

If the spectral quantity $\tilde{G}$ has a linear dependence on k_x or k_y, namely, $\tilde{G} = -jk_x\tilde{A}$ or $\tilde{G} = -jk_y\tilde{A}$, where $\tilde{A}$ has only kp, z, and z' dependence, then its transformation into the spatial domain corresponds to [21]:

$$-jk_x\tilde{A} \quad \longleftrightarrow \quad \frac{\partial A}{\partial x} \tag{4.32}$$

$$-jk_y\tilde{A} \quad \longleftrightarrow \quad \frac{\partial A}{\partial y}. \tag{4.33}$$

For example, if $\tilde{G} = -jk_x\tilde{A}$ so that in the spatial domain,

$$G(\rho, z, z') = \int_0^\infty -jk_x\tilde{A}(k_\rho, z, z')J_0(k_\rho\rho)k_\rho dk_\rho, \tag{4.34}$$

then the same spatial-domain response can be obtained by correspondingly apply a differential operation to the spatial quantity A:

$$\begin{aligned} G(\rho, z, z') &= \frac{\partial A(\rho, z, z')}{\partial x} && (4.35) \\ &= \frac{\partial}{\partial x}\left(\int_0^\infty \tilde{A}(k_\rho, z, z')J_0(k_\rho\rho)k_\rho dk_\rho\right) \\ &= -\int_0^\infty \tilde{A}(k_\rho, z, z')\frac{\partial(k_\rho\rho)}{\partial x}J_1(k_\rho\rho)k_\rho dk_\rho \\ &= -\cos\phi\int_0^\infty \tilde{A}(k_\rho, z, z')J_1(k_\rho\rho)k_\rho^2 dk_\rho, && (4.36) \end{aligned}$$

where ϕ is an angle between ρ and the x-axis, and J_1 is a 1st-order Bessel function. Similarly,

$$\tilde{G} = -jk_y\tilde{A} \iff G = -\sin\phi\int_0^\infty \tilde{A}(k_\rho, z, z')J_1(k_\rho\rho)k_\rho^2 dk_\rho. \tag{4.37}$$

Spectral domain	Spatial domain
$\tilde{G}$=$\tilde{A}$	G=$S_0[\tilde{A}]$
$\tilde{G}$=$-jk_x\tilde{A}$	G=$-\cos\phi S_1[\tilde{A}]$
$\tilde{G}$=$-jk_y\tilde{A}$	G=$-\sin\phi S_1[\tilde{A}]$

Table 4.1: Table of spatial-to-spectral domain transformations pertinent to the derivation of Green's functions for a half-space structure.

4.4 Component-by-component Derivation

In view of the preliminary information presented in Sec. 4.2, we now have all the resources at our disposal to derive the various scalar components of the dyadic vector potential layered Green's function in (4.15) and its associated scalar potential Green's function in (4.23). For the sake of illustration, all derivations in this section are demonstrated on the half-space structure in Fig. 4-2 where the source dipole is located in region R_0 above the plane of interface.

4.4.1 Derivation of G_A^{zz}

Consider a z-directed unit-strength source dipole located at $r' = (x', y', z')$ in region R_0. The resulting z-directed potential field at position $r = (x, y, z)$, which is denoted as $G_{A_0}^{zz}$ in region R_0 or $G_{A_1}^{zz}$ in region R_1, can be obtained by solving the following set of Helmholtz equations as simplified from (4.11) and (4.12):

$$r \in R_0 \;:\; (\nabla^2 + k_0^2) G_{A_0}^{zz}(\rho, z, z') = -\mu_0 \delta(x - x')\delta(y - y')\delta(z - z') \tag{4.38}$$

$$r \in R_1 \;:\; (\nabla^2 + k_1^2) G_{A_1}^{zz}(\rho, z, z') = 0. \tag{4.39}$$

This system is subjected to the following set of boundary conditions:

$$G_{A_0}^{zz} = G_{A_1}^{zz}\big|_{z=0} \tag{4.40}$$

$$\frac{1}{\epsilon_0}\frac{\partial G_{A_0}^{zz}}{\partial z} = \frac{1}{\epsilon_1}\frac{\partial G_{A_1}^{zz}}{\partial z}\bigg|_{z=0}, \tag{4.41}$$

which is obtained from the generalized boundary conditions (4.7)-(4.10) tailored to this specific case of source and field orientation.

In cylindrical coordinate system, the solutions to (4.38) and (4.39) are readily obtained as linear combinations of upward and downward-traveling waves in the form of $e^{\pm jk_{0z}} J_0(k_\rho \rho)$ as derived using the Fourier transformation introduced in Sec. 4.3. In fact, the general solution of field response in the ith layered medium [76] is written as:

$$G_{A_i}^{zz}(\rho, z, z') = \mu_i \int_0^\infty \left[a_i^{zz}(k_\rho, z')e^{-jk_{iz}z} + b_i^{zz}(k_\rho, z')e^{jk_{iz}z}\right] J_0(k_\rho\rho) k_\rho dk_\rho, \tag{4.42}$$

where a_i^{zz} and b_i^{zz} are the coefficients of upward and downward travelling waves in the ith

layer obtained by applying the appropriate boundary conditions [14].

Pertaining to the half-space example at hand, the particular field solution for region R_0 can be represented as a combination of [67]:

$$G_{A_0}^{zz} = G_0^p + G_0^s, \tag{4.43}$$

where G_0^p is the primary field generated by the source excitation in the absence of the layered boundary. Therefore field response G_0^p is just the spatially-unbounded Green's function defined in (4.31). Field G_0^s is generated as a secondary response by the primary field due to the presence of the layered medium. Moreover (4.43) can be casted into the form of (4.42) as:

$$G_{A_0}^{zz}(\rho, z, z') = \mu_0 \int_0^\infty \left[\frac{e^{-jk_{0z}|z-z'|}}{jk_{0z}} + a_0^{zz}(k_\rho, z') e^{-jk_{0z}z} \right] J_0(k_\rho \rho) k_\rho dk_\rho, \tag{4.44}$$

where the first bracketed term of (4.44) is the spectral-domain, spatially-unbounded Green's function, and the second term denotes the field of secondary waves generated by the source dipole and reflected in an upward direction from the boundary interface. In the absence of the source dipole in region R_1, the solution of $G_{A_1}^{zz}$ in (4.39) is written as:

$$G_{A_1}^{zz}(\rho, z, z') = \mu_0 \int_0^\infty b_1^{zz}(k_\rho, z') e^{jk_{1z}z} J_0(k_\rho \rho) k_\rho dk_\rho, \tag{4.45}$$

hence capturing the field of downward-travelling waves produced by the source dipole and transmitted into R_1. The two unknown quantities a_0^{zz} and b_1^{zz} can be solved by substituting (4.44) and (4.45) into boundary conditions (4.40) and (4.41) for $G_{A_0}^{zz}$ and $G_{A_1}^{zz}$. Consequently,

$$a_0^{zz}(k_\rho, z') = \frac{e^{-jk_{0z}z'}}{jk_{0z}} \tilde{R}_{TM}^{0,1} \tag{4.46}$$

$$b_1^{zz}(k_\rho, z') = \frac{e^{-jk_{0z}z'}}{jk_{0z}} \tilde{R}_{TM}^{1,0}, \tag{4.47}$$

where

$$\tilde{R}^{0,1}_{TM}(k_\rho) = \left(\frac{n^2 k_{0z} - k_{1z}}{n^2 k_{0z} + k_{1z}}\right) \tag{4.48}$$

$$\tilde{R}^{1,0}_{TM}(k_\rho) = \left(\frac{2n^2 k_{0z}}{n^2 k_{0z} + k_{1z}}\right) \tag{4.49}$$

$$n^2 = \frac{\hat{\epsilon}_1}{\hat{\epsilon}_0} \quad k_{0z} = \sqrt{k_0^2 - k_\rho^2} \quad k_{1z} = \sqrt{k_1^2 - k_\rho^2},$$

with $\tilde{R}$ being the generalized reflection coefficients [6] for which the subscript TE or TM represents the polarization of a wave, and the superscript $(i,i+1)$ or $(i,i\text{-}1)$ specifies a layer interface. For the sake of brevity, details concerning field solutions for region R_1 are omitted henceforth. They can, however, be easily derived from the field solutions of region R_0.

4.4.2 Derivation of G_A^{xx} and G_A^{yy}

Now consider a x-directed unit-strength source dipole located at $r' = (x', y', z')$ in region R_0. The generated potential field in the x-direction at position $r = (x, y, z)$, which is denoted as $G_{A_0}^{xx}$ in region R_0 or $G_{A_1}^{xx}$ in region R_1, is obtained by solving the following set of Helmholtz equations:

$$r \in R_0 \ : \ (\nabla^2 + k_0^2) G_{A_0}^{xx}(\rho, z, z') = -\mu_0 \delta(x - x')\delta(y - y')\delta(z - z') \tag{4.50}$$

$$r \in R_1 \ : \ (\nabla^2 + k_1^2) G_{A_1}^{xx}(\rho, z, z') = 0, \tag{4.51}$$

subjected to the boundary conditions:

$$G_{A_0}^{xx} = G_{A_1}^{xx}\big|_{z=0} \tag{4.52}$$

$$\frac{\partial G_{A_0}^{xx}}{\partial z} = \left.\frac{\partial G_{A_1}^{xx}}{\partial z}\right|_{z=0}. \tag{4.53}$$

Using a completely analogous procedure as in Sec. 4.4.1, the solution of $G_{A_0}^{xx}$ is in the form:

$$G_{A_0}^{xx}(\rho, z, z') = \mu_0 \int_0^\infty \left[\frac{e^{-jk_0|z-z'|}}{jk_{0z}} + a_0^{xx}(k_\rho, z')e^{-jk_{0z}z}\right] J_0(k_\rho \rho) k_\rho dk_\rho, \tag{4.54}$$

with

$$a_0^{xx}(k_\rho, z') = \frac{e^{-jk_{0z}z'}}{jk_{0z}}\tilde{R}_{TE}^{0,1} \tag{4.55}$$

$$\tilde{R}_{TE}^{0,1}(k_\rho) = \left(\frac{k_{0z} - k_{1z}}{k_{0z} + k_{1z}}\right). \tag{4.56}$$

Furthermore, due to the symmetry of revolution property in (4.18), we can easily conclude that:

$$G_{A_0}^{yy}(\rho, z, z') = G_{A_0}^{xx}(\rho, z, z'). \tag{4.57}$$

4.4.3 Derivation of G_A^{xz} and G_A^{yz}

Using the same x-directed source dipole as in Sec. 4.4.2, we are now interested in computing the z-directed potential field at observation point r. The following set of Helmholtz equations can be written that governs each one of the two half-space regions:

$$r \in R_0 \ : \ (\nabla^2 + k_0^2)G_{A_0}^{xz}(\rho, z, z') = 0 \tag{4.58}$$

$$r \in R_1 \ : \ (\nabla^2 + k_1^2)G_{A_1}^{xz}(\rho, z, z') = 0, \tag{4.59}$$

with the boundary conditions being:

$$G_{A_0}^{xz} = G_{A_1}^{xz}\big|_{z=0} \tag{4.60}$$

$$\frac{\partial(n^2 G_{A_0}^{xz} - G_{A_1}^{xz})}{\partial z} = \frac{\partial(G_{A_1}^{xx} - n^2 G_{A_0}^{xx})}{\partial x}. \tag{4.61}$$

It is worth noting that even though the x-oriented source dipole no longer directly affects the z-oriented field $G_{A_0}^{xz}$ in (4.58), the source dipole still bears an indirect effect on the field through boundary condition (4.61). In view of (4.58), it is evident that the spatially-unbounded Green's function associated with the source dipole is no longer needed as a part of the field solution of $G_{A_0}^{xz}$ as in the case of $G_{A_0}^{xx}$. The general set of solutions becomes:

$$G_{A_0}^{xz}(\rho, z, z') = \mu_0 \int_0^\infty a_0^{xz}(k_\rho, z')e^{-jk_{0z}z}J_0(k_\rho\rho)k_\rho dk_\rho \tag{4.62}$$

$$G_{A_1}^{xz}(\rho, z, z') = \mu_0 \int_0^\infty a_1^{xz}(k_\rho, z')e^{jk_{0z}z}J_0(k_\rho\rho)k_\rho dk_\rho. \tag{4.63}$$

Unknown quantities a_0^{xz} and a_1^{xz} are determined by substituting (4.62) and (4.63) into boundary conditions (4.60) and (4.61) for $G_{A_0}^{xz}$ and $G_{A_1}^{xz}$. Consequently,

$$a_0^{xz}(k_\rho, z') = -\frac{k_{0z}k_x}{k_\rho^2}\Big[- \tilde{R}_{TM}^{0,1} - \tilde{R}_{TE}^{0,1}\Big]\frac{e^{-jk_{0z}z'}}{jk_{0z}}, \tag{4.64}$$

where $\tilde{R}_{TM}^{0,1}$ and $\tilde{R}_{TE}^{0,1}$ are already defined in (4.48) and (4.56),respectively.

One perhaps immediately notices the k_x dependence in (4.64). Therefore the simplification defined in (4.36) can be applied to (4.64), producing an alternative representation where

$$\begin{aligned} G_{A_0}^{xz}(\rho, z, z') &= \frac{\partial}{\partial x}\Big[\mu_0 \int_0^\infty \frac{1}{k_\rho^2}\Big(\tilde{R}_{TM}^{0,1} + \tilde{R}_{TE}^{0,1}\Big)e^{-jk_{0z}(z+z')}J_0(k_\rho\rho)k_\rho dk_\rho\Big] \\ &= -\mu_0 \cos\phi \int_0^\infty \Big(\tilde{R}_{TM}^{0,1} + \tilde{R}_{TE}^{0,1}\Big)e^{-jk_{0z}(z+z')}J_1(k_\rho\rho)dk_\rho. \end{aligned} \tag{4.65}$$

Furthermore, due to the symmetry of revolution property in (4.19), one can conclude by (4.37) that:

$$\begin{aligned} G_{A_0}^{yz}(\rho, z, z') &= \mu_0 \int_0^\infty -\frac{1}{k_{0z}}\frac{k_{0z}k_y}{k_\rho^2}\Big(- \tilde{R}_{TM}^{0,1} - \tilde{R}_{TE}^{0,1}\Big)e^{-jk_{0z}(z+z')}J_0(k_\rho\rho)k_\rho dk_\rho \quad (4.66) \\ &= -\mu_0 \sin\phi \int_0^\infty \Big(\tilde{R}_{TM}^{0,1} + \tilde{R}_{TE}^{0,1}\Big)e^{-jk_{0z}(z+z')}J_1(k_\rho\rho)dk_\rho. \quad (4.67) \end{aligned}$$

4.4.4 Scalar Potential Layered Green's Functions

According to (4.23), the relationship between the dyadic vector layered Green's function and the scalar layered Green's function is:

$$\nabla' G_\phi(r, r') = -\frac{1}{\mu\epsilon}\nabla \cdot \overline{\overline{G}}_A(r, r').$$

Now that the various components of the dyadic Green's function are known, the above relationship enables us to derive the scalar layered Green's function. After equating, component by component, the right- and left-hand sides of (4.23), one can draw the following conclusions:

- For a z-directed dipole:

$$\frac{\partial G_\phi}{\partial z'} = -\frac{1}{\mu\epsilon}\frac{\partial G_A^{zz}}{\partial z}. \tag{4.68}$$

- For a x-directed dipole:

$$\frac{\partial G_\phi}{\partial x'} = -\frac{1}{\mu\epsilon}\left(\frac{\partial G_A^{xx}}{\partial x} + \frac{\partial G_A^{xz}}{\partial z}\right). \tag{4.69}$$

- For a y-directed dipole:

$$\frac{\partial G_\phi}{\partial y'} = -\frac{1}{\mu\epsilon}\left(\frac{\partial G_A^{yy}}{\partial y} + \frac{\partial G_A^{yz}}{\partial z}\right). \tag{4.70}$$

Upon close inspection, one notices that the scalar potential field created by a x-directed dipole in (4.69) is exactly the same as that created by a y-directed dipole in (4.70). Thus there exists only two different types of scalar layered Green's functions, G_ϕ^v and G_ϕ^h, each is respectively associated to a vertically or a horizontally-oriented dipole.

Derivation of scalar Green's function G_ϕ^v

From (4.68), the scalar layered Green's function $G_{\phi_0}^v$ for a vertical dipole in region R_0 can be readily obtained as:

$$G_{\phi_0}^v = -\frac{1}{\mu_0\epsilon_0}\int \frac{\partial G_{A_0}^{zz}}{\partial z}dz' = -\frac{1}{\mu_0\epsilon_0}\int\int_0^\infty \frac{\partial \tilde{G}_A^{zz}}{\partial z}J_0(k_\rho\rho)k_\rho dk_\rho dz'. \tag{4.71}$$

Substituting $\tilde{G}_{A_0}^{zz}$, which is the expression in the bracket of (4.44), into (4.71) one obtains:

$$G_{\phi_0}^v(\rho,z,z') = \frac{1}{\epsilon_0}\left(\frac{e^{-jk_0R}}{R} - \int_0^\infty \frac{1}{jk_{0z}}\tilde{R}_{TM}^{0,1}e^{-jk_{0z}(z+z')}J_0(k_\rho\rho)k_\rho dk_\rho\right), \tag{4.72}$$

where R=$\sqrt{p^2+(z-z')^2}$, and $\tilde{R}_{TM}^{0,1}$ is already defined in (4.48).

Derivation of scalar Green's function G_ϕ^h

Let's first provide two more spatial-to-spectral domain correspondences, namely,

$$\frac{\partial}{\partial x'} \longleftrightarrow jk_x \tag{4.73}$$

$$\frac{\partial}{\partial x} \longleftrightarrow -jk_x. \tag{4.74}$$

Hence, the following relationship holds for (4.69) in the spectral domain:

$$\begin{aligned} jk_x\tilde{G}_\phi^h &= -\frac{1}{\mu\epsilon}\left(-jk_x\tilde{G}_A^{xx}+\frac{\partial\tilde{G}_A^{zz}}{\partial z}\right) \\ \tilde{G}_\phi^h &= \frac{1}{\mu\epsilon}\left(\tilde{G}_A^{xx}-\frac{1}{jk_x}\frac{\partial\tilde{G}_A^{zz}}{\partial z}\right). \end{aligned} \tag{4.75}$$

Therefore, the spatial-domain representation of the scalar layered Green's function associated to a horizontal dipole in region R_0 becomes:

$$\begin{aligned} G_{\phi_0}^h(k_\rho,z,z') &= \frac{1}{\mu_0\epsilon_0}\int_0^\infty\left(\tilde{G}_{A_0}^{xx}-\frac{1}{jk_x}\frac{\partial\tilde{G}_{A_0}^{zz}}{\partial z}\right)J_0(k_\rho\rho)k_\rho dk_\rho \\ &= \frac{1}{\epsilon_0}\left(\frac{e^{-jk_0R}}{R}+\right. \\ &\quad \left.\int_0^\infty\frac{1}{jk_{0z}}\frac{k_{0z}^2\tilde{R}_{TM}^{01}+k_0^2\tilde{R}_{TE}^{01}}{k_\rho^2}e^{-jk_{0z}(z+z')}J_0(k_\rho\rho)k_\rho dk_\rho\right), \end{aligned} \tag{4.76}$$

where the spectral functions $\tilde{G}_{A_0}^{xx}$ and $\tilde{G}_{A_0}^{zz}$ are the expressions in the brackets of (4.54) and (4.44), respectively. Quantities $\tilde{R}_{TM}^{01}$ and $\tilde{R}_{TE}^{01}$ are defined in (4.48) and (4.56), respectively.

4.4.5 Sectional Summary

This section provides a succinct summary of the spectral-domain Green's functions for the source layer, which, according to our assumption, is the topmost unbounded region of a multilayered structure as shown in Fig. 4-1. The field evaluation region is also confined to the same topmost layer. For a x-, y-, and z-oriented electric dipole embedded in this layer, the following spectral-domain Green's functions are obtained:

- z-oriented dipole:

$$\begin{aligned} \tilde{G}_{A_0}^{zz} &= \frac{\mu_0}{jk_{0z}}\left[e^{-jk_{0z}|z-z'|}+a_{zz}e^{-jk_{0z}z}\right] \\ \tilde{G}_{\phi_0}^{z} &= \tilde{G}_{\phi_0}^{v}=\frac{1}{\epsilon_0 jk_{0z}}\left[e^{-jk_{0z}|z-z'|}+a_v e^{-jk_{0z}z}\right] \end{aligned}$$

- x-oriented dipole:

$$\begin{aligned}
\tilde{G}_{A_0}^{xx} &= \frac{\mu_0}{jk_{0z}}\left[e^{-jk_{0z}|z-z'|} + a_{xx}e^{-jk_{0z}z}\right] \\
\tilde{G}_{A_0}^{xz} &= \frac{\mu_0}{jk_{0z}}\left[\frac{k_{0z}k_x}{k_\rho^2}(a_{xz} - b_{xz})e^{-jk_{0z}z}\right] \\
\tilde{G}_{\phi_0}^{x} &= \tilde{G}_{\phi_0}^{h} = \frac{1}{\epsilon_0 jk_{0z}}\left[e^{-jk_{0z}|z-z'|} + \frac{k_0^2 a_h - k_{0z}^2 b_h}{k_\rho^2}e^{-jk_{0z}z}\right]
\end{aligned}$$

- y-oriented dipole:

$$\begin{aligned}
\tilde{G}_{A_0}^{yy} &= \frac{\mu_0}{jk_{0z}}\left[e^{-jk_{0z}|z-z'|} + a_{yy}e^{-jk_{0z}z}\right] \\
\tilde{G}_{A_0}^{yz} &= \frac{\mu_0}{jk_{0z}}\left[\frac{k_{0z}k_y}{k_\rho^2}(a_{yz} - b_{yz})e^{-jk_{0z}z}\right] \\
\tilde{G}_{\phi_0}^{y} &= \tilde{G}_{\phi_0}^{h},
\end{aligned}$$

where,

$$a_{xx} = a_{yy};\ \ a_{xz} = a_{yz};\ \ b_{xz} = b_{yz}. \tag{4.77}$$

For a half-space problem, the wave coefficients are:

$$\begin{aligned}
a_{zz} &= \tilde{R}_{TM}^{01}e^{-jk_{0z}z'} \\
a_v &= \tilde{R}_{TM}^{01}e^{-jk_{0z}z'} \\
a_{xx} &= \tilde{R}_{TE}^{01}e^{-jk_{0z}z'} \\
a_{xz} &= -\tilde{R}_{TM}^{01}e^{-jk_{0z}z'} \\
b_{xz} &= \tilde{R}_{TE}^{01}e^{-jk_{0z}z'} \\
a_h &= \tilde{R}_{TM}^{01}e^{-jk_{0z}z'} \\
b_h &= \tilde{R}_{TE}^{01}e^{-jk_{0z}z'},
\end{aligned}$$

where $\tilde{R}_{TM}^{01}$ and $\tilde{R}_{TE}^{01}$ are defined in (4.48) and (4.56), respectively. These spectral-domain Green's functions can be transformed into the spatial domain by using the various types of Sommerfeld integral transformations described in the section. Furthermore, multi-layered solutions for a_{zz}, a_v, a_{xx}, a_{xz}, b_{xz}, a_h and b_h can be easily determined using a similar derivation procedure as in the case of the half-space example.

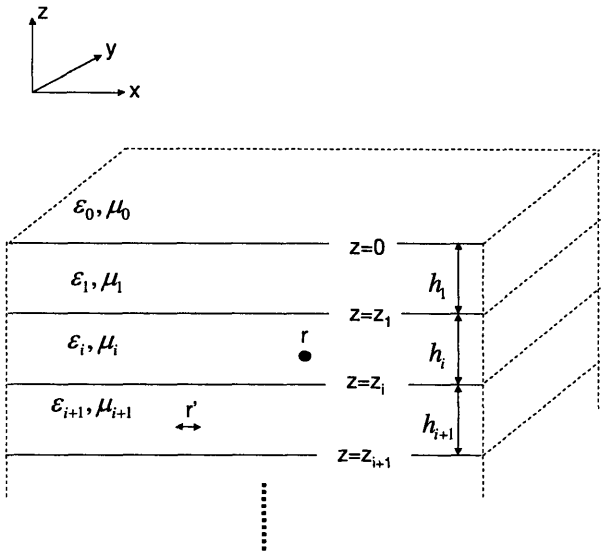

Figure 4-3: A source dipole and an evaluation point embedded in arbitrary layers of a multilayered planar medium.

In a more generalized situation as shown in Fig. 4-3, where the source is embedded in an arbitrary layer i, which is not necessarily the topmost region, and the field is evaluated in layer j, where j might not be equal to i, the following generalized procedure [6] can be used to derive the spectral-domain Green's functions.

1 Green's functions are derived in the source layer i where the z dependence of the field in the source region is formulated as a sum of 1) a spatially-unbounded Green's function, 2) a series of upward-traveling waves due to reflection at boundary $z = z_{i+1}$, and 3) a series of downward-traveling waves generated at $z = z_i$. The coefficients of the upward and downward traveling waves are obtained in terms of the generalized coefficients by applying the appropriate boundary conditions.

2 If the evaluation layer j is different from source layer i, Green's functions in the evaluation layer are obtained using an iterative algorithm [6] applied to each TE and TM component of the Green's functions in the source layer.

Details concerning the above procedure can be found in [6, 14].

An alternative procedure is offered by [45, 21] where a multi-layered planar structure is formulated in terms of a transmission-line like network along the axis normal to the stratification. Particularly, analogies can be drawn from the various Green's function components

to circuit components in an equivalent transmission line model so that familiar electromagnetic analysis of transmission line equations can be applied to determine solutions of these layered Green's functions.

Chapter 5

Background: Evaluation of Spatial-domain Layered Green's Functions

In the previous chapter, we have shown the derivation for the expression of spatial-domain dyadic vector potential and scalar potential layered Green's functions as Sommerfeld-type integrals over semi-infinite integration paths. In this section, we shall explore the numerous methods to evaluate these integrals, where these integrals are extremely complicated to compute and do not usually have closed forms. The reasons for the difficulty of evaluation can be attributed to the poles presented on the integration path for spectral function $\tilde{G}(k_\rho, z, z')$ and the oscillatory nature of the Bessel functions which prevents fast integration convergence. Hence this area of study has sparked much research effort that culminated into two major approaches, one of which consists of the numerical evaluation of the Sommerfeld integrals using special-purpose acceleration techniques such as those in [48, 21]. A lack of closed-form analytical expressions combined with a heavy cost associated with numerical algorithms for slow-converging integrals make this approach an inviable option for our interconnect analysis. The complex image method, on the other hand, has been extensively used in literature as well as in practice due to its versatility, efficiency, and ease of integration into existing potential/field solvers. It is due to this reason that the complex image method is chosen for the evaluation of Sommefeld integrals in our interconnect analysis problem.

5.1 Literature Survey on the Complex Image Method

The rudimentary concept behind the complex image method is to numerically approximate the kernel of a Sommerfeld-type integral as a series of exponentials with complex exponents and coefficients. The Sommerfeld Identity is then applied to these exponentials to produce a set of closed-form expressions in the spatial domain which serves as a complete replacement of the original Sommerfeld integral.

The image theory has been attempted by numerous authors with Van der Pol [74] being the first to interpret the closed-form analytical solutions of layered Green's functions as complex images. One of the early authors to participate in the modern development of the image theory is Silvester [64] who approximated the static equivalent of the dyadic Green's functions using a set of static images. Chow and El-behery [8] subsequently extended his work by modeling Green's functions in dynamic frequency ranges for a horizontal dipole in a half-space utilizing quasi-static images. Following Chow and El-behery, a series of papers was published by Lindell *et al.* who developed an image theory where a series of discrete and continuous images are utilized to approximate fields generated by vertical electric and magnetic dipoles in a half-space [39, 40] as well as in a horizontally-layered medium [41]. The most significant drawback associated with these early formulations is that the methods deteriorate rapidly when the relative dielectric constant or the thickness of the substrate increases, creating areas called "far fields" where surface waves dominate, and the image theory is no longer sufficiently accurate.

Fang *et al.* [17] recognized this problem and developed a method that became the cornerstone of all recent investigations. This method approximates solutions in the far field using a residue expression to account for the surface wave poles near the approximation contour of integration. According to his work, a Sommerfeld integral can be accurately approximated as a combination of:

1 Quasi-static images dominating in static near field; these images have real spatial locations and are obtained analytically using the Sommerfeld Identity.

2 Surface waves dominating in far field; the surface wave contributions are obtained using residue calculus.

3 Complex images with each image having a complex amplitude and occupying a com-

plex spatial location; these images are obtained by first approximating their spectral counterparts as series of exponentials using an exponential-fitting method called the Prony method [25]. These complex exponentials are then analytically transformed into the spatial domain using the Sommerfeld Identity.

When compared to the method developed by Lindell *et al.*, this three-part approximation approach has demonstrated a reduction in computational cost and an increase in accuracy. This concept of Green's function approximation is fully implemented by [80] in the case of a horizontal dipole above and embedded in a lossy medium as well as by [62] in the case of a vertical dipole above a lossy medium.

The idea of approximating a Sommerfeld integral-type Green's function by a three-part procedure was thus established, and the ensuing research focused on further defining and honing this methodology. For example, Chow *et al.* [9] extended the idea by providing a conceptual basis for the complex images, relating them to leaky waves that are important in the intermediate field region. Chow *et al.* were able to use many fewer terms for the closed-form Green's functions while still achieving an error of less than 1%. A critical inaccuracy in the method developed by Fang *et al.* was identified by Kipp and Chan [36] who supplied a correction to the methodology in the case where a source is embedded in a dielectric layer. This error was due to an incorrect description of the integration plane's branch-cut topology. The correction brought about by Kipp and Chan further extended the generality of the image approach. In addition, Hojjat *et al.* [27] vigorously demonstrated that the near field computation is inaccurate if the surface wave contributions were extracted from the spectral Green's functions. They also provided a range within which the surface waves must not be extracted. Furthermore, Hojjat *et al.* [28] extended the three-part approximation of a dyadic layered Green's function to include its non-symmetrical components, namely, G_A^{xz} and G_A^{yz}. The image method has become even more applicable and general to all possible cases encountered. Moreover, Dural and Aksun [14] offered several improvements to the three-part approximation technique that ultimately elevated the method to the status of being a practical tool for various circuit analysis applications. Their work include:

1 Provide a complete set of closed-form Green's functions in spectral and spatial domains for general stratified media.

2 Use a General Pencil of Function (GPOF) method [29] instead of a Prony method for

complex image calculation which is more robust and less noise sensitive.

3 Cast the closed-form Green's functions into a suitable form for the solution of the MPIE by the method of moments for a general 3D geometry.

In recent years, Aksun [1] offered another breakthrough that obviated the need to extract either quasi-static images or surface wave contributions; instead, he outlined a two-level approximation technique for the spectral-domain representation of the Green's functions which would generate, through the Sommerfeld Identity, a small set consisting of only complex images. The procedure developed previously suffered from the difficulty associated with choosing the appropriate approximation parameters for the exponential-fitting methods, thereby rendering the technique not so robust. Moreover, the extraction of the surface-wave poles and real images may not be possible for multi-layered geometries. Aksun's two-level approximation for the automatic generation of closed-form layered Green's functions overcomes these difficulties and makes the use of the method a convincing option in any robust and efficient EM solver.

In our research, we have logically chosen to approximate the various components of the layered Green's functions using the aforementioned two-level approximation technique. As an exception to the technique, since our analysis only involves a half-space configuration, the quasi-static images can be extracted without much difficulty and would reduce the number of images generated by the two-level approximation scheme, thus minimizing the overall computational cost. Therefore, in our approximation approach, each one of the spatial-domain Green's function components is represented as a sum of quasi-static and complex images that are obtained using the two-level method.

5.2 Extraction of Quasi-static Images

Quasi-static range of operation is only valid at extremely low operating frequencies (f), that is, as $f \rightarrow 0$. Using the same half-space problem as the previous chapter for illustration purposes, one can see that, under the quasi-static assumption, the wave-number k_0 in the source region R_0 also tends to 0, leading to the conclusion that $k_{0z} = k_{1z} = jk_\rho$, where $k_{iz} = \sqrt{k_i^2 - k_\rho^2}$ for $i = 0, 1$.

Since the Sommerfeld integral representation of the vector potential dyadic Green's

function as well as the scalar potential Green's function in region R_0 depend on the spectral values of $\tilde{R}_{TM}^{01}$ and $\tilde{R}_{TE}^{01}$, it is only logical to examine how the quasi-static assumptions would affect these values. Mainly,

$$\tilde{R}_{TM_q}^{0,1} = \tilde{R}_{TM}^{0,1}|_{k_{0z}=k_{1z}} = \frac{n^2-1}{n^2+1} \tag{5.1}$$

$$\tilde{R}_{TE_q}^{0,1} = \tilde{R}_{TE}^{0,1}|_{k_{0z}=k_{1z}} = 0, \tag{5.2}$$

signifying that $\tilde{R}_{TM}^{0,1}$ and $\tilde{R}_{TE}^{0,1}$ would converge to their spectral quasi-static values of $\tilde{R}_{TM_q}^{0,1}$ and $\tilde{R}_{TE_q}^{0,1}$ as f tends to zero.

Therefore substituting (5.1) into the Sommerfeld-type integral in (4.44) produces the following quasi-static expression $G_{A_{0z_q}}^{zz}$ for $G_{A_0}^{zz}$:

$$\begin{aligned} G_{A_{0z_q}}^{zz} &= \mu_0 \int_0^\infty \frac{1}{jk_{0z}} \tilde{R}_{TM_q}^{0,1} e^{-jk_{0z}(z+z')} J_0(k_\rho \rho) k_\rho dk_\rho \\ &= \mu_0 \frac{n^2-1}{n^2+1} \int_0^\infty \frac{1}{jk_{0z}} e^{-jk_{0z}(z+z')} J_0(k_\rho \rho) k_\rho dk_\rho \qquad (5.3) \\ &= \mu_0 \frac{n^2-1}{n^2+1} \frac{e^{-jk_0 r^0}}{r^0}, \qquad (5.4) \\ with \quad r^0 &= \sqrt{\rho^2 + (z+z')^2}. \qquad (5.5) \end{aligned}$$

The expression in (5.4) is obtained through the application of the Sommerfeld Identity which analytically back-transforms the expression in (5.3) to a closed-form spatial-domain quasi-static "image" in (5.7). This image of the source dipole is situated at a vertical distance z' below the plane of regional interface, where the interface serves as a "mirror" of reflection for the source dipole. Hence $G_{A_0}^{zz}$ can now be represented as:

$$\begin{aligned} G_{A_0}^{zz} &= G_{A_{0_s}}^{zz} + G_{A_{0z_q}}^{zz} + G_{A_{0z_r}}^{zz} \\ &= \mu_0 \left[\frac{e^{-jk_0 r}}{r} + \frac{n^2-1}{n^2+1} \frac{e^{-jk_0 r^0}}{r^0} + \int_0^\infty \frac{1}{jk_{0z}} (\tilde{R}_{TM}^{0,1} - \tilde{R}_{TM_q}^{0,1}) e^{-jk_{0z}(z+z')} J_0(k_\rho \rho) k_\rho dk_\rho \right], \end{aligned} \tag{5.6}$$

where the first term, $G_{A_{0_s}}^{zz}$, is the field contribution made by the source dipole in the absence of the stratified medium and $r = \sqrt{\rho^2 + (z-z')^2}$, the second term, $G_{A_{0z_q}}^{zz}$, is the the field associated with an image of the source dipole and $r^0 = \sqrt{\rho^2 + (z+z')^2}$, and the third term, $G_{A_{0z_r}}^{zz}$, is the remainder of the Sommerfeld integral after the extraction of the

quasi-static contribution, and this integral is to be expanded as a series of complex images as shall be explained shortly. Evidently if medium R_1 is infinitely conducting or if $f \rightarrow$ 0, then the third term would vanish, and the entire field solution can be represented as a combination of effected generated by the mirroring dipoles without the presence of the planar-stratified medium. This observation agrees with the equivalence principle in the classical electromagnetic theories [37].

As for the field created by a x-directed source dipole, no quasi-static images can be extracted for $G_{A_0}^{xx}$ since its spectral-domain representation, consisting of only $\tilde{R}_{TE}^{0,1}$, vanishes according to (5.2) as $f \rightarrow 0$. For field solution $G_{A_0}^{xz}$, after replacing $\tilde{R}_{TM}^{0,1}$ and $\tilde{R}_{TE}^{0,1}$ in (4.65) by their quasi-static values in (5.1) and (5.2), respectively, the following quasi-static expression is generated according to [27]:

$$\begin{aligned} G_{A_{0_q}}^{xz} &= -\mu_0 \cos\phi \int_0^\infty \left(\tilde{R}_{TM_q}^{0,1} + \tilde{R}_{TE_q}^{0,1} \right) e^{-jk_{0z}(z+z')} J_1(k_\rho \rho) dk_\rho \\ &= -\mu_0 \left(\frac{n^2-1}{n^2+1}\right) \cos\phi \int_0^\infty e^{-jk_{0z}(z+z')} J_1(k_\rho \rho) dk_\rho. \end{aligned} \tag{5.7}$$

Applying the following identity to (5.7):

$$\int_0^\infty e^{-a\mu} J_1(\mu\rho) d\mu = \frac{\sqrt{a^2+\rho^2} - a}{\rho\sqrt{a^2+\rho^2}},$$

and using the quasi-static assumption that $k_{0z} \rightarrow jk_\rho$, the quasi-static extraction of (5.7) becomes:

$$G_{A_{0_q}}^{xz} \approx -\mu_0 \left(\frac{n^2-1}{n^2+1}\right) \cos\phi \frac{\sqrt{(z+z')^2+\rho^2} - (z+z')}{\rho\sqrt{(z+z')^2+\rho^2}}. \tag{5.8}$$

It is obvious that the mathematical premise on which this quasi-static contribution is extracted doesn't fit into the general framework of the image theory in that there isn't a physical interpretation for the closed-form expression in (5.8). In addition, this expression cannot be easily integrated into the MPIE formulation in comparison to the $\frac{e^{-jkR}}{R}$ form taken by the other images. As mentioned earlier, the two-level approximation of Sommerfeld-type integrals doesn't actually require the extraction of quasi-static contributions in order to produce accurate solutions, therefore the quasi-static extraction in the case of $G_{A_0}^{xz}$ should be avoided.

Moving onto the quasi-static extractions of the scalar layered Green's functions, for the

case associated with a vertical dipole $G^v_{\phi_0}$, as defined in (4.72), the following quasi-static image is produced:

$$G^v_{\phi_{0_q}} = -\frac{1}{\epsilon_0}\frac{n^2-1}{n^2+1}\frac{e^{-jk_0r_0}}{r_0}, \tag{5.9}$$

where r_0 is defined in (5.5). Therefore $G^v_{\phi_0}$ can be represented by the following three-part approximation:

$$\begin{aligned} G^v_{\phi_0} &= G^v_{\phi_{0_s}} + G^v_{\phi_{0_q}} + G^v_{\phi_{0_r}} \\ &= \frac{1}{\epsilon_0}\left(\frac{e^{-jk_0r}}{r} - \frac{n^2-1}{n^2+1}\frac{e^{-jk_0r_0}}{r_0} - \int_0^\infty \frac{1}{jk_{0z}}(\tilde{R}^{0,1}_{TM} - \tilde{R}^{0,1}_{TM_q})e^{-jk_{0z}(z+z')}J_0(k_\rho\rho)k_\rho dk_\rho\right), \end{aligned}$$

with the first term, $G^v_{\phi_{0_s}}$, being the free-space Green's function for the source, the second term, $G^v_{\phi_{0_q}}$, being the quasi-static image of the source, and the last term, $G^v_{\phi_{0_r}}$, being the Sommerfeld integral remainder after the quasi-static contribution is extracted.

As for the scalar potential $G^h_{\phi_0}$ that is associated with a horizontal dipole in (4.76), the quasi-static expression becomes:

$$G^h_{\phi_{0_q}} = \frac{1}{\epsilon_0}\int_0^\infty \frac{1}{jk_{0z}}\frac{k_{0z}^2\tilde{R}^{01}_{TM_q}}{k_\rho^2}e^{-jk_{0z}(z+z')}J_0(k_\rho\rho)k_\rho dk_\rho.$$

Under the assumption that $k_{0z} \to jk_\rho$, the above expression is simplified to a closed-form image:

$$\begin{aligned} G^h_{\phi_{0_q}} &= -\frac{1}{\epsilon_0}\int_0^\infty \frac{1}{jk_{0z}}\tilde{R}^{01}_{TM_q}e^{-jk_{0z}(z+z')}J_0(k_\rho\rho)k_\rho dk_\rho. \\ &= -\frac{1}{\epsilon_0}\frac{n^2-1}{n^2+1}\frac{e^{-jk_0r_0}}{r_0}. \end{aligned} \tag{5.10}$$

Additionally, $G^v_{\phi_0}$ can also be represented by a three-component expression:

$$\begin{aligned} G^h_{\phi_0} &= G^h_{\phi_{0_s}} + G^h_{\phi_{0_q}} + G^h_{\phi_{0_r}} \\ &= \frac{1}{\epsilon_0}\left(\frac{e^{-jk_0r}}{r} - \frac{n^2-1}{n^2+1}\frac{e^{-jk_0r_0}}{r_0} + \int_0^\infty \frac{1}{jk_{0z}}(\tilde{R}^{0,1}_{TM} + \tilde{R}^{0,1}_{TM_q})e^{-jk_{0z}(z+z')}J_0(k_\rho\rho)k_\rho dk_\rho\right). \end{aligned}$$

The following table summaries the quasi-static images obtained for various type of Green's function components:

Green's function type	quasi-static image
$G_{A_0}^{xx}$	none
$G_{A_0}^{xz}$	none
$G_{A_0}^{zz}$	$\mu_0 \frac{n^2-1}{n^2+1} \frac{e^{-jk_0 r^0}}{r^0}$
$G_{\phi_0}^{v}$	$-\frac{1}{\epsilon_0} \frac{n^2-1}{n^2+1} \frac{e^{-jk_0 r^0}}{r^0}$
$G_{\phi_0}^{h}$	$-\frac{1}{\epsilon_0} \frac{n^2-1}{n^2+1} \frac{e^{-jk_0 r^0}}{r^0}$

Table 5.1: Quasi-static images corresponding to various type of layered Green's function components in region R_0 of a half-space medium;$r^0 = \sqrt{\rho^2 + (z+z')^2}$.

5.3 Expansion of Complex Images

The purpose of this section is to offer an accurate and efficient approach to approximating each Sommerfeld-type Green's function integral after the quasi-static contribution is extracted.

5.3.1 Preliminaries

Before entering the numerical process of integral evaluation, let's explore some mathematical grounds by first deriving the complex-plane topology induced by the variable of integration k_ρ and on which an integration path is defined.

$$k_\rho = \sqrt{k_i^2 - k_{z_i}^2}, \tag{5.11}$$

where i indexes the various layers in a multi-layered environment. It is obvious that k_ρ is a double-valued function, and therefore, the locations of various branch cuts and Riemann sheets should be explicitly located in order to identify the Sommerfeld integration path (SIP). This topic has been extensively addressed in literature, resulting in a SIP on the complex-k_ρ plane as shown in Fig. 5-1, which is determined by three effects [21, 36]:

1 *Hankel function branch cut.* The Hankel function has a logarithmic singularity at $k_\rho = 0$, and hence, produces a branch cut with an end point at the origin. This cut can be stipulated to extend along the negative real axis to connect with the other end point located at infinity. For the case of $Re(k_\rho) < 0$, the SIP should lie below the cut [47].

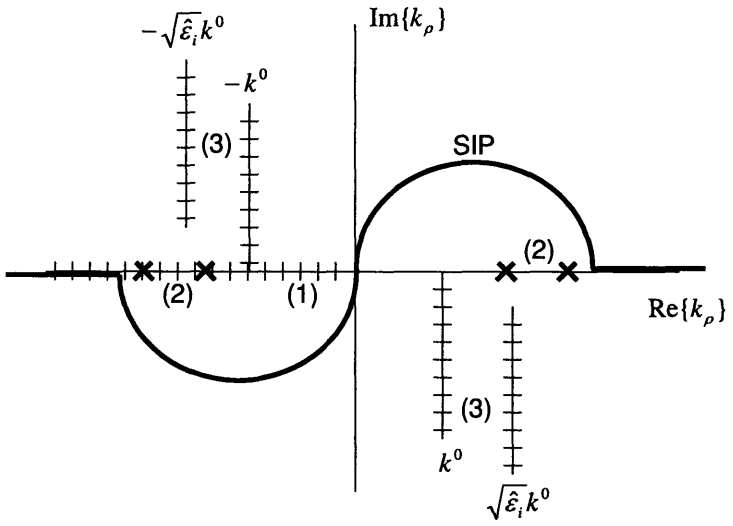

Figure 5-1: Topology of a spectral-domain Green's function in a complex-k_ρ plane with 1) being Hankel function branch cuts, 2) being surface-wave poles and 3) being k_{z_i} poles.

2 *surface wave poles.* The location and number of surface wave poles of the spectral Green's function depend both on the multi-layer structure and the excitation frequency. The spectral Green's functions are even functions of k_ρ so that the poles always appear in corresponding pairs in the complex-k_ρ topology. For lossless dielectrics, they are located on the real axis whereas in lossy materials, they migrate into the second and fourth quadrants of the complex-k_ρ plane. Consequently, restricting k_ρ to be real would lead to possibe strongly divergent behavior. This explains the fact that a lossless case is more difficult to integrate than a lossy case and that the SIP should be deformed in order to avoid possible singularities.

3 k_{zi} *branch cut.* The vertical wave-number associated with each layer, k_{z_i}, is a multi-valued function of k_ρ as demonstrated by:

$$k_{zi} = \sqrt{k_i^2 - k_\rho^2}, \tag{5.12}$$

with branch points at $k_\rho = \pm\sqrt{\hat{\epsilon}_i}k^0$, where $\hat{\epsilon}_i$ is the complex permittivity of the ith layer as defined in (4.1), and k^0 is the free-space wave-number. While the shape of

the branch cuts are arbitrary, they must extend toward $\pm j\infty$ rather than join each other along the real axis so that the SIP doesn't cross a branch cut [36]. However, only those wave-numbers associated with unbounded regions will have their branch cuts manifested in the spectral Green's functions. According to [6, 36], this can be explained by the fact that bounded layers have waves travelling in both directions, so the selection of the sign for the wave-number is irrelevant. In unbounded layers, waves are only travelling away from the source, and the sign of the wave number must be selected accordingly. For our half-space example, both the top and bottom layers are assumed to be unbounded, hence both k_{z_0} and k_{z_1} generate branch cuts for the spectral layered Green's functions.

In addition, the wave radiation condition needs to be imposed on the fields [37], that is, $Re\{k_{z_i}\} > 0$ and $Im\{k_{z_i}\} < 0$. Taking into account this condition as well as the various branch cuts and surface-wave poles, one comes to the conclusion that the SIP should be restricted to lie in the first and third quadrants while passing through the origin as shown in Fig. 5-1. There are equivalent choices of integration path and branch cuts, but the final results of integration should be the same.

5.3.2 Two-level Approximation Approach

The SIP in Fig. 5-1 is deformed to avoid the poles. However, according to [23], these poles do not lie on the entire real axis, but are concentrated, rather, in the interval $[k^0, k^0\sqrt{(\hat{\epsilon}_i)_{max}}]$, with $(\hat{\epsilon}_i)_{max}$ being the maximum relative permittivity of the layered medium. For this reason, the integration path can be divided into two distinct intervals: $[0, k^0\sqrt{(\hat{\epsilon}_i)_{max}}]$ on which a complex-k_ρ contour of integration is used to avoid the poles, and $[k^0\sqrt{(\hat{\epsilon}_i)_{max}}, \infty]$ on which k_ρ is real.

These two intervals form the basis of the two-level approximation approach developed by [1]. Traditionally, the one-level approximation [36, 9, 17] consists of the extraction of the quasi-static contribution as well as the surface-wave pole contribution before performing the integration of the remaining Green's function over a contour as shown in Fig. 5-2. However, as demonstrated by [1], this one-level approximation is not robust in that it requires the users to investigate apriori the spectral-domain behavior of the Green's function and to perform iterations to determine the most optimal approximation parameters needed by an

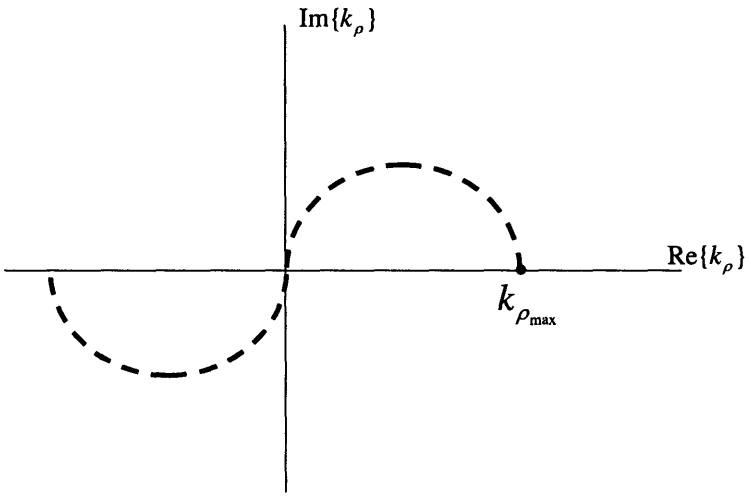

Figure 5-2: Complex-k_ρ integration path for a one-level approximation scheme.

exponential fitting method such as the GPOF. In addition, since the known exponential fitting methods only permit uniform sampling, a large number of samples much be taken in order to accurately approximate a slow-converging function with rapid changes, even if these changes only occur in a small region.

To circumvent these difficulties, the approximation is performed in two levels, with the first along the path of C_{ap1} and the second along C_{ap2} as shown in Fig. 5-3. The first-level approximation along the path of the real-k_ρ axis is performed with the double purpose of capturing the behavior of a spectral-domain Green's function in the far field for large k_ρ and delimiting the near field range within which the Green's function changes sharply for small k_ρ. The path C_{ap1} is defined as a mapping of a real variable t onto the imaginary k_z plane by:

$$\text{On } C_{ap1}: \quad k_{iz} = -jk_i(T_{02} + t), \quad 0 \leq t \leq T_{01} \tag{5.13}$$

where k_i is the wave-number for the source layer i. Hence k_ρ takes on real functional values in the interval of $[k_{\rho_{max_2}}, k_{\rho_{max_{21}}}]$ where:

$$k_\rho = k_i\sqrt{1 + (T_{02} + t)^2}, \quad 0 \leq t \leq T_{01}. \tag{5.14}$$

The reason that variable t parameterizes k_z rather than k_ρ, as one might expect, is that the spectral-domain Green's functions should be approximated in terms of exponentials of

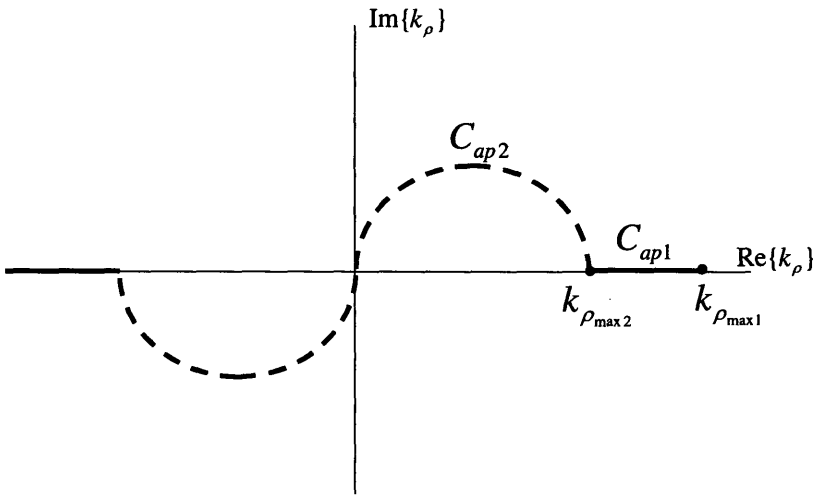

Figure 5-3: Complex-k_ρ integration path for a two-level approximation scheme.

k_z in order to take advantage of the Sommerfeld Identity.

The second level of the two-level approximation scheme is along the deformed path C_{ap2}, which is the same as the one-level scheme as shown in Fig. 5-2. This path is defined as a mapping of a real variable t onto the complex k_z plane by:

$$\text{On } C_{ap2}: \quad k_{iz} = k_i\big[-jt + (1 - \frac{t}{T_{02}})\big] \quad 0 \le t \le T_{02}. \tag{5.15}$$

In this case, k_ρ is a complex function where:

$$k_\rho = k_i\sqrt{1 - \Big[-jt + (1 - \frac{t}{T_{02}})\Big]^2}. \tag{5.16}$$

Details of the Two-level Approximation Scheme

Using the Sommerfeld-integral remainder in (5.6) as an example, we will illustrate step by step how the two-level approximation method is applied to obtain a set of analytical expressions for the integral. Just to reiterate, the integral has the form:

$$G^{zz}_{A0r} = \int_0^\infty \frac{1}{jk_{0z}}(\tilde{R}^{0,1}_{TM} - \tilde{R}^{0,1}_{TM_q})e^{-jk_{0z}(z+z')}J_0(k_\rho\rho)k_\rho dk_\rho. \tag{5.17}$$

According to the two-level approximation procedure:

1 Choose T_{02} in (5.13) and (5.15) such that $k_{\rho_{max_2}} > k^0\sqrt{(\hat{\epsilon}_i)_{max}}$, where $k_{\rho_{max_2}}$(=

$k_0\sqrt{1+T_{02}^2}$) is located on the real-axis of the complex-k_ρ plane as shown in Fig. 5-3, and $k^0\sqrt{(\hat{\epsilon}_i)_{max}}$ is the maximum value of the wave-number between the two layers. This choice serves as a delimiter between the complex contour of integration and the real contour of integration and is determined by the range where the surface-wave poles are concentrated.

2 Choose T_{01} in (5.13) and (5.15) such that $k_{\rho_{max_1}}\left(=k_0\sqrt{1+(T_{01}+T_{02})^2}\right)$ ensures that the behavior of the spectral-domain Green's function $\tilde{R}_{TM}^{0,1}-\tilde{R}_{TM_q}^{0,1}$ is captured for large values of k_ρ. The number of function samples on $[k_{\rho_{max_2}},\ k_{\rho_{max_1}}]$ is also chosen. Since the spectral-domain behavior is always smooth beyond $k_{\rho_{max_2}}$, it is not necessary to have a large number of samples in this interval.

3 Sample the spectral function $\tilde{R}_{TM}^{0,1}-\tilde{R}_{TM_q}^{0,1}$ along path C_{ap1} using the GPOF method; the sample is produced by varying t between 0 and T_{01} uniformly in (5.13). Therefore:

$$\begin{aligned}
\tilde{R}_{TM}^{0,1}-\tilde{R}_{TM_q}^{0,1}\approx f(k_\rho) &= \sum_{i=1}^{m} a_i e^{b_i t} \\
&= \sum_{i=1}^{m} a_i e^{b_i\left(\frac{k_{0z}}{-jk_0}-T_{02}\right)} \\
&= \sum_{i=1}^{m} \left(a_i e^{-T_{02}b_i}\right) e^{-\frac{b_i}{jk_0}k_{0z}} \\
&= \sum_{i=1}^{m} a_{t_i} e^{-b_{t_i}k_{0z}}, \qquad (5.18) \\
where\ \ a_{t_i}=a_i e^{-T_{02}b_i}; &\qquad b_{t_i}=\frac{b_i}{jk_0}.
\end{aligned}$$

Complex coefficients and exponents a and b, respectively, are obtained from the GPOF method, and m is the number of exponentials used in the approximation. This number is dependent on the number of significant singular values determined through a step of the GPOF method [29]. These coefficients and exponents are subsequently transformed to a_t and b_t in order to cast the approximating function into a form suitable for the application of the Sommerfeld Identity, namely, as an exponential function of k_{0z}. To mathematically illustrate this analytical transformation, let's first substitute the series of approximating exponentials in (5.18) into the original integral

(5.17), generating:

$$\begin{aligned}
&\int_0^\infty \frac{1}{jk_{0z}} f(k_\rho) e^{-jk_{0z}(z+z')} J_0(k_\rho\rho) k_\rho dk_\rho \\
&= \sum_{i=1}^{m} a_{t_i} \int_0^\infty \frac{1}{jk_{0z}} e^{-jk_{0z}\left(z+z'-\frac{b_{t_i}}{k_0}\right)} J_0(k_\rho\rho) k_\rho dk_\rho \\
&= \sum_{i=1}^{m} a_{t_i} \frac{e^{-jk_0 r_{cx_i}}}{r_{cx_i}} \qquad (5.19) \\
with\ r_{cx_i} &= \sqrt{r^2 + \left(z+z'-\frac{b_i}{k_0}\right)}. \qquad (5.20)
\end{aligned}$$

Each term in the summation of (5.19) is called a complex image of the source dipole, which is signified by its complex amplitude a_{t_i} and its complex location at a vertical distance $z + z' - \frac{b_i}{k_0}$ below the plane of media interface.

4 The approximating function $f(k_\rho)$ in (5.18) is subtracted from the original spectral-domain Green's function $\tilde{R}_{TM}^{0,1} - \tilde{R}_{TM_q}^{0,1}$ in order to guarantee that the function is negligible beyond $k_{\rho_{max_2}}$. In other words, the function will be nonzero only in a small range of $k_\rho \in [0, k_{\rho_{max_2}}]$ so that the fine features of the function in the near field can be captured without using many sampling points. To demonstrate this concept:

$$\begin{aligned}
G_{A0r}^{zz} &= \int_0^\infty \frac{1}{jk_{0z}} \left(\tilde{R}_{TM}^{0,1} - \tilde{R}_{TM_q}^{0,1} - f(k_\rho) + f(k_\rho)\right) e^{-jk_{0z}(z+z')} J_0(k_\rho\rho) k_\rho dk_\rho \\
&= \int_0^\infty \frac{1}{jk_{0z}} \left(\tilde{R}_{TM}^{0,1} - \tilde{R}_{TM_q}^{0,1} - f(k_\rho)\right) e^{-jk_{0z}(z+z')} J_0(k_\rho\rho) k_\rho dk_\rho \\
&\qquad + \int_0^\infty \frac{1}{jk_{0z}} f(k_\rho) e^{-jk_{0z}(z+z')} J_0(k_\rho\rho) k_\rho dk_\rho \\
&\approx \int_{C_{ap2}} \left(\tilde{R}_{TM}^{0,1} - \tilde{R}_{TM_q}^{0,1} - f(k_\rho)\right) e^{-jk_{0z}(z+z')} J_0(k_\rho\rho) k_\rho dk_\rho + \sum_{i=1}^{m} a_{t_i} \frac{e^{-jk_0 r_{cx_i}}}{r_{cx_i}} \qquad (5.21)
\end{aligned}$$

Note that the first integral is evaluated along only C_{ap2} due to the fact that the integrand is negligible along C_{ap1}.

5 The integral of (5.21) is sampled along C_{ap2}. Since the range [0, $k_{\rho_{max_2}}$] is small, the sampling frequency can still be quite high without incurring a large number of sample points. Applying the GPOF approximation method again to the spectral-

domain function of the integral in (5.21) generates:

$$\begin{aligned}
\tilde{R}_{TM}^{0,1} - \tilde{R}_{TM_q}^{0,1} - f(k_\rho) &\approx \sum_{i=1}^{n} a_{2i} e^{b_{2i} t} \\
&= \sum_{i=1}^{n} a_{2_i} e^{-b_{2_i} \frac{(\frac{k_{0z}}{k_0} - 1) T_{02}}{j T_{02} + 1}} \\
&= \sum_{i=1}^{n} \left(a_{2_i} e^{b_{2_i} \frac{T_{02}}{j T_{02}+1}} \right) e^{-b_{2_i} \frac{T_{02} k_{0z}}{k_0 (j T_{02}+1)}} \\
&= \sum_{i=1}^{n} a_{2_{t_i}} e^{-b_{2_{t_i}} k_{0z}}, \qquad (5.22) \\
where\ a_{2_{t_i}} = a_{2_i} e^{k_0 b_{2_{t_i}}}; &\qquad b_{2_{t_i}} = \frac{b_{2_i} T_{02}}{k_0 (j T_{02} + 1)}.
\end{aligned}$$

Substituting (5.22) into (5.21) and subsequently applying the Sommerfeld Identity yields:

$$G_{A0r}^{zz} \approx \sum_{i=1}^{n} a_{2t_i} \frac{e^{-jk_0 r_{cx2_i}}}{r_{cx2_i}} + \sum_{i=1}^{m} a_{t_i} \frac{e^{-jk_0 r_{cx_i}}}{r_{cx_i}}, \qquad (5.23)$$

$$with\ r_{cx2_i} = \sqrt{r^2 + \left(z + z' - \frac{b_{2_i} T_{02}}{k_0 (j T_{02} + 1)} \right)}. \qquad (5.24)$$

By following the above 5-step procedure, it can be seen that the semi-infinite integral of (5.17) can ultimately be approximated as a series of analytical complex images in (5.23).

It is evident that this procedure can also be applied in a straightforward manner to the treatment of Sommerfeld-type integrals of $G_{A_0}^{xx}$, $G_{\phi_0}^{v}$, $G_{\phi_0}^{h}$, in addition to $G_{A_0}^{zz}$. However, one problem remains concerning the use of the Sommerfeld Identity for the generation of closed-form approximations for $G_{A_0}^{xz}$, where its spectral-domain function has an additional linear dependence on jk_x. We have already shown in the previous section that the extraction of its quasi-static contribution is not a feasible task. Hence the Sommerfeld integral must be approximated in its entirety, with the integral being:

$$G_{A_0}^{xz}(\rho, z, z') = -\mu_0 \int_0^\infty \frac{1}{k_{0z}} \frac{k_{0z} k_x}{k_\rho^2} \left(- \tilde{R}_{TM}^{0,1} - \tilde{R}_{TE}^{0,1} \right) e^{-jk_{0z}(z+z')} J_0(k_\rho \rho) k_\rho dk_\rho.$$

Using the property defined in (4.35), $G_{A_0}^{xz}$ has an equivalent expression as:

$$G_{A_0}^{xz}(\rho, z, z') = -\mu_0 \frac{\partial}{\partial x} \left[\int_0^\infty \frac{1}{k_{0z}} \left[\frac{-jk_{0z}}{k_\rho^2} \left(- \tilde{R}_{TM}^{0,1} - \tilde{R}_{TE}^{0,1} \right) \right] e^{-jk_{0z}(z+z')} J_0(k_\rho \rho) k_\rho dk_\rho \right]. \qquad (5.25)$$

If we approximate the integral in the bracketed expression using the two-level method, then the following type of analytical forms are obtained:

$$\begin{aligned} G_{A_0}^{xz} &\approx -\mu_0 \frac{\partial}{\partial x}\left(\sum_{i=1}^{n} a_{2t_i}^{xz} \frac{e^{-jk_0 r_{cx2_i}^{xz}}}{r_{cx2_i}^{xz}} + \sum_{i=1}^{m} a_{t_i}^{xz} \frac{e^{-jk_0 r_{cx_i}^{xz}}}{r_{cx_i}^{xz}}\right) \\ &= -\mu_0 \left[\sum_{i=1}^{n} a_{2t_i}^{xz} \frac{\partial}{\partial x}\left(\frac{e^{-jk_0 r_{cx2_i}^{xz}}}{r_{cx2_i}^{xz}}\right) + \sum_{i=1}^{m} a_{t_i}^{xz} \frac{\partial}{\partial x}\left(\frac{e^{-jk_0 r_{cx_i}^{xz}}}{r_{cx_i}^{xz}}\right)\right], \end{aligned} \tag{5.26}$$

where the subscript xz is indicative of the fact that each set of complex coefficients and exponents is uniquely tailored the specific spectral-domain Green's function from which it is obtained. Hence this set of complex parameters is different from the set for the case of $G_{A_0}^{zz}$.

5.4 Chapter Summary

Combining the concept of real and complex images as explained in this section, we can now apply them to our half-space problem and expand each spatial-domain vector and scalar potential Green's function component into a sum of analytical forms as summarized in Table 5.2.

Green's function type	source dipole contribution	quasi-static image contribution	complex image contribution
$G_{A_0}^{xx}$	$\mu_0 \frac{e^{-jk_0 r}}{r}$	none	$\mu_0 \sum_i a_i^{xx} \frac{e^{-jk_0 r_{cx_i}^{xx}}}{r_{cx_i}^{xx}}$
$G_{A_0}^{xz}$	none	none	$\mu_0 \sum_i a_i^{xz} \frac{\partial}{\partial x}\left(\frac{e^{-jk_0 r_{cx_i}^{xz}}}{r_{cx_i}^{xz}}\right)$
$G_{A_0}^{yz}$	none	none	$\mu_0 \sum_i a_i^{xz} \frac{\partial}{\partial y}\left(\frac{e^{-jk_0 r_{cx_i}^{xz}}}{r_{cx_i}^{xz}}\right)$
$G_{A_0}^{zz}$	$\mu_0 \frac{e^{-jk_0 r}}{r}$	$\mu_0 \frac{n^2-1}{n^2+1} \frac{e^{-jk_0 r^0}}{r^0}$	$\mu_0 \sum_i a_i^{zz} \frac{e^{-jk_0 r_{cx_i}^{zz}}}{r_{cx_i}^{zz}}$
$G_{\phi_0}^{v}$	$\frac{1}{\epsilon_0} \frac{e^{-jk_0 r}}{r}$	$-\frac{1}{\epsilon_0} \frac{n^2-1}{n^2+1} \frac{e^{-jk_0 r^0}}{r^0}$	$-\frac{1}{\epsilon_0} \sum_i a_i^{zz} \frac{e^{-jk_0 r_{cx_i}^{zz}}}{r_{cx_i}^{zz}}$
$G_{\phi_0}^{h}$	$\frac{1}{\epsilon_0} \frac{e^{-jk_0 r}}{r}$	$-\frac{1}{\epsilon_0} \frac{n^2-1}{n^2+1} \frac{e^{-jk_0 r^0}}{r^0}$	$\frac{1}{\epsilon_0} \sum_i a_i^{h} \frac{e^{-jk_0 r_{cx_i}^{h}}}{r_{cx_i}^{h}}$

Table 5.2: Closed form approximations corresponding to various type of layered Green's function components in region R_0 of a half-space medium; $r = \sqrt{\rho^2 + (z-z')^2}$, $r^0 = \sqrt{\rho^2 + (z+z')^2}$ and $r_{cx} = \sqrt{\rho^2 + (z+z'-b_{cx})^2}$.

From Table 5.2, we see that the source contribution is the field generated by the source

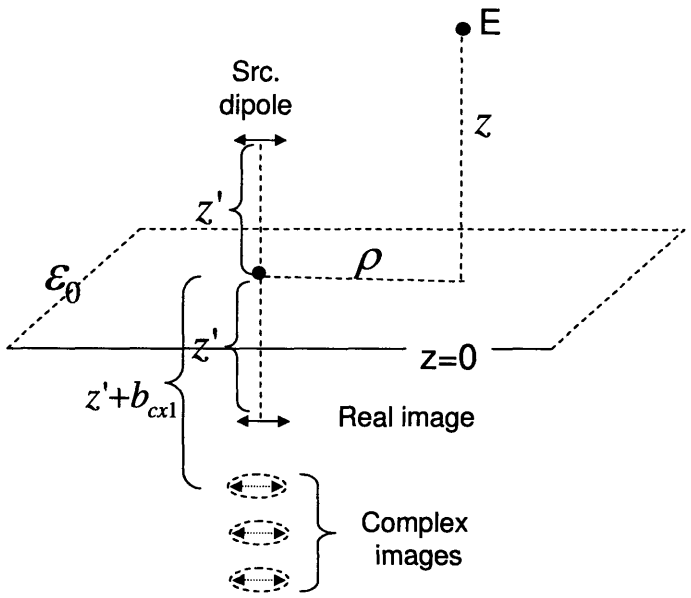

Figure 5-4: Complex image representation of G_{A0}^{xx}.

dipole at an evaluation point in the absence of the substrate; the distance between the source dipole and the evaluation point is denoted by $r = \sqrt{\rho^2 + (z - z')^2}$. The quasi-static image contribution is the field generated by the image of the source dipole and measured at an evaluation point in the absence of the substrate; the distance between the dipole image and the evaluation point is denoted by $r^0 = \sqrt{\rho^2 + (z + z')^2}$. Finally, the complex image contribution is the sum of the fields generated by a series complex images of the source dipole and measured at an evaluation point in the absence of the substrate; the distance between each complex source image and the evaluation point is denoted by $r_{cx} = \sqrt{\rho^2 + (z + z' - b_{cx})^2}$. Fig. 5-4 provides a graphical illustration of this concept. From the figure, the complex image theory becomes clear: the field generated by a dipole in the presence of a layered medium is the same as the field generated, in the absence of the medium, by the dipole itself and a set of its images with real and complex locations in space.

Several additional observations can be made. First, the complex coefficients and exponents of $G_{A_0}^{zz}$ and $G_{\phi_0}^{v}$ are the same due to the fact that both have the same spectral-domain Green's function remainder after the real images are extracted. Second, the GPOF method is only performed in four different cases of field computation due to symmetry and integrand

equivalence.

Chapter 6

Practical Considerations of Incorporating Layered Green's Functions into the MPIE

In Chapter 3, we have described the use of the MPIE formulation to numerically obtain potential-field solutions of complex 3D interconnect geometries. More specifically, one is able to determine magnetic vector potential A and electric scalar potential ϕ from the set of integral equations in the MPIE formulation by integrating type-specific Green's function kernels over conductor volumes and surfaces. For example, the set of layered Green's functions introduced in Chapter 5 can be utilized to account for the influence of a semiconductive substrate on a system of conductors. In this chapter, we shall explore the concept of incorporating these closed-form Green's functions into the MPIE formulation. Moreover, we will introduce a set of novel integration techniques of the closed-form layered Green's function kernels in order to promote the overall computational efficiency of the solver.

6.1 Integration of Layered Green's Functions into the MPIE

To assemble the discretized version of the MPIE as shown in the matrix form of (3.25), equations (3.26)-(3.30) must be numerically integrated with the incorporation of the layered

Green's function kernels G_A and G_ϕ. The vector potential computation in (3.27) becomes:

$$L_{ij}(r) = \int_v \int_v \overline{\overline{G}}_A(r,r')\overline{m}_i(r) \cdot \overline{m}_j(r')dr'dr,$$

where, after representing $\overline{m}_i(r)$ by its vector components $[m_{i_x}(r), m_{i_y}(r), m_{i_z}(r)]$ and substituting (4.15) for $\overline{\overline{G}}_A$,

$$\begin{aligned}
\overline{\overline{G}}_A(r,r')\overline{m}_i(r) \cdot \overline{m}_j(r') &= \begin{bmatrix} G_A^{xx}(r,r') & 0 & 0 \\ 0 & G_A^{yy}(r,r') & 0 \\ G_A^{xz}(r,r') & G_A^{yz}(r,r') & G_A^{zz}(r,r') \end{bmatrix} \begin{bmatrix} m_{i_x}(r) \\ m_{i_y}(r) \\ m_{i_z}(r) \end{bmatrix} \cdot \begin{bmatrix} m_{j_x}(r') \\ m_{j_y}(r') \\ m_{j_z}(r') \end{bmatrix} \\
&= G_A^{xx}(r,r')m_{i_x}(r)m_{j_x}(r') + G_A^{yy}(r,r')m_{i_y}(r)m_{j_y}(r') \\
&\quad + G_A^{xz}(r,r')m_{i_x}(r)m_{j_z}(r') + G_A^{yz}(r,r')m_{i_y}(r)m_{j_z}(r') \\
&\quad + G_A^{zz}(r,r')m_{i_z}(r)m_{j_z}(r'). \qquad (6.1)
\end{aligned}$$

Therefore,

$$\begin{aligned}
L_{ij}(r) &= \int_v \int_v G_A^{xx}(r,r')\Big(m_{i_x}(r)m_{j_x}(r') + m_{i_y}(r)m_{j_y}(r')\Big)drdr' \\
&\quad + \int_v \int_v G_A^{xz}(r,r')m_{i_x}(r)m_{j_z}(r')drdr' + \int_v \int_v G_A^{yz}(r,r')m_{i_y}(r)m_{j_z}(r')drdr' \\
&\quad + \int_v \int_v G_A^{zz}(r,r')m_{i_z}(r)m_{j_z}(r')drdr'. \qquad (6.2)
\end{aligned}$$

Equation (6.2) is obtained after having applied the simplification $G_A^{xx}(r,r') = G_A^{yy}(r,r')$ for a planar-stratified medium.

Similarly, (3.28) becomes,

$$P_{m\ell}(r) = \int_s \int_s G_\phi(r,r')v_\ell(r')v_m(r)dr'dr.$$

As explained in Sec. 4.2.3, a scalar layered Green's function is directionally associated to the orientation of the source dipole, with G_ϕ^v associated to a vertical dipole and G_ϕ^h to a horizontal dipole, hence the following simplification can be made:

$$G_\phi(r,r')v_\ell(r') = G_\phi^h(r,r')\Big(v_{\ell_x}(r') + v_{\ell_y}(r')\Big) + G_\phi^v(r,r')v_{\ell_z}(r'), \qquad (6.3)$$

where $[v_{\ell_x}(r'), v_{\ell_y}(r'), v_{\ell_z}(r')] = v_\ell(r')\hat{n}_s$, and $\hat{n}_s$ denotes the normal direction of the source conductor surface. Therefore,

$$P_{m\ell}(r) = \int_s \int_s G_\phi^h(r,r') v_m(r) \Big(v_{\ell_x}(r') + v_{\ell_y}(r') \Big) dr' dr + \int_s \int_s G_\phi^v(r,r') v_m(r) v_{\ell_z}(r') dr' dr. \tag{6.4}$$

Furthermore, since we have learned from the previous chapter that each layered Green's function component in (6.2) and (6.4) can be approximated by a set of closed-form images with forms shown in Table 5.2, the double volume and surface integrations of (6.2) and (6.4) can then be approximated by a series of integrations involving these closed-form images. For example, in (6.2), the double volume integration involving G_A^{zz} is approximated as:

$$\begin{aligned} &\int_v \int_v G_A^{zz}(r,r') m_{i_z}(r) m_{j_z}(r') dr dr' \\ &\approx \mu_0 \int_v \int_v \left(\frac{e^{-jk_0 R_s}}{R_s} + \frac{n^2-1}{n^2+1} \frac{e^{-jk_0 R^0}}{R^0} + \sum_i a_i^{zz} \frac{e^{-jk_0 R_{cx_i}^{zz}}}{R_{cx_i}^{zz}} \right) m_{i_z}(r) m_{j_z}(r') dr dr' \end{aligned} \tag{6.5}$$

where

$$\begin{aligned} R_s(r,r') &= \sqrt{(x-x')^2 + (y-y')^2 + (z-z')^2}; \\ R^0(r,r') &= \sqrt{(x-x')^2 + (y-y')^2 + (z+z')^2}; \\ R_{cx_i}^{zz}(r,r') &= \sqrt{(x-x')^2 + (y-y')^2 + (z+z'-b_{cx_i}^{zz})^2}. \end{aligned} \tag{6.6}$$

Moreover, if piecewise-constant basis functions as defined in (3.31) were used in a Galerkin scheme for the computation of the magnetic potential, then the above double volume integration over a pair of filaments i and j becomes:

$$\begin{aligned} &\frac{l_{j_z} l_{i_z}}{a_i a_j} \int_{v_i} \int_{v_j} G_A^{zz}(r,r') dr dr' \\ &\approx \mu_0 \frac{l_{j_z} l_{i_z}}{a_i a_j} \left(\int_{v_i} \int_{v_j} \frac{e^{-jk_0 R_s}}{R_s} dr' dr + \frac{n^2-1}{n^2+1} \int_{v_i} \int_{v_j} \frac{e^{-jk_0 R^0}}{R^0} dr dr' + \sum_i a_i^{zz} \int_{v_i} \int_{v_j} \frac{e^{-jk_0 R_{cx_i}^{zz}}}{R_{cx_i}^{zz}} dr dr' \right). \end{aligned} \tag{6.7}$$

As another example, consider the double surface integration of the G_ϕ^v kernel in (6.4). If

this kernel were to be replaced by its approximating images, then

$$\int_s\int_s G_\phi^v(r,r')v_m(r)v_{\ell_z}(r')dr'dr$$
$$\approx \frac{1}{\epsilon_0}\int_s\int_s\left(\frac{e^{-jk_0R_s}}{R_s}-\frac{n^2-1}{n^2+1}\frac{e^{-jk_0R^0}}{R^0}-\sum_i a_i^{zz}\frac{e^{-jk_0R^{zz}_{cx_i}}}{R^{zz}_{cx_i}}\right)v_m(r)v_{\ell_z}(r')dr'dr, \tag{6.8}$$

where R_s, R^0 and $R^{zz}_{cx_i}$ are defined in (6.6). If piecewise-constant collocation technique were applied to the scalar potential calculation, then the above surface integration over a pair of panels ℓ and m, with panel ℓ being the evaluation panel, becomes:

$$\int_{s_m} G_\phi^v(r_{\ell_c},r')dr'$$
$$\approx \frac{1}{\epsilon_0}\left(\int_{s_m}\frac{e^{-jk_0R_s(\ell_c,r')}}{R_s(\ell_c,r')}dr'-\frac{n^2-1}{n^2+1}\int_{s_m}\frac{e^{-jk_0R^0(\ell_c,r')}}{R^0(\ell_c,r')}dr'-\sum_i a_i^{zz}\int_{s_m}\frac{e^{-jk_0R^{zz}_{cx_i}(\ell_c,r')}}{R^{zz}_{cx_i}(\ell_c,r')}dr'\right), \tag{6.9}$$

where ℓ_c is the centroid of panel ℓ.

As an observation, if a piecewise-constant Galerkin scheme were utilized in the computation of vector potentials, then the resulting double volume integrations consist of the following two types of scalar kernels:

$$\text{Type I:} \quad \frac{e^{-jkR}}{R}$$

$$\text{Type II:} \quad \frac{\partial}{\partial h}\left(\frac{e^{-jkR}}{R}\right); \quad \text{h=x or y,}$$

while distance R has the various forms as defined in (6.6). Similarly, if a piecewise-constant centroid-collocation scheme were used in the scalar potential analysis, then the resulting panel integrations consist of only the Type I kernel as suggested by Table 5.2.

6.2 Volume Integration of Type I kernel

As a consequence of using the Galerkin technique for vector potential computations, the resulting double volume integrals, in (6.7) for example, are extremely expensive to compute if a traditional 3D quadrature approach were to be applied to both inner and outer integrations. This observation motivates the development of a set of accelerated integration

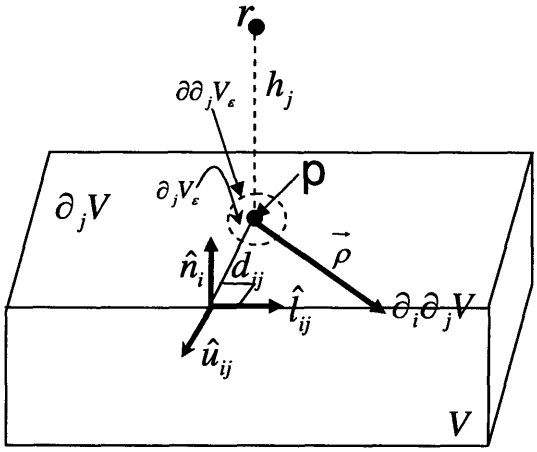

Figure 6-1: Geometric definition of quantities used in a volume integration scheme.

schemes applicable to inner volume integrations, which when combined with a 3D quadrature approach to outer integrations, dramatically enhances the efficiency of the overall double volume integration process.

First, let's examine the case of

$$\int_V \frac{e^{-jk|r'-r|}}{|r'-r|} dv'. \tag{6.10}$$

Consider the distribution of sources within a filament of volume V. As shown in Fig. 6-1, the surface of V, denoted by ∂V, is composed of several faces, each indexed as $\partial_j V$. Each $\partial_j V$ has an outward unit normal $\hat{n}_j$. The perpendicular distance generated from the projection of the observation point r onto the plane of $\partial_j V$ is denoted as h_j. This style of notation is adopted from [78].

The first step in evaluating the volume integral in (6.10) is to apply the Divergence theorem [37] to transform the integral in V to an integration over ∂V. The theorem states,

$$\int_V (\nabla \cdot \overline{F}) dv = \int_{\partial V} \overline{F} \cdot \hat{n} \; da. \tag{6.11}$$

6.2.1 Observation I: Volume-to-surface Integration

According to (6.11), the volume integration in (6.10) can be transformed to an integral over the volume's enclosing surfaces if a vector can be determined such that its divergence is the same as the integrand in (6.10). In order to apply such theorem, the integration kernel must be continuously differentiable over the domain of integration V. This is not the case, however, when the observation point r is in V or on ∂V. A separate treatment is devised to handle this self-term case as shown in the latter part of this section. However, if r is outside of V, the Divergence theorem is applied to (6.10) which yields

$$\begin{aligned}
\int_V \frac{e^{-jkR}}{R} dv' &= \int_V \nabla' \cdot \overline{R}\left[\frac{1}{-jk}\frac{e^{-jkR}}{R^2} - \frac{1}{(-jk)^2}\left(\frac{e^{-jkR}}{R^3} - \frac{1}{R^3}\right)\right] dv' \\
&= \int_{\partial V} \hat{n} \cdot \overline{R}\left[\frac{1}{-jk}\frac{e^{-jkR}}{R^2} - \frac{1}{(-jk)^2}\left(\frac{e^{-jkR}}{R^3} - \frac{1}{R^3}\right)\right] ds' \\
&= \sum_j \int_{\partial_j V} \hat{n}_j \cdot \overline{R}\left[\frac{1}{-jk}\frac{e^{-jkR}}{R^2} - \frac{1}{(-jk)^2}\left(\frac{e^{-jkR}}{R^3} - \frac{1}{R^3}\right)\right] ds' \\
&= \sum_j h_j \int_{\partial_j V} \left[\frac{1}{-jk}\frac{e^{-jkR}}{R^2} - \frac{1}{(-jk)^2}\left(\frac{e^{-jkR}}{R^3} - \frac{1}{R^3}\right)\right] ds',
\end{aligned} \tag{6.12}$$

where $\overline{R} = \hat{x}(x - x') + \hat{y}(y - y') + \hat{z}(z - z')$ is a vector from r to r', and $R = ||\vec{R}||$.

In (6.12), the 3D integration in V is transformed to a sum of 2D integrations over faces bounding V. In order to proceed further, more properties have to be defined for $\partial_j V$ in relation to the observation point r as shown in Fig. 6-1:

- P is the end point of the projection of r onto the plane defined by $\partial_j V$.
- $\partial_j V$ is enclosed by a set of edges, each indexed as $\partial_i \partial_j V$.
- For each $\partial_i \partial_j V$, a local coordinate system is defined with the origin centered at P and three axes of directions, $\hat{l}_{ij}$,$\hat{u}_{ij}$ and $\hat{n}_j$.
- d_{ij} is the perpendicular distance of the projection of P onto the line $\partial_i \partial_j V$.
- $\overline{\rho}$ is a vector from P to a point on $\partial \partial_j V$, the boundary of $\partial_j V$, and ρ denotes the distance between the two points.

6.2.2 Observation II: Surface-to-line Integration

The Divergence theorem can be applied once more to transform integration over surface $\partial_j V$ to one over contour $\partial\partial_j V$ of $\partial_j V$. However, if P is in $\partial_j V$ or on $\partial\partial_j V$, before such theorem can be applied, it is necessary to exclude for separate treatment a region of $\partial_j V_\epsilon$, which is the intersection of $\partial_j V$ and a small disk of radius ϵ centered at P. Continue on with the calculation of (6.12), but for the sake of brevity, let's define *I(R)* to be the integrand of (6.12) such that

$$\begin{aligned}
\int_V \frac{e^{-jkR}}{R} dv' &= \sum_j h_j \int_{\partial_j V} I(R) ds' \\
&= \lim_{\epsilon \to 0} \sum_j h_j \int_{\partial_j (V - V_\epsilon)} I(R) ds' + \lim_{\epsilon \to 0} \sum_j h_j \int_{V_\epsilon} I(R) ds' \\
&= \lim_{\epsilon \to 0} \sum_j h_j \int_{\partial_j (V - V_\epsilon)} \nabla' \cdot \frac{\overline{\rho}}{\rho^2} \left[\frac{1}{(-jk)^2} \left(\frac{e^{-jkR}}{R} - \frac{1}{R} \right) - \frac{1}{-jk} \right] ds' \\
&= \lim_{\epsilon \to 0} \sum_j h_j \int_{\partial\partial_j (V - V_\epsilon)} \hat{u} \cdot \frac{\overline{\rho}}{\rho^2} \left[\frac{1}{(-jk)^2} \left(\frac{e^{-jkR}}{R} - \frac{1}{R} \right) - \frac{1}{-jk} \right] dl' \\
&= \sum_j h_j \sum_i \int_{\partial_i \partial_j V} \frac{d_{ij}}{\rho^2} \left[\frac{1}{(-jk)^2} \left(\frac{e^{-jkR}}{R} - \frac{1}{R} \right) - \frac{1}{-jk} \right] dl' \\
&\quad + \lim_{\epsilon \to 0} \sum_j h_j \int_{\partial\partial_j V_\epsilon} \hat{u} \cdot \frac{\overline{\rho}}{\rho^2} \left[\frac{1}{(-jk)^2} \left(\frac{e^{-jkR}}{R} - \frac{1}{R} \right) - \frac{1}{-jk} \right] dl',
\end{aligned} \tag{6.13}$$

where $\hat{u}$ is the outward normal vector of $\partial_j V \backslash \partial_j V_\epsilon$. The last integral of (6.13) can be evaluated using a local polar coordinate system centered at P. This produces:

$$\begin{aligned}
&\lim_{\epsilon \to 0} \sum_j h_j \int_{\partial\partial_j V_\epsilon} \hat{u} \cdot \frac{\overline{\rho}}{\rho^2} \left[\frac{1}{(-jk)^2} \left(\frac{e^{-jkR}}{R} - \frac{1}{R} \right) - \frac{1}{-jk} \right] dl' \\
&= \sum_j h_j \sum_i \int_{\partial_i \partial_j V} \frac{d_{ij}}{\rho^2} \left[\frac{1}{(-jk)^2} \left(\frac{e^{-jk|h|}}{|h|} - \frac{1}{|h|} \right) - \frac{1}{-jk} \right] dl'.
\end{aligned} \tag{6.14}$$

Substituting (6.14) into (6.13) yields the final expression

$$\int_V \frac{e^{-jkR}}{R} dv' = \sum_j h_j \sum_i \int_{\partial_i \partial_j V} \frac{d_{ij}}{\rho^2} \left[\frac{1}{(-jk)^2} \left(\frac{e^{-jkR} - 1}{R} - \frac{e^{-jk|h|} - 1}{|h|} \right) \right] dl'. \tag{6.15}$$

Equation (6.15) shows that the volume integration of (6.10) can be transformed to a sum of 1D integrations over the line segments contouring the volume.

6.2.3 Self-term Volume Integration

For the separate case where $r \in V \backslash \partial V$, a simple approximation scheme is used. That is,

$$\int_V \frac{e^{-jk|r-r'|}}{|r-r'|} dv' = \sum_i e^{-jk|r-r_{ic}|} \int_{V_i} \frac{1}{|r-r'|} dr', \tag{6.16}$$

where the source filament is divided into sub-filaments, and r_{ic} is the center of the ith sub-filament. The integral in (6.16) is solved using the method described in [78] which transforms the volume integral of $\frac{1}{|r-r'|}$ into a sum of boundary segment integrals through the application of the Divergence theorem. The effect of extracting the e^{-jkR} term outside of the integral is minimal since both source and evaluation points vary within only one filament-length, which is a small fraction of the wavelength.

6.3 Volume Integration of Type II kernel

Let's examine the case of

$$\int_V \frac{\partial}{\partial h} \frac{e^{-jk|r'-r|}}{|r'-r|} dv', \quad where \;\; h = x \; or \; y. \tag{6.17}$$

Since only G^A_{xz} and G^A_{yz} require the use of Type II kernels, there is no need to be concerned with the self-term case where $r \in V \backslash \partial V$. Through two consecutive applications of the Divergence theorem, the volume integral of (6.17) can also be transformed to a sum of 1D line

integrals. That is,

$$\begin{aligned}
\int_V \frac{\partial}{\partial h}\frac{e^{-jk|r'-r|}}{|r'-r|}dv' &= -\int_V \nabla'\cdot\left(\hat{h}\frac{e^{-jkR}}{R}\right)dv' \\
&= -\int_{\partial V}\hat{n}\cdot\hat{h}(\frac{e^{-jkR}}{R})ds' \\
&= -\sum_j n_{j_h}\int_{\partial_j V}\frac{e^{-jkR}}{R}ds' \\
&= -\sum_j n_{j_h}\int_{\partial_j V}\nabla'\cdot\frac{\overline{\rho}}{\rho^2}\left(\frac{e^{-jkR}}{-jk}-\frac{1}{-jk}\right)ds' \\
&= -\sum_j n_{j_h}\int_{\partial\partial_j V}\hat{u}\cdot\frac{\overline{\rho}}{\rho^2}\left(\frac{e^{-jkR}}{-jk}-\frac{1}{-jk}\right)dl' \\
&= -\sum_j n_{j_h}\sum_i \frac{d_{ij}}{\rho^2}\int_{\partial_i\partial_j V}\left(\frac{e^{-jkR}}{-jk}-\frac{1}{-jk}\right)dl',
\end{aligned} \tag{6.18}$$

where n_{j_h} is either the x or y component of $\hat{n}_j$.

6.4 Surface Integration of Type I kernel

To determine the surface integration of the Type I kernel,

$$\int_S \frac{e^{-jk|r-r'|}}{|r-r'|}ds', \tag{6.19}$$

one immediately sees that the solution is already obtained in (6.18) where the integrand generated after applying the first Divergence theorem is exactly the same as the integrand of the surface integration. However, one still needs to account for the case where evaluation point $r \in S \setminus \partial S$. In another words, if the end point of the projection of r is in S or on $\partial_j S$, before the Divergence theorem can be applied, it is necessary to exclude for separate treatment a region of S_ϵ, which is the intersection of S and a small circle of radius ϵ centered at P. Such configuration is shown in Fig. 6-2. Using the notation defined in Fig. 6-2,

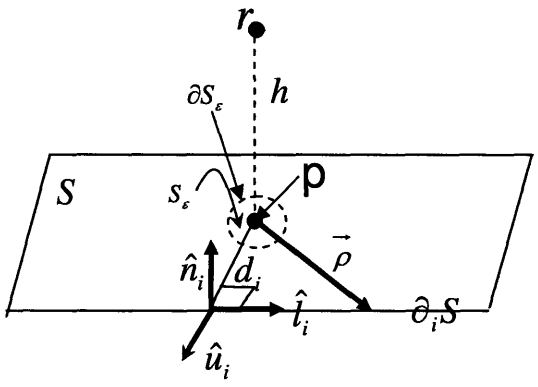

Figure 6-2: Geometric definition of quantities used in a surface integration scheme.

$$\begin{aligned}
\int_S \frac{e^{-jk|r-r'|}}{|r-r'|}ds' &= \lim_{\epsilon\to 0}\int_{(S-S_\epsilon)} \frac{e^{-jk|r-r'|}}{|r-r'|}ds' + \int_{S_\epsilon} \frac{e^{-jk|r-r'|}}{|r-r'|}ds' \\
&= \lim_{\epsilon\to 0}\int_{(S-S_\epsilon)} \nabla'\cdot\frac{\overline{\rho}}{\rho^2}\left(\frac{e^{-jkR}}{-jk}-\frac{1}{-jk}\right)ds' \\
&= \lim_{\epsilon\to 0}\int_{(S-S_\epsilon)} \hat{u}\cdot\frac{\overline{\rho}}{\rho^2}\left(\frac{e^{-jkR}}{-jk}-\frac{1}{-jk}\right)ds' \\
&= \sum_i \frac{d_i}{\rho^2}\int_{\partial_i S}\left(\frac{e^{-jkR}}{-jk}-\frac{1}{-jk}\right)dl' + \lim_{\epsilon\to 0}\int_{S_\epsilon}\hat{u}\cdot\frac{\overline{\rho}}{\rho^2}\left(\frac{e^{-jkR}}{-jk}-\frac{1}{-jk}\right)ds',
\end{aligned} \tag{6.20}$$

where $\hat{u}$ is the outward normal vector of $S\backslash S_\epsilon$. The last surface integral of (6.20), when casted into the polar coordinate system, can also be reduced to a sum of 1D line integrals over the segments bounding the surface:

$$\lim_{\epsilon\to 0}\int_{S_\epsilon}\hat{u}\cdot\frac{\overline{\rho}}{\rho^2}\left(\frac{e^{-jkR}}{-jk}-\frac{1}{-jk}\right)ds' = \sum_i \frac{d_i}{\rho^2}\int_{\partial_i S}\left(\frac{e^{-jk|h|}}{-jk}-\frac{1}{-jk}\right)dl', \tag{6.21}$$

where h is the normal projection of r onto S. When substituting (6.21) into (6.20), one obtains the final expression:

$$\int_S \frac{e^{-jk|r-r'|}}{|r-r'|}ds' = \sum_i \frac{d_i}{\rho^2}\int_{\partial_i S}\left(\frac{e^{-jkR}}{-jk}-\frac{e^{-jk|h|}}{-jk}\right)dl'. \tag{6.22}$$

6.5 Chapter Summary

Table 6.1 summaries all the 1D integral representations obtained for the volume or surface integrations of the full-wave Green's function kernels used in potential evaluations. It should be emphasized that these integrals are only valid if piecewise-constant basis functions were utilized.

Integration region	Integration type	1D integral representation
$r \notin V \backslash \partial V$	$\int_V \frac{e^{-jkR}}{R} dv'$	$\sum_j h_j \sum_i \int_{\partial_i \partial_j V} \frac{d_{ij}}{\rho^2} \left[\frac{1}{(-jk)^2} \left(\frac{e^{-jkR}-1}{R} - \frac{e^{-jk\lvert h\rvert}-1}{\lvert h\rvert} \right) \right] dl'$
$r \in V \backslash \partial V$	$\int_V \frac{e^{-jkR}}{R} dv'$	$\sum_i e^{-jk\lvert r-r_{ic}\rvert} \int_{V_i} \frac{1}{\lvert r-r'\rvert} dr'$
$r \notin V \backslash \partial V$; h=x or y	$\int_V \frac{\partial}{\partial h} \frac{e^{-jk\lvert r'-r\rvert}}{\lvert r'-r\rvert} dv'$	$-\sum_j n_{j_h} \sum_i \frac{d_{ij}}{\rho^2} \int_{\partial_i \partial_j V} \left(\frac{e^{-jkR}}{-jk} - \frac{1}{-jk} \right) dl'$
all cases	$\int_S \frac{e^{-jk\lvert r-r'\rvert}}{\lvert r-r'\rvert} ds'$	$\sum_i \frac{d_i}{\rho^2} \int_{\partial_i S} \left(\frac{e^{-jkR}}{-jk} - \frac{e^{-jk\lvert h\rvert}}{-jk} \right) dl'$

Table 6.1: Representation of volume and surface integrations of full-wave Green's function kernels as series of 1D line integrations.

Chapter 7

Optimization-based Frequency-parameterizing Basis Functions

The conductors-over-substrate impedance solver described in the previous sections uses piecewise-constant basis functions to approximate the unknown conductor filament currents for any layout geometry. However, the efficiency of the solver is being challenged by the ever increasing operating frequencies which generate skin and proximity effects, as illustrated in Fig. 7-1, that need to be accurately modeled in order to provide accurate impedance solutions.

If piecewise constant basis functions were used to model these effects, each conductor volume is first discretized lengthwise into individually conducting segments with the assumption that the cross-sectional current density does not vary along the length of the segments. The number of segments produced per conductor is dictated by accuracy, and the segments are always much shorter than a wavelength. Then the cross-sectional interior of each segment is discretized in a manner dictated by skin depth [11], hence generating, per segment, bundles of many tightly-packed parallel filaments with very large aspect ratios. One might think this is not problematic if the system were to be solved by a fast technique since, theoretically speaking, the computational cost only scales in a linear fashion with the total number of basis functions. The resulting filament-to-filament interactions within each segment, however, cannot be accelerated by fast techniques that are based on the

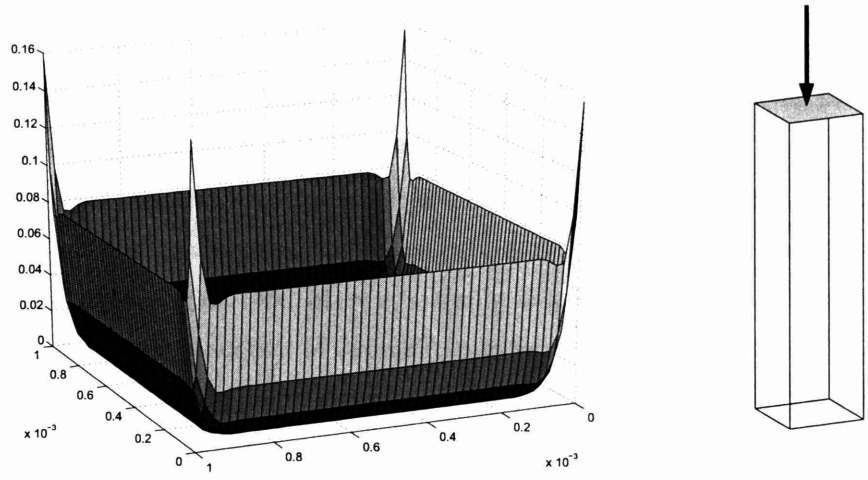

Figure 7-1: Skin effect: high frequency current-crowding phenomenon over the cross-section of a filament.

approximation of distant interactions only. Therefore direct computations must be used to resolve these near-distanced interactions with a complexity that grows quadratically with the number of filaments per segment.

The explosive cost associated with high-frequency impedance simulations has spurred the development of methods that seek to either represent interior conductor current using surface field quantities [10, 30, 65, 73, 77] or generate specialized basis functions that have the built-in capability of capturing interior current variations [12, 11]. However, major drawbacks have been observed in the first approach where surface-based formulations such as [77, 30] result in excessively complex systems that are numerical unstable at low-frequencies. Therefore, for the sake of accuracy and robustness of implementation, the latter of the two approaches is preferred.

Specifically, according to [12], a set of specialized basis functions is derived from the interior Helmoholtz equations governing the flow of longitudinal current through a conductor. The resulting basis function set is composed of a series of exponentials, with each exponential being a function of frequency and cross-sectional position and is referred to as a "conduction mode." Each conduction mode is capable of capturing the frequency-dependent current distribution originating from a certain region of a conductor's cross section. However, these specialized basis functions can only be generated for those cross-section shapes where analytical solutions of the diffusion equation are available. Practically speaking, only rectangular and cylindrical cross-sections can be handled. Another disadvantage of the

conduction mode basis functions is that they are incapable of capturing proximity effects in neighboring wires of dissimilar cross-sectional shapes.

To remedy these shortcomings, [11] describes another set of basis functions called "proximity templates" that is pre-computed numerically at each desired frequency for each unique conductor cross-section type. More specifically, at a desired frequency, basis function templates for a source conductor of a specific cross-section type are constructed as a composite of nine or so simulation results generated from placing test conductors at judiciously chosen locations surrounding the source conductor. An apparent disadvantage of such an approach is the high computational cost associated with constructing these basis functions if there exists a large number of frequency points of interest. Another disadvantage is the lack of predictability in the method's accuracy due to the fact that its solutions are entirely dependent on how well the locations of the few trial samples are chosen.

In this chapter, a set of novel basis functions is introduced that maximizes the efficiency with which large and complex interconnect structures are modeled. According to the procedure outlined in Sec. 7.1 of this chapter, these basis functions only need to be pre-computed once per conductor cross-section geometry of interest, and they are valid for a wide range of frequencies of operation. For the sake of reusability, these basis functions can be stored off-line with a minimal storage cost. In spite of having the advantage of being inherently frequency-independent within a given frequency range, these basis functions are also able to collectively capture the frequency-variant nature of conductor current distributions, hence providing reasonably accurate modeling solutions with far fewer degrees of freedom in comparison to the use of traditional basis functions. Furthermore, post-optimization techniques are applied to the resulting basis functions in order to guarantee their robustness. The necessity of such optimization is firmly established in Sec. 3.5.2 of this thesis. In addition, these basis functions will not complicate the cost of volume integrations in a Galerkin scheme if a MPIE formulation were used.

7.1 Pre-computation of Specialized Basis Functions

This section describes the construction of a high-order basis that minimizes the number of functions per segment, parameterizes the frequency-dependent nature of current variation unique to different cross-section shapes, and guarantees frequency-independence for a wide

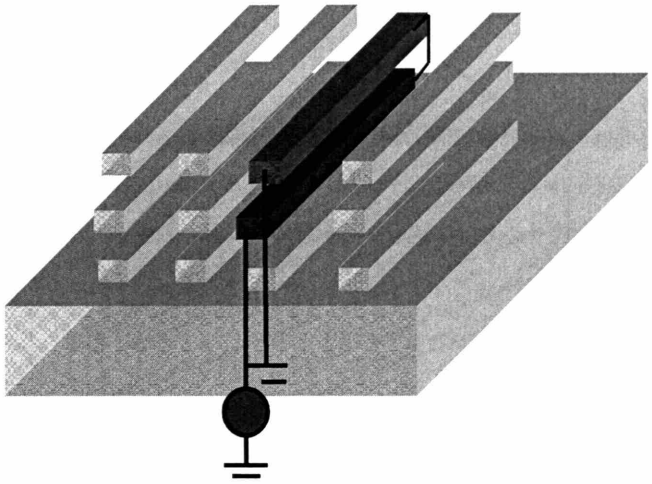

Figure 7-2: Example of a source and test conductor pair for the construction of specialized basis functions that capture skin and proximity effects.

range of frequencies. The procedure is as follows:

1 For a given conductor of a specific cross-section shape, let's call this conductor a "source" conductor, consider placing another conductor, called "test" conductor, at a certain interaction distance r_i from the source conductor. Shorting the conductors at one end while exciting the structure with a unity current source at a desired frequency point would allow one to examine the current distribution over the cross section of the source conductor in response to the proximity effect generated by the test conductor at position r_i. Fig. 7-2 shows an example of such source and test conductor pair. The resulting solution of source current response v_i is obtained by using a very fine piecewise constant discretization method, hence producing η filaments per conductor segment. Extending this concept to p such test conductors situated at various locations surrounding the source conductor, one would thus obtain, for a specific excitation frequency, a collection V of such current solutions for the source conductor with $V = \{\overline{v}_i\}, i = 1 \ldots p$, and each vector $\overline{v}_i$ is of length η. If the spatial sampling of the test conductors is sufficiently fine, matrix V would contain a decent set of "snapshots" from which proximity effects for a specific cross-section shape at a specific frequency can be captured. This step of the procedure is the same as the basis function generation procedure in [11].

2 Now select a set of frequency samples $S^n = \{s^1, s^2, ..., s^n\}$ at which step *1* is repeated.

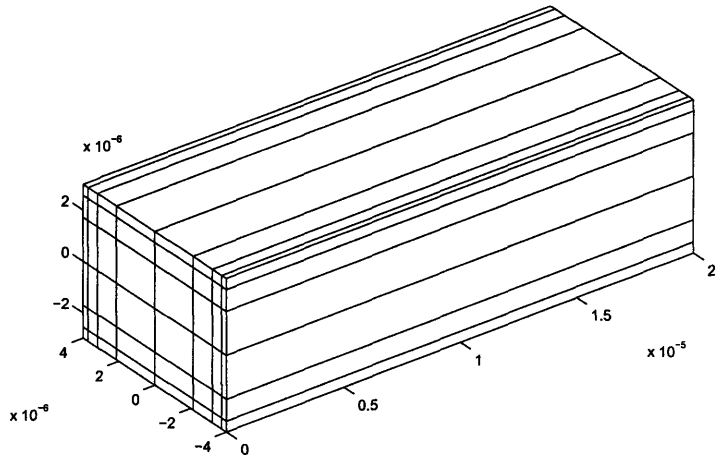

Figure 7-3: Example of a fine piecewise-constant volume discretization used to obtain higher-order basis functions.

It becomes crucial that S^n spans the entire range of desired operating frequencies. In addition, the frequency samples should be fine enough so that the interpolation of the resulting sampled currents faithfully captures their overall variation with frequency. The combination of such spatial and frequency sampling subsequently generates a collection V_{pn} of source current solutions with $V_{pn} = \{\overline{v}_i\}, i = 1 \ldots p \times n$.

3 It becomes evident that the span of matrix V_{pn} captures a conductor's cross-sectional current distribution, accounting for both frequency-dependent skin effects and frequency plus spatial-dependent proximity effects. Therefore the subspace spanned by V_{pn} can be used to generate a set of specialized basis functions. More specifically, let's determine q ($q \ll p \times n$, $q \ll \eta$) such linearly-independent basis functions, the collection of which, $U = \{\overline{u}_1, \overline{u}_2, \ldots \overline{u}_q\}$, approximates V_{pn}. The accuracy of the approximation is measured by the minimal distance, in a least square sense, between the span of U and V_{pn}. To satisfy this minimization requirement, a singular-value-decomposition (SVD) method is used to generate these q orthogonal basis functions from the q dominant singular vectors of V_{pn}. Each one of these q basis functions can be viewed as a mode representing an orthogonally decomposed current distribution shape over a conductor's cross section. Therefore a weighted sum of these current distribution modes is capable of accounting for the cross-sectional current distribution at any particular frequency point within the range from which the basis functions are

generated.

In practice, at most 8 of these specialized basis functions ($q = 8$) are needed to accurately capture current distributions in most cross-section shapes over a wide span of frequencies. In contrast, a much larger number ($\eta \gg 8$) of piecewise-constant basis functions is needed to capture the cross-sectional current variation at one frequency point, and this number grows rapidly with the increase in frequency. In addition, the frequency-independent nature of the specialized basis functions implies that they only need to be pre-computed once for each unique cross-section geometry and can be stored off-line for repeated use. Since the number of these basis functions is small, storage cost is negligible.

7.2 Post-optimization of Specialized Basis Functions

In this section, we will demonstrate how optimization can be applied to the set of basis functions $U = \{\overline{u}_1 \ldots \overline{u}_q\}$ constructed from the previous section in order to avoid numerical difficulties encountered when these basis functions are used to approximate unknown current densities in a conductor system.

According to (3.21), the current density distribution in the ith conductor segment can be approximated by a weighted sum of the basis functions in U as:

$$\overline{J}_i \approx \sum_{j=1}^{q} \frac{\overline{u}_j \hat{\ell}_i}{\sum \overline{u}_j} I_{ij}, \tag{7.1}$$

where current variation unique to a cross-section shape can be effectively captured by the span of U within a given frequency range. Coefficient I_{ij} denotes the weight corresponding to the jth basis function, $\overline{u}_j$, as it contributes to the overall current distribution in segment i. In turn, each $\overline{u}_j$ is a vector of η piecewise-constant filament currents, the union of which provides an accurate approximation of the cross-sectional current contained in the jth basis function mode. Quantity $\sum \overline{u}_j$ is the sum of these currents. The purpose of basis function normalization by $\sum \overline{u}_j$ is to explicitly define basis function weight I_{ij} as a physical current, the necessity of which has been firmly established in Sec. 3.5.2. However, the possibility that the total current contained in the jth basis function mode ($\sum \overline{u}_j$) might be zero signifies

that it might be necessary to additionally process the basis functions in U in order to prevent each normalized vector from blowing up. The problem can be mathematically formulated as:

> Given a basis function matrix U={$\overline{u}_i$, i=1..q}, where U is an orthonormal matrix with possible column sums being zero, we need to determine a set of coefficients {α_{ij}, i=1..q, j=1..q} such that
>
> $$\overline{m}_j = \sum_{i=1}^{q} \alpha_{ij} \overline{u}_i, \tag{7.2}$$
>
> where $\overline{m}_j$ forms a column of a new basis function matrix M={$\overline{m}_j$, j=1..q}. M is subjected to the following constraints in terms of α:
>
> - *Orthogonality:* $\left(\overline{m}_k \cdot \overline{m}_\ell \approx 0 \text{ if } k > \ell\right)$
>
> $$-\epsilon < \left(\sum_{i=1}^{q} \alpha_{ik} \overline{u}_i\right)^T \left(\sum_{i=1}^{q} \alpha_{i\ell} \overline{u}_i\right) < \epsilon \;\; if \;\; k > \ell, \tag{7.3}$$
>
> where ϵ is a small constant.
>
> - *Nonzero column sums:* $\left(\sum \overline{m}_j > \beta\right)$
>
> $$\left| \left(\sum_{i=1}^{q} \alpha_{ik} \overline{u}_i\right)^T ones(\eta) \right| > \beta, \tag{7.4}$$
>
> where β is a positive non-zero constant and $ones(\eta)$ is a η-length vector of one's.

The problem is now formulated so that a standard optimization technique can be applied to solve the q^2 unknown α's, thus yielding a new ortho-normal basis function matrix M having the same span as the original matrix U, but guaranteeing nonzero column sums.

7.3 Incorporation of Basis Functions into MPIE

This section demonstrates how the collection of such modal basis functions, obtained using the procedure in Sec. 7.1 and optimized using the method in Sec. 7.2, is incorporated into

the MPIE formulation to produce a reduced system of equations for the potentials of a large interconnect network.

After replacing U in (7.1) by the optimized set of basis functions $M(=\{\overline{m}_j\}; j = 1 \ldots q)$, one is able to use the new basis functions in a Galerkin technique to produce a linear system of equations for the unknown basis function weights. To obtain partial resistance R_{ij} in (3.26) in terms of basis function vectors $\overline{m}_i$ and $\overline{m}_j$, the following approximation can be made:

$$R_{ij} \approx \frac{1}{\sigma \sum_{k=1}^{\eta} m_{i_k} \sum_{k=1}^{\eta} m_{j_k}} \sum_{k=1}^{\eta} m_{i_k} m_{j_k} \frac{l_{i_k}}{a_{i_k}},$$

where m_{i_k} is the kth piecewise-constant current in the ith mode, l_{i_k} and a_{i_k} are the length and cross-sectional area, respectively, of the filament on which the kth piecewise-constant current of the ith mode is defined. If there are n conductor segments in the discretized system and q basis function modes for each segment, then R is a block-diagonal matrix of size $qn \times qn$ with each block being $q \times q$.

Similarly, for the calculation of partial inductance L_{ij} in (3.27):

$$L_{ij} \approx \frac{1}{\sum_{k=1}^{\eta} m_{i_k} \sum_{k=1}^{\eta} m_{j_k}} \sum_{k_1=1}^{\eta} \sum_{k_2=1}^{\eta} m_{i_{k_1}} m_{j_{k_2}} \int_{v_{i_{k_1}}} \int_{v_{j_{k_2}}} \overline{\overline{G}}_A(r, r', \omega) \hat{\ell}_i \cdot \hat{\ell}_j dr' dr. \qquad (7.5)$$

Therefore L is a dense matrix of size $qn \times qn$. The system setup cost associated with computing the integrals of higher-order basis functions, as in (7.5), is actually the same as those involving piecewise-constant basis functions. Furthermore, the accelerated integration techniques introduced in the previous chapter for piecewise-constant basis functions can still be applied to the higher-order basis functions introduced in this paper. More importantly, due to the fact that $q \ll \eta$, R and L matrices produced by the use of the specialized basis functions are much smaller in comparison to the use of piecewise-constant basis functions, which yields, instead, matrices of size $\eta n \times \eta n$.

7.4 Chapter Summary

In this chapter, a procedure for the automatic generation of specialized basis functions is presented. The resulting set of high-order basis functions, unique to a conductor's cross-sectional geometry, is capable of generating system matrices for the MPIE that are much

reduced in size in comparison to that of piecewise-constant basis functions. This is because the specialized basis functions are derived to parameterize the frequency-dependent nature of a conductor's cross-sectional current variation, hence capable of capturing electromagnetic phenomenon such as skin and proximity effects over a wide range of frequencies. The basis functions themselves are frequency-independent within a specified frequency range of operation. Therefore they only need to be pre-computed once for each conductor cross-section type and can be stored off-line with a minimal cost for the purpose of future use. In addition, these basis functions have proven to bear the same computational cost as piecewise-constant basis functions if used in a Galerkin scheme for the solutions of the MPIE.

Chapter 8

FastSub: a pFFT-accelerated Integral Equation Solver

The techniques described in the body of this thesis culminate into the implementation of an electromagnetic integral equation solver called FastSub. This solver is capable of performing interconnect impedance extractions in the presence of a conductive substrate and over a wide range of operating frequencies. Numerous novel schemes are implemented in the solver to enhance its overall performance, some which have been extensively discussed in the previous chapters, but others are yet to be explained. These techniques of acceleration include:

- Accelerated volume and surface integration schemes (Chap.6).
- Frequency-parameterizing, yet frequency-independent specialized basis functions (Chap.7).
- Pre-corrected Fast-Fourier Transform (pFFT) method tailored to the utilization of dyadic Green's functions.

The last method is the focus of discussion in this chapter. Rather than providing detailed description regarding every aspect of pFFT, many of which can be found in the works of [55, 56, 84], the purpose of this chapter is to highlight the extensions made to the existing pFFT in order to accommodate dyadic Green's functions.

8.1 Preliminaries

In order to use a Krylov-based iterative method to solve a discretized system such as the one in (3.51), one needs to consider the fact that the dominating cost of such a method is the dense matrix-vector product Ax_i, which produces an overall computational complexity of $O(n^2)$, with n^2 being the number of non-zeros in the matrix. In our problem, $A = [MZ_{em}M^T]$ and $x_i = I_{m_i}$. However, exploiting the physical structure of the problem, one can reduce the computational complexity of the matrix-vector product to $O(n \log n)$ utilizing pFFT. The theoretical principle behind this method rests on the observation that in (3.46), the product of LI, where L is a dense matrix of size $m \times m$, corresponds to the computation of magnetic potentials in m filaments generated by m currents (I) flowing through the same filaments. Similarly, the product Pq, where P is a dense matrix of size $n \times n$, corresponds to the computation of scalar potentials on n panels generated by n charges (q) residing on the same panels. Using the former interaction as an example, the procedure utilized in pFFT to approximate the computation of magnetic vector potentials can be summarized as:

- *Projection:* Superimpose a three-dimensional grid onto the entire physical space of interest. Project each filament current I onto a set of nearby grid points or stencils surrounding the filament. This projection is done such that the potential produced by the new grid currents is the same as the potential produced by the original filament current on far away grid points. Consequently, a sparse projection matrix P is produced, where P is of size $N_g \times N_b$, where N_g is the number of grid points, and N_b is the number of basis functions.

- *Convolution:* The grid potentials generated by the current on the same grid points can be easily computed using a convolution operation in the spatial domain. Such convolution can be handled by a Fast-Fourier Transformation (FFT). Hence a convolution matrix H is produced where H is of size $N_g \times N_g$.

- *Interpolation:* The computed grid potentials can be interpolated onto the filaments to approximate filament potentials. Hence a sparse interpolation matrix I is generated with I being $N_b \times N_g$.

- *Direct computation and pre-correction:* Accuracy of the above procedure deteriorates

rapidly for nearby filament interactions. Therefore contributions of nearby filament currents must be computed directly and care must be taken to remove the grid potential contributions of those direct-interacting filaments. The resulting direct matrix D and pre-correction matrix Pc are both sparse and of sizes $N_b \times N_b$.

- *Putting it all together:*

$$Ax_i \approx \Big([D - Pc] + [I][H][P] \Big) x_i. \tag{8.1}$$

Of course, the same procedure can be applied to the computation of electric scalar potentials on panels. Thus far, the pFFT technique has only been extensively applied to accelerations involving scalar Green's functions. This chapter demonstrates how pFFT can be extended to include acceleration of matrix-vector products involving the dyadic Green's function kernels encountered in our problem.

In our problem, the integral equation used to compute the magnetic vector potential for each entry of the inductance matrix L can be expressed as:

$$\begin{aligned} A_{ij} &= \int_{v_i} dr\; w_i(r)\hat{\ell}_i^* \cdot \int_{v_j} dr'\; \overline{\overline{G}}_A(r,r') w_j(r')\hat{\ell}_j \\ &= \hat{\ell}_i^* \cdot \Big(\int_{v_i} dr\; w_i(r) \int_{v_j} dr'\; \overline{\overline{G}}_A(r,r') w_j(r') \Big) \hat{\ell}_j, \end{aligned} \tag{8.2}$$

where v_i and v_j are the volume supports for basis functions $w_i(r)$ and $w_j(r)$, respectively. Vectors $\hat{\ell}_i$ and $\hat{\ell}_j$ are the directions of current flow in volumes v_i and v_j, respectively. Dyad G_A is the layered Green's function as derived in the previous chapter of this thesis and has the following dyadic form:

$$\overline{\overline{G}}_A = \begin{bmatrix} G_A^{xx} & 0 & 0 \\ 0 & G_A^{yy} & 0 \\ G_A^{xz} & G_A^{yz} & G_A^{zz} \end{bmatrix}, \tag{8.3}$$

where $G_A^{yy} = G_A^{xx}$.

According to the method of complex images, scalar components G_A^{xx}, G_A^{yy} and G_A^{zz} can be expressed by the following generalized representation:

$$\begin{aligned} G_A^{vv}(r,r') &= G_{A_{real}}^{vv}(r,r') + G_{A_{images}}^{vv}(r,r') \\ &= g(x-x',y-y',z-z') + \sum_i a_i\, g(x-x',y-y',z+z'-jb_i), \end{aligned} \tag{8.4}$$

where subscript vv indicates a diagonal component of the dyadic Green's function in (8.3). In the above equation, $G_{A_{real}}^{vv}$ corresponds to the potential generated by real filament interactions in the absence of the substrate. $G_{A_{images}}^{vv}$ corresponds to the potential generated by complex-image filaments on real filaments, and $a_i's$ and $b_i's$ are the complex coefficients and exponents of the images, respectively. Both $G_{A_{real}}^{vv}$ and $G_{A_{images}}^{vv}$ can be expressed in terms of free-space Green's function g.

The off-diagonal component G_A^{xz}, on the other hand, has the following differential form with respect to the x-direction:

$$G_A^{xz}(r,r') = \sum_i a_i \frac{\partial}{\partial x'} g(x-x',y-y',z+z'-jb_i). \tag{8.5}$$

Similarly, the off-diagonal component G_A^{yz} has the following differential form with respect to the y-direction,

$$G_A^{yz}(r,r') = \sum_i a_i \frac{\partial}{\partial y'} g(x-x',y-y',z+z'-jb_i). \tag{8.6}$$

Note that both G_A^{xz} and G_A^{yz} are generated by only complex image filaments.

8.2 Projection and Interpolation

It should be noted that the variant of the pFFT method employs polynomial projection and interpolation schemes, hence producing projection and interpolation matrices that are independent of the specific underlying Green's function [55]. This makes it much easier to handle complex Green's function kernels and, from an implementation point of view, provides a unified framework regardless of basis function types or particular method of

evaluation. However, projection and interpolation schemes do depend on the type of applied operators to the inner and outer integration kernels.

First, consider the case of projection. The double volume integration of the dyadic Green's function kernel can be decomposed into the double volume integrations of five scalar kernels. These scalar kernels can be placed into three categories based on the type of applied operators to the green's functions in (8.4)-(8.6). In (8.5), an inner differential operator $\frac{d(.)}{dx'}$ is applied to its free-space green's functions. In (8.6), $\frac{d(.)}{dy'}$ is applied. In (8.4), an identity operator is applied. Therefore, according to the projection principle [84], different projection matrices need to be produced for these different inner integral operator types. It is clear that the projection of our dyadic Green's function cannot be treated as an encapsulated unit. Rather, projection should be considered on an individual basis for each scalar component of the dyadic Green's function. Consequently three projection matrices, P_F, $P_{\frac{dF}{dx}}$ and $P_{\frac{dF}{dy}}$ are produced for our problem [85].

From (8.2), one observes that the scalar kernels of the dyadic Green's function all share the same identity operator in the outer integral. Hence only one interpolation matrix I is suffice for our problem.

8.3 Convolution and Grid-generation Constraints

In (8.4), one notices that even though the first term $G^{vv}_{A_{real}}$ is shift invariant in all directions, the second term $G^{vv}_{A_{images}}$ is only shift invariant along the x-y plane. Particularly, its dependence on $z + z'$ adds complexity to the overall pFFT approach. A similar observation is made for (8.5) and (8.6), where only image contributions are present.

The additional complexity in FFT due to the presence of layered interface is resolved by [55], according to which the matrix that maps grid current to grid potentials is the sum of a matrix with block-toeplitz structure corresponding to the first term of (8.4), and a matrix with block-Hankel structure corresponding to the second term of (8.4). The Toeplitz matrix is generated from the discrete convolution of the free-space Green's function and can be treated with an ordinary FFT technique. The Hankel matrix is related to a Toeplitz matrix via a simple permutation matrix, therefore multiplication by a Hankel matrix is also $O(N \log N)$ via the FFT. Furthermore, the permutation matrix may be represented in Fourier space so that multiplication of a vector by the sum of a Hankel and a Toeplitz

matrix can be performed using a single forward and inverse FFT pair.

In our problem, we have assumed that all conductor structures occupy only the topmost layer of the layered medium. Hence the grid generation step is essentially the same as the case of free space. However, care much be taken to ensure that the grid is always above the plane of interface and never crosses below to the substrate region.

8.4 Direct Matrix and Pre-correction

As mentioned earlier, the nearby interactions should be computed directly and the inaccurate contributions from the use of grid should be removed. Since there are three different types of projection schemes involved in our problem, the dyadic Green's function cannot be treated as a single unit when it comes to the computation of direct interactions and the removal of grid contributions. Rather, they should be applied individually to each scalar component of the dyadic Green's function. Hence a direct matrix is generated for each unique scalar component, producing D^{xx}, D^{zz}, D^{xz} and D^{yz}. In addition, pre-correction matrices are produced unique to each component, hence generating pre-correction matrices Pc^{xx}, Pc^{zz}, Pc^{xz} and Pc^{yz}.

8.5 Algorithm Summary

The following algorithm summarizes the pFFT approach developed for the computation of magnetic vector potentials $\overline{A} = [A_x, A_y, A_z]$ due to the excitation of vector currents $\overline{I} = [I_x, I_y, I_z]$ in the presence of a substrate:

1. Construct projection matrices P_F, $P_{\frac{dF}{dx}}$, $P_{\frac{dF}{dy}}$.

2. Construct interpolation matrix I.

3. Construct direct-interaction matrices D^{xx}, D^{zz}, D^{xz} and D^{yz}.

4. Construct pre-correction matrices Pc^{xx}, Pc^{zz}, Pc^{xz} and Pc^{yz}.

5. FFT projected inputs:

   . $\hat{I}_x = \text{FFT}([P_F]I_x)$ $\qquad\qquad$ $\hat{I}_{x_{image}} = \text{reflect}(\hat{I}_x)$

- $\hat{I}_y = \text{FFT}\big([P_F]I_y\big)$ $\qquad\qquad$ $\hat{I}_{y_{image}} = \text{reflect}(\hat{I}_y)$
- $\hat{I}_z = \text{FFT}\big([P_F]I_z\big)$ $\qquad\qquad$ $\hat{I}_{z_{image}} = \text{reflect}(\hat{I}_z)$
- $\hat{I}_{x_{image2}} = \text{reflect}\Big(\text{FFT}\big(\big[P_{\frac{dF}{dx}}\big]I_x\big)\Big)$
- $\hat{I}_{y_{image2}} = \text{reflect}\Big(\text{FFT}\big(\big[P_{\frac{dF}{dy}}\big]I_y\big)\Big)$

6. FFT scalar Green's function components:

- $\tilde{H}_{toeplitz}(G^{xx}_{A_{real}}) = \text{FFT}(G^{xx}_{A_{real}})$ $\qquad\qquad$ $\tilde{H}_{hankel}(G^{xx}_{A_{image}}) = \text{FFT}(G^{xx}_{A_{image}})$
- $\tilde{H}_{toeplitz}(G^{zz}_{A_{real}}) = \text{FFT}(G^{zz}_{A_{real}})$ $\qquad\qquad$ $\tilde{H}_{hankel}(G^{zz}_{A_{image}}) = \text{FFT}(G^{zz}_{A_{image}})$
- $\tilde{H}_{hankel}(G^{xz}_{A_{image}}) = \text{FFT}(G^{xz}_{A_{image}})$
- $\tilde{H}_{hankel}(G^{yz}_{A_{image}}) = \text{FFT}(G^{yz}_{A_{image}})$

6. Convolution:

- $\hat{A}_x = \tilde{H}_{toeplitz}(G^{xx}_{A_{real}})\hat{I}_x + \tilde{H}_{hankel}(G^{xx}_{A_{image}})\hat{I}_{x_{image}}$
- $\hat{A}_y = \tilde{H}_{toeplitz}(G^{xx}_{A_{real}})\hat{I}_y + \tilde{H}_{hankel}(G^{xx}_{A_{image}})\hat{I}_{y_{image}}$
- $\hat{A}_z = \tilde{H}_{toeplitz}(G^{zz}_{A_{real}})\hat{I}_z + \tilde{H}_{hankel}(G^{zz}_{A_{image}})\hat{I}_{z_{image}} + \tilde{H}_{hankel}(G^{xz}_{A})\hat{I}_{x_{image2}} + \tilde{H}_{hankel}(G^{yz}_{A})\hat{I}_{y_{image2}}$

7. Inverse FFT and interpolate:

- $A_x = [I]\text{FFT}^{-1}(\hat{A}_x)$
- $A_y = [I]\text{FFT}^{-1}(\hat{A}_y)$
- $A_z = [I]\text{FFT}^{-1}(\hat{A}_z)$

8. Pre-correction:

- $A_x = A_x + (D^{xx} - Pc^{xx})I_x$
- $A_y = A_y + (D^{xx} - Pc^{xx})I_y$
- $A_z = A_z + (D^{xz} - Pc^{xz})I_x + (D^{yz} - Pc^{yz})I_y + (D^{zz} - Pc^{zz})I_z$

Chapter 9

Results

This chapter contains various examples that demonstrate the efficiency and accuracy of the solver presented in the thesis. The purpose of the first section is to establish the efficiency of the solver due its use of the novel accelerated integration schemes. The purpose of the second section is to validate the overall simulation techniques described in the thesis by comparing measurement data obtained on fabricated devices to the results produced from our solver simulation. Examples in the third section seek to demonstrate the solver's versatility of application in various design areas. For instance, examples are presented to demonstrate the solver's ability to analyze the effects of design parameter and substrate conductivity variations on impedance and to account for full-wave effects at the integrated-circuit level. The last section of this chapter contains examples that conclusively establish the superior efficiency with which the specialized high-order basis functions are capable of capturing conductor cross-sectional current distributions when compared to piecewise-constant basis functions.

9.1 Computational Cost Comparisons

This section presents cost analysis and comparison of utilizing the accelerated integration scheme as opposed to a standard 3D Gaussian quadrature approach for the volume filament integration of a Type I kernel and a Type II kernel with an associated x-directed derivative. The source filament is $1um$ x $1um$ in the cross-section and $500um$ in length. The potentials are evaluated $2.5um$ and $10um$ from the center of the filament at an operating frequency

of $30GHz$.

Tables 9.1 and 9.2 show that, in comparison to the standard 3D Gaussian quadrature scheme, an average of 14X reduction in computational cost is achieved when the accelerated integration scheme is used for close-field potential calculation and an average of 7X cost reduction is achieved when the accelerated integration scheme is used for intermediate-field potential calculation.

Accuracy (%)	3D Gaussian quadrature (pts #)	1D accelerated method (pts #)	cost reduction
0.1	266	20	13X
1	160	10	16X
4	98	6	16X

Table 9.1: Cost analysis for the volume integration of a Type I kernel evaluated at a distance of $2.5um$ from the filament center.

Accuracy (%)	3D Gaussian quadrature (pts #)	1D accelerated method (pts #)	cost reduction
0.1	90	10	9X
1	42	6	5.25X
4	28	4	7X

Table 9.2: Cost analysis for the volume integration of a Type I kernel evaluated at a distance of $10um$ from the filament center.

For the potential evaluation consisting of the Type II kernel, tables 9.3 and 9.4 show that averages of 17X and 10X cost reductions are achieved corresponding to near-field and intermediate field evaluations, respectively.

Accuracy (%)	3D Gaussian quadrature (pts #)	1D accelerated method (pts #)	cost reduction
0.1	450	28	16X
1	320	18	17X
4	250	12	20X

Table 9.3: Cost analysis for the volume integration of a Type II kernel with an associated x-directed derivative. The kernel is evaluated at a distance of $2.5um$ from the filament center.

Accuracy (%)	3D Gaussian quadrature (pts #)	1D accelerated method (pts #)	cost reduction
0.1	110	12	9X
1	80	8	10X
4	62	6	10X

Table 9.4: Cost analysis for the volume integration of a Type II kernel with an associated x-directed derivative. The kernel is evaluated at a distance of $10um$ from the filament center.

9.2 Accuracy Validation Against Measurements

This section contains four examples that validate the accuracy of our solver when compared to actual measurement data collected by [54] on four fabricated RF spiral inductors of various dimensions.

9.2.1 A Square $2.25mm^2$-area, 1.75-turn RF Inductor

The first example is run on a square 1.75-turn spiral RF inductor with an area of $2.25mm^2$ as shown in Fig. 9-1. This inductor is fabricated on a multi-chip module (MCM) [54] using copper wires that are $5\mu m$ thick and $65.9\mu m$ wide. The separation distance between the turns is $34.1\mu m$. A guard ring that is $125\mu m$ wide and $5\mu m$ thick is placed $200\mu m$ from the RF-inductor to simulate a nearby ground. This structure is embedded in a dielectric and situated $180\mu m$ above a substrate. The dielectric has a resistivity(ρ) of $1.0x10^{17}\Omega \cdot cm$ and a relative permittivity (ϵ_r) of 3.5. The material properties of the substrate are: $\rho = 1.0x10^{14}\Omega \cdot cm$ and $\epsilon_r = 9.9$. Fig. 9-2 shows a plot of quality factors (Q-factors) obtained for this RF inductor excited over a range of frequency inputs. One set of Q-factor data is produced from measurements while the other set is from the solver introduced in this thesis.

9.2.2 A Square $4mm^2$-area, 2.75-turn RF Inductor

The second example is run on a square 2.75-turn spiral RF inductor with an area of $4mm^2$ as shown in Fig. 9-3. The metal and substrate material properties for this example are the same as those in the first example. This 2.75-turn inductor is composed of wires that are $5\mu m$ thick and $67.1\mu m$ wide. The separation distance between the turns is $45.4\mu m$. The

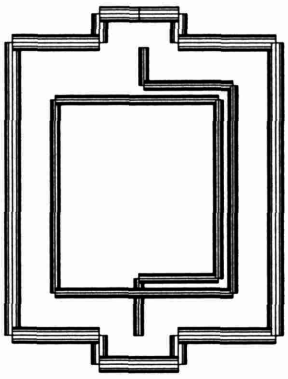

Figure 9-1: A square 1.75-turn RF inductor with an area of 2.25 mm^2 and surrounded by a ground ring.

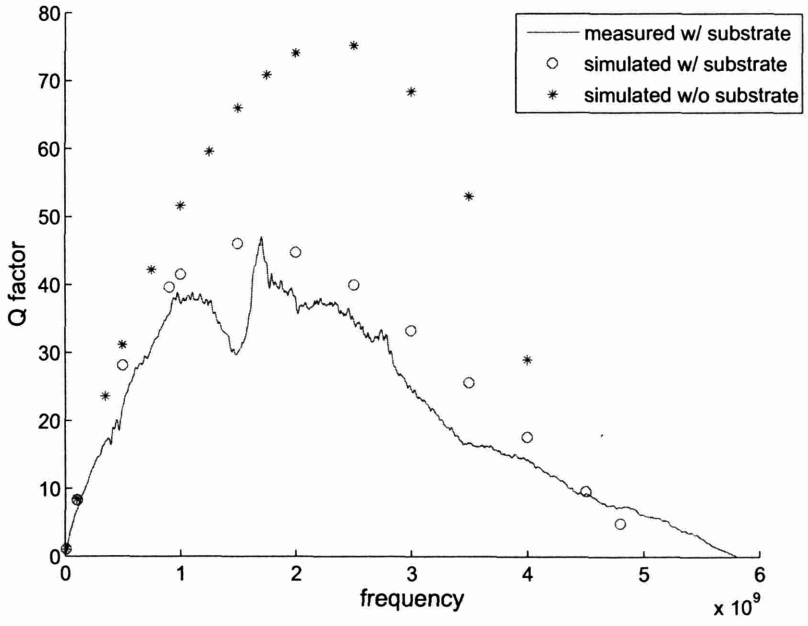

Figure 9-2: Measured and simulated Q-factors for the RF inductor described in Fig. 9-1.

inductor is situated at the same distance from the substrate as that of the first example and is surrounded by a similar ground ring. Fig. 9-4 shows a plot of the Q-factor comparison obtained for this inductor.

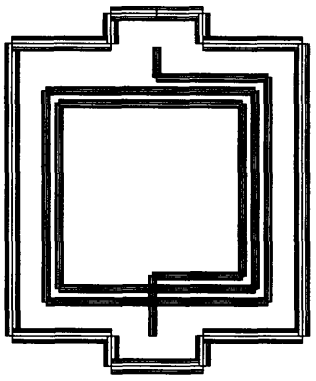

Figure 9-3: A square 2.75-turn RF inductor with an area of 4 mm^2 and surrounded by a ground ring.

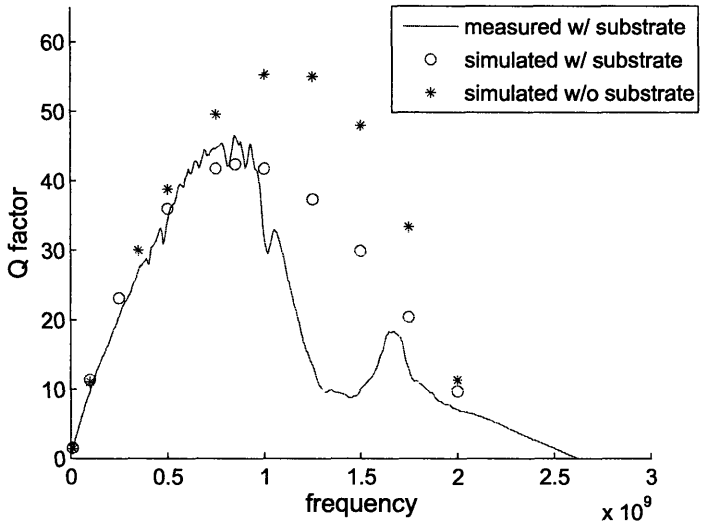

Figure 9-4: Measured and simulated Q-factors for the RF inductor described in Fig. 9-3.

9.2.3 A square 2.25mm^2-area, 3.75-turn RF Inductor

The third example is a square 3.75-turn spiral RF inductor with an area of 2.25mm^2 as shown in Fig. 9-5. The metal and substrate material properties used in this example are the same as those in the first example. This 3.75-turn inductor is composed of wires that are 5μm thick and 61.6μm wide. The separation distance between the turns is 38.4μm. The

inductor is situated at the same distance from the substrate as that of the first example and is surrounded by a similar ground ring. Fig. 9-6 shows a plot of Q-factor comparison obtained for the 3.75-turn inductor.

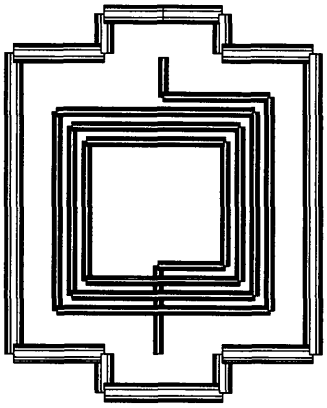

Figure 9-5: A square 3.75-turn RF inductor with an area of $2.25mm^2$ and surrounded by a ground ring.

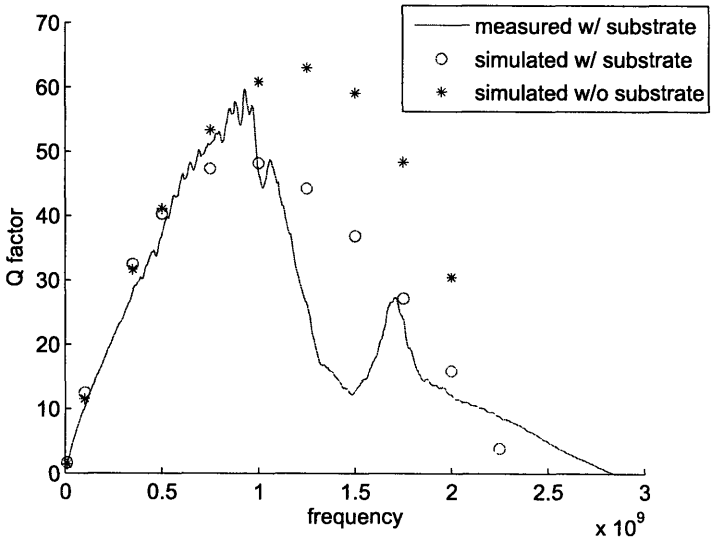

Figure 9-6: Measured and simulated Q-factors for the RF inductor described in Fig. 9-5.

9.2.4 A square $2.25mm^2$-area, 4.75-turn RF Inductor

The last example of this section is a square 4.75-turn spiral RF inductor with an area of $2.25mm^2$ as shown in Fig. 9-7. This 4.75-turn inductor is composed of wires that are $5\mu m$ thick and $37.6\mu m$ wide. The separation distance between the turns is $24.95\mu m$. Fig. 9-8 shows a plot of Q-factor comparison obtained for the 4.75-turn inductor.

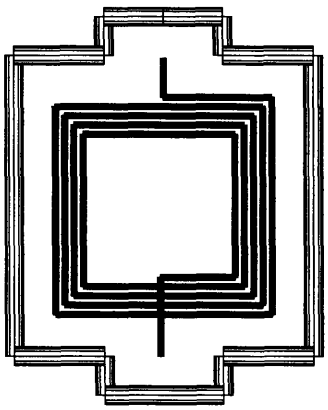

Figure 9-7: A square 4.75-turn RF inductor with an area of $2.25mm^2$ and surrounded by a ground ring.

Measuring Q-factors on fabricated RF inductors is a difficult task, and measurements are typically noisy; nevertheless, Figs. 9-2, 9-4, 9-6, and 9-8 all demonstrate that simulation results obtained from our solver can accurately reflect the overall Q-factor behavior of fabricated devices. One interesting observation worth noting is that as the number of turns increases, the effect of the substrate becomes increasingly negligible. This is due to the fact that the parasitics created between metal windings dominate as the number of turns increases, hence rendering the effect of the substrate negligible.

9.3 Applied Examples

After thoroughly establishing the validity of our solver in the previous section, this section uses the solver to quantitatively analyze substrate effects on various IC structures with the purpose of showcasing the versatility of our solver in various application areas.

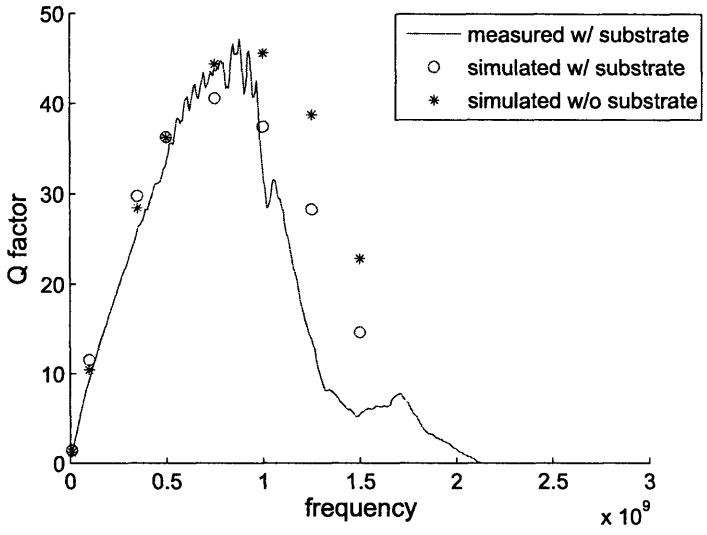

Figure 9-8: Measured and simulated Q-factors for the RF inductor described in Fig. 9-7.

9.3.1 Full-wave Effects on a MCM Transmission Line

This section studies full-wave substrate effects on a MCM transmission line. The transmission line is constructed using two copper wires that are $5\mu m$ thick, $10\mu m$ wide, and $3cm$ long. The two lines are situated $1cm$ apart at a height $180\mu m$ above the substrate in the oxide layer. The properties of the oxide layer and the substrate are the same as the MCM in the previous section.

In Fig. 9-9, one set of resistance results is generated in quasi-static mode where the full-wave kernels are replaced with the $\frac{1}{R}$ kernels, and the other set is generated in full-wave mode. In Fig. 9-9, the full-wave effects are manifested as discrepancies in the resonance peaks between the data generated in the full-wave mode and those in quasi-static mode. These discrepancies increase with frequency, reflecting on the full-wave mode's ability, or, the quasi-static mode's inability, to capture high-frequency radiation losses in the system.

9.3.2 Design Parameter Variation Effects on a RF Inductor

A clear advantage of our simulation tool is the ease for which parameter changes are modeled in a spiral inductor design in order to optimize its electrical behavior or examine its para-

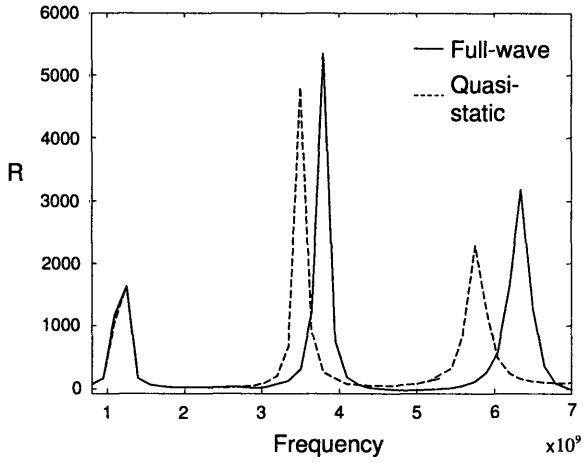

Figure 9-9: Resistance comparison between full-wave and quasi-static simulations on the transmission line structure in Sec. 9.3.1.

meter sensitivity. To illustrate this concept, we will examine the effects design parameter changes bear on spiral inductors' quality factor behavior over frequency. The square spiral inductors used in this example are composed of copper wires and embedded in a dielectric ($\epsilon_r = 3.9$) $7\mu m$ above a conducting silicon substrate ($\epsilon_r = 11.7$,$\rho = 1\Omega \cdot cm$). Each inductor layout has the following design parameters: metallization width (W), metallization thickness (T), separation distance between metal windings (SI), number of windings (N) and outer dimension (OD). We will start our analysis with the following nominal values: N=3, W=5μm, T=1μm, SI=2um, OD=400μm.

Variation on the number of windings (N)

The quality factor plots for five values of N are shown in Fig. 9-10. The self-resonance frequency (f_{SR}) decreases in a non-linear fashion with each additional winding due to the increase in capacitive coupling between the windings as well as to the substrate. In addition, the peak of quality factors decreases with increased metal loss introduced by the additional windings [24].

Variation on the separation distance (SI)

Fig. 9-11 shows the effect of varying metal spacing on the overall quality factor behavior of an inductor. A smaller spacing results in higher capacitive coupling between windings,

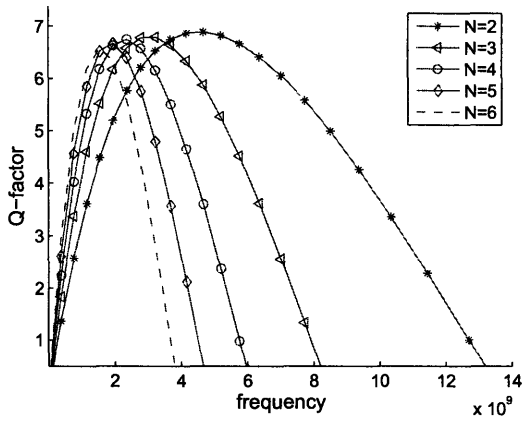

Figure 9-10: Quality factors for N=2, 3, 4, 5, 6 (W=5μm, T=1μm, SI=2μm, OD=400μm).

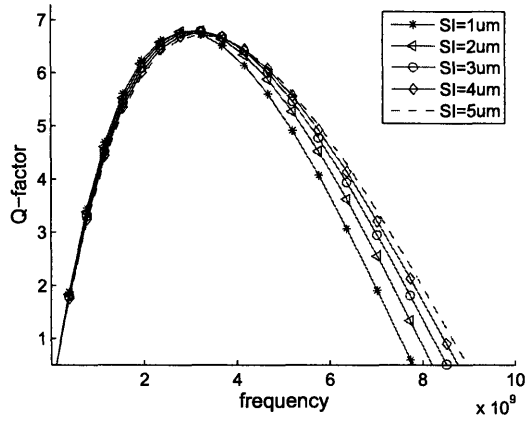

Figure 9-11: Quality factors for SI=1μm, 2μm, 3μm, 4μm, 5μm (W=5μm, T=1μm, N=3, OD=400μm).

hence leads to a lower f_{SR}. The peak of the quality factors, however, is not so sensitive to changes in separation distance.

Variation on the metallization width (W)

Fig. 9-12 shows the effect of varying metallization width on the overall quality factor behavior of an inductor. The larger surface area associated with wider metallization width results

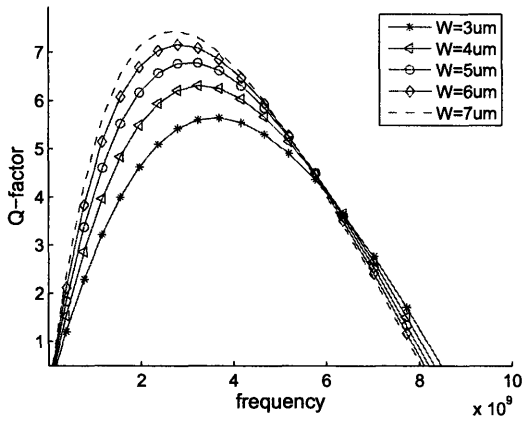

Figure 9-12: Quality factors for W=3μm, 4μm, 5μm, 6μm, 7μm (SI=2μm, T=1μm, N=3, OD=400μm).

in higher parasitic capacitances, which lowers the inductor's f_{SR} and increases its loss due to substrate dissipation. In addition, as metal line widens, ac resistance increases due to skin effects at a given frequency [42]. Thus quality factor peak shifts to a lower frequency as the conductor width increases.

9.3.3 Substrate Conductivity Effects on a Transmission Line

This section studies the effect of substrate conductivity variation on a transmission line structure. The transmission line is constructed using two copper wires that are $2\mu m$ thick, $10\mu m$ wide, and $100\mu m$ in length. The two lines are situated $110\mu m$ apart in an oxide layer ($\epsilon_r = 3.9$) at a height $5\mu m$ above a substrate of varying conductivities ($\sigma = 8\frac{S}{m}$, $\sigma = 800\frac{S}{m}$, $\sigma = 8000\frac{S}{m}$, $\epsilon_r = 11$). Figs. 9-13 and 9-14 present the simulated closed-circuit resistance and inductance, respectively, for such a configuration, and Fig. 9-15 presents its simulated open-circuit capacitance. These plots clearly show the influence of substrate skin effect on the resulting impedance.

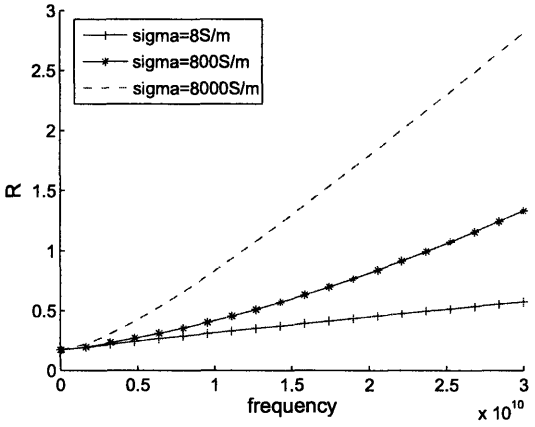

Figure 9-13: Closed-circuit resistance analysis for a transmission line structure in the presence of a substrate with a varying degree of conductivity.

Due to the strong skin effect in the substrate, the substrate resistance increases rapidly with frequency. This explains the overall increase in the resistance of the transmission line for the high conductivity case in Fig. 9-13. The figure also shows that this increase in resistance becomes weaker for decreasing substrate conductivities.

According to Fig. 9-14, as substrate conductivity and frequency increase, transmission line inductance decreases. This can be explained by the fact that increased skin effect diminishes the magnetic field's ability to penetrate into the substrate's interior, hence weakens the transmission line's inductance.

Capacitance behavior in Fig. 9-15 can be explained by the fact that at a high conductivity, the substrate acts as a ground plane for the electric field. Consequently, the transmission line's capacitance remains nearly constant for the cases of $\sigma = 800\frac{S}{m}$ and $\sigma = 8000\frac{S}{m}$ because the electric field is confined to only the oxide layer. However, for a low-conductivity substrate at high frequencies, the increased penetration of the electric field into the substrate leads to the observed reduction of capacitance in the case of $\sigma = 8\frac{S}{m}$.

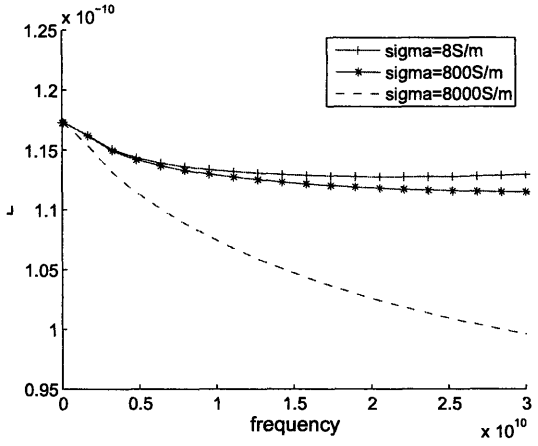

Figure 9-14: Closed-circuit inductance analysis for a transmission line structure in the presence of a substrate with various conductivities.

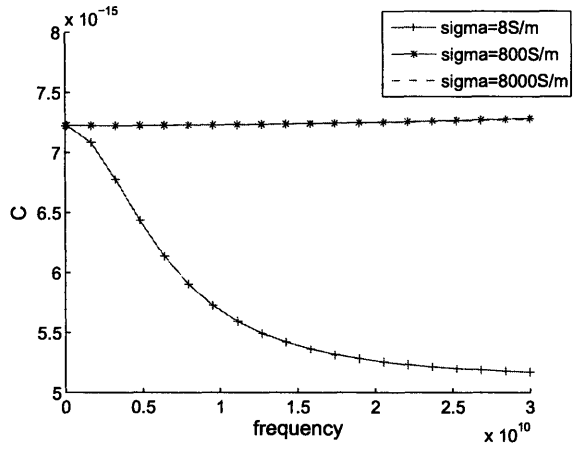

Figure 9-15: Open-circuit capacitance analysis for a transmission line structure in the presence of a substrate with a varying degree of conductivity.

9.3.4 Use of Ground Shielding for Substrate Loss Prevention

The goal of this section is to examine the optimality of using a patterned ground shield by analyzing its effect on the impedance of a spiral structure in comparison to the effect

generated without a shield or with a solid shield in the presence of a substrate.

The inductor structure with a patterned ground shield is shown in Figs. 9-16 and 9-17, taken from various viewing angles. The square 3-turn spiral RF inductor with an area of

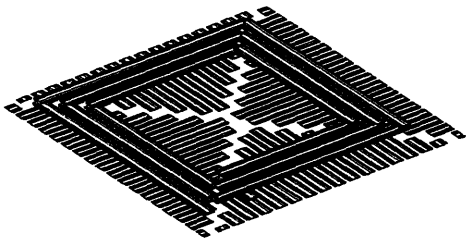

Figure 9-16: Angled view of a spiral inductor with a patterned ground shield.

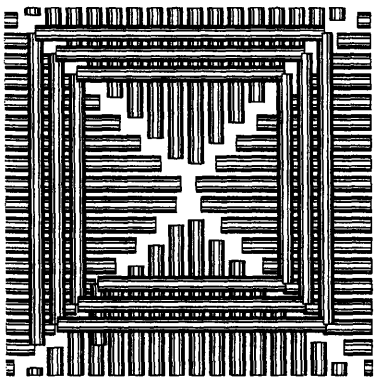

Figure 9-17: Top view of a spiral inductor with a patterned ground shield.

$0.09mm^2$ is composed of copper wires that are $2\mu m$ thick and $15\mu m$ wide. The separation distance between the turns is $5\mu m$. An underpass is situated $1\mu m$ below the inductor to contact the center of the spiral. The spiral and the ground shield are separated by $4.8\mu m$ of oxide ($\epsilon_r = 4$). The ground shield is separated from the silicon substrate ($\sigma = 10\frac{S}{m}$) by $0.4\mu m$ of oxide. To investigate the effect of shield pattern, a ground shield with $5\mu m$ slot width, $0.34\mu m$ slot thickness, and $20\mu m$ pitch is used. The shield is composed of a

polysilicon material ($\sigma = 2e4\frac{S}{m}$). The ground strips of the shield are merged together around the four outer edges of the spiral.

Figs. 9-18 shows the quality factor comparison obtained for the inductor in this example simulated without a shield, with a solid ground shield and with a patterned ground shield. From the results, it seems that having a patterned shield doesn't necessarily improve the quality factor of the spiral inductor in this example.

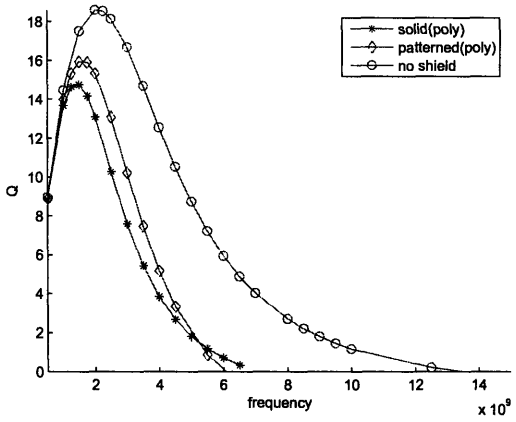

Figure 9-18: Quality-factor comparison obtained for the inductor structure with a patterned ground shield, a solid ground shield, and no shield.

9.4 Specialized High-order Basis Functions

This section utilizes our specialized high-order basis functions to efficiently extract the impedances of various complex IC structures. The basis functions are implemented in the context of our EM solver where a pre-corrected FFT (pFFT) scheme is introduced for the accelerated matrix-vector products involving dyadic Green's function kernels so that substrate effects can be accounted for. The specialized basis functions' efficiency is validated by comparing their performance to that of piecewise-constant basis functions.

9.4.1 Stacked Inductors

A set of specialized basis functions is first pre-computed in the frequency range of $[0.01\,MHz \ldots 10\,GHz]$ for trial copper wires with rectangular cross-sections that are $5\mu m$ thick and $10\mu m$ wide. Subsequently, impedance analysis utilizing the specialized basis functions is performed on four structures as shown in Fig 9-19.a,b,c,d, where each structure is embedded in a silicon oxide dielectric ($\epsilon_r = 3.9$) above a silicon substrate ($\epsilon_r = 3.9$, $\rho = 1\Omega \cdot cm$). For the three-

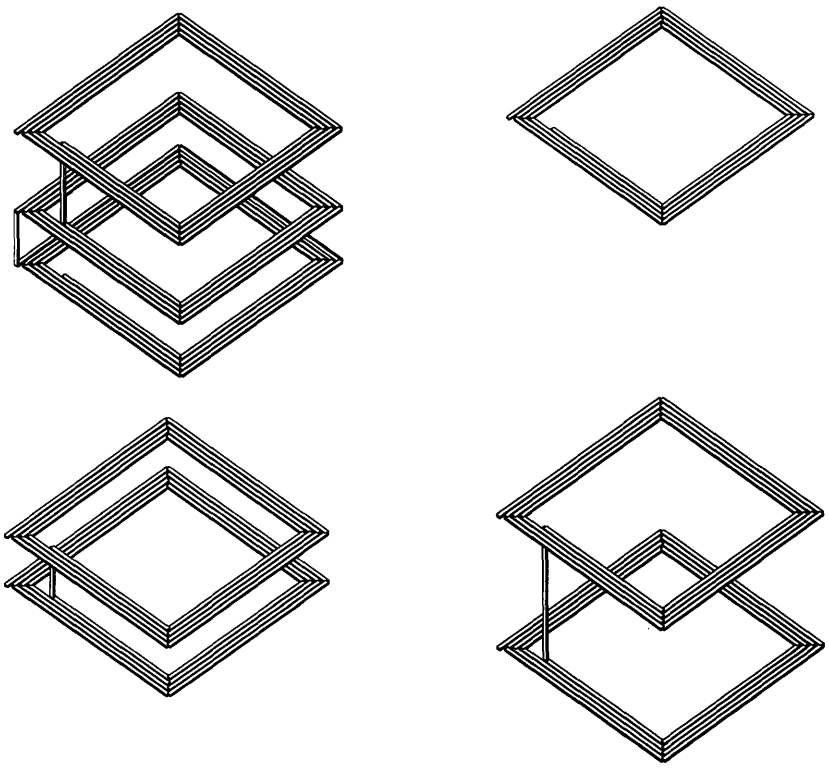

Figure 9-19: a. A three-layer M3-M2-M1 inductor. b. A one layer M3 inductor. c. A two-layer M3-M2 inductor. d. A two-layer M3-M1 inductor. Note that the structures are not drawn to scale for the sake of visual clarity.

layer M3-M2-M1 inductor in Fig. 9-19.a, the vertical heights of its three spirals are $16\mu m$, $26\mu m$ and $36\mu m$, respectively, above the silicon substrate. The single-layer M3 inductor in Fig. 9-19.b is composed from the topmost layer of the inductor in Fig. 9-19.a. The M3-M2 inductor of Fig. 9-19.c is composed from the top and middle layers of the three-layer in-

ductor. The M3-M1 inductor of Fig. 9-19.d is composed from the top and bottom layers of the same three-layer inductor. In turn, each inductor spiral is composed of a 4-turned copper wire that is $5\mu m$ thick and $10\mu m$ wide with a lateral dimension of $0.25mm^2$ and a separation distance of $2\mu m$ between metal windings.

Fig. 9-20 shows the error generated from the utilization of the high-order basis functions in comparison to the solution obtained from a fine piecewise-constant discretization scheme. For a maximum absolute error of only 0.25%, 8 specialized basis functions per conductor segment are needed in contrast to the requisite 48 piecewise-constant basis functions per segment to obtain the same amount of accuracy. The factor of 6× reduction in the number

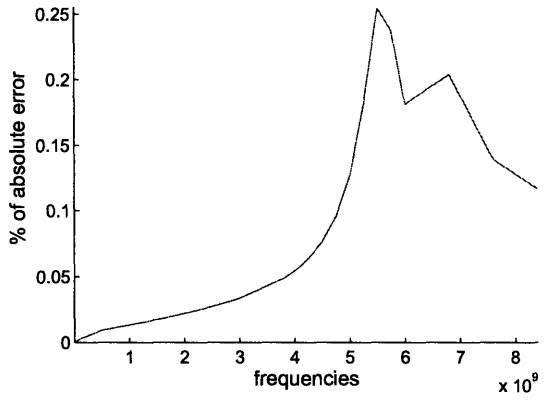

Figure 9-20: Error analysis for the usage of specialized high-order basis functions. Analysis is performed on the single-layer inductor example.

of basis functions translates to a significant 36× reduction in the computational cost of near-distance interactions when solving the system in a pre-corrected FFT ($pFFT$) scheme. This fact is confirmed by the FLOP (floating point operation) count decomposition in Table. 9.5 for each major stage of the pFFT scheme as it is applied to our single-layer inductor example. Note that even though the cost of assembling projection (P) and interpolation (I) matrices is only reduced by a factor of 8.6 for the use of higher-order basis functions, there exists a dramatic 36.28× reduction in the cost of pre-correction, an observation that collaborates our theory that by reducing the overall number of basis functions by a factor of N, one is able to reduce the cost of resolving nearby interactions, which cannot take advantage of the acceleration offered by pFFT, by a factor of N^2 as manifested at the pre-correction stage. Furthermore, the cost of iterative solve is reduced by a factor of 12, which is approximately

	piecewise-constant	Higher-order	reduction factor
# filaments	720	120	6
P and I matrices	1.9e5	2.3e4	8.3
D matrix	1.1e9	6.8e8	1.6
Pre-correction matrix	1.27e10	3.5e8	36.3
Iterative solve	1.18e8	9.4e6	12.6

Table 9.5: Flop count for the assembly of each pFFT stage for filament potential calculations of the single-layer inductor at frequency=1GHz.

O(Mlog$N$).

Additionally, Fig. 9-21 shows the quality factor analysis of the four inductor structures in this section. Their overall simulated behavior confirms the research conducted by [86] which

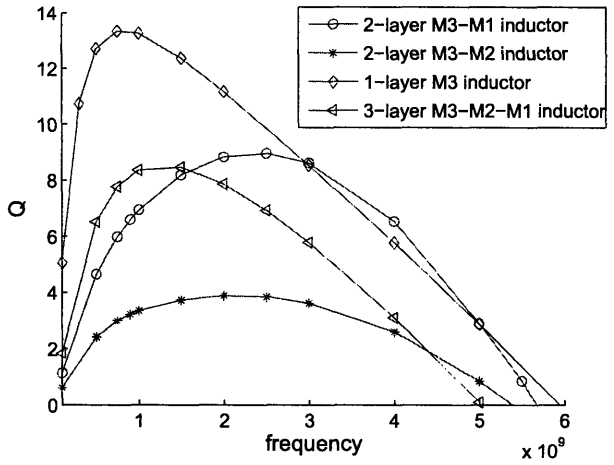

Figure 9-21: Quality factor analysis for the four inductors in Fig. 9-19.

theorizes that a stacked spiral inductor's self-resonance frequency (f_{SR}) can be drastically modified by the vertical placement of its spiral layers, and in some cases, by as much as 100%. Typically, a stacked structure exhibits a single $f_{SR} = \frac{1}{2\pi\sqrt{L_{eq}c_{eq}}}$, where L_{eq} and C_{eq} are the equivalent inductance and capacitance of the structure, respectively. Generally speaking, the inter-layer capacitance between the spirals has a much greater impact on f_{SR} than the layer-to-substrate capacitance. Hence increasing the stack separation distance diminishes the inter-layer capacitance while maintains a relatively constant inductance because the lateral dimensions of a stacked inductor are nearly two orders of magnitude greater than its

vertical dimension. Results in Fig. 9-21 confirm that this is indeed the case for our inductor examples. One observes that f_{SR} of the M3-M1 inductor is 25% greater than that of the M3-M2 inductor. Even more dramatic is the fact that f_{SR} of the M3-M1 inductor is 100% greater than that of the M3-M2-M1 inductor.

9.4.2 Conductor Array with Trapezoidal Cross-sections

A second set of specialized basis functions is pre-computed in the frequency range of $[1MHz \ldots 40GHz]$ for trial copper wires with trapezoidal cross-sections that are $1.2\mu m$ thick, $1\mu m$ wide on the top base and $0.6\mu m$ wide on the bottom base. Subsequently, impedance analysis is performed on an 8-conductor bus example with each conductor $300\mu m$ in length and separated $2\mu m$ from the neighboring wires. Fig. 9-22 offers a zoomed view of such configuration. The entire structure is embedded in a dielectric ($\epsilon_r = 3.9$) and situated $16\mu m$ above a conductive substrate ($\rho = 0.1\Omega \cdot cm$, $\epsilon_r = 11.7$). Due to the com-

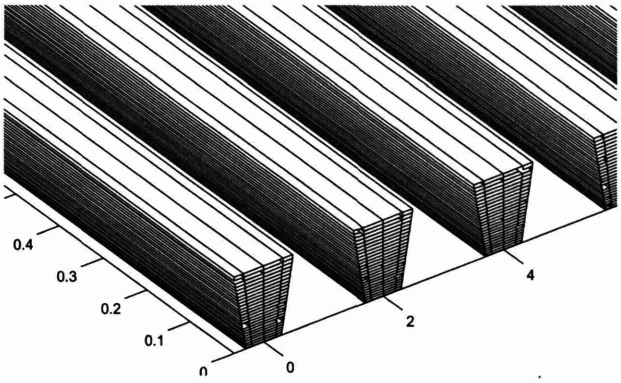

Figure 9-22: Structural view of an array of 8 conductors with trapezoidal cross-sections. Each conductor is $300\mu m$ in length with a cross-sectional dimension of $1.2\mu m$ in thickness, $1\mu m$ on the top base and $0.6\mu m$ on the bottom base. Separation distance between the conductors is $2\mu m$.

bined effects of irregular cross-sectional shape and skin and proximity phenomenon, each conductor's trapezoidal cross-section must be discretized finely if piecewise-constant basis functions were used. This concept is illustrated by the fine cross-sectional mesh shown in Fig. 9-22. To be specific, 104 piecewise-constant filaments per conductor are required for this particular example. In contrast, only 8 specialized higher-order basis functions are needed to capture the same conductor cross-sectional current distribution for a maximum

error of only 0.0072% as shown in Fig. 9-23. This is a factor of 13× reduction in the num-

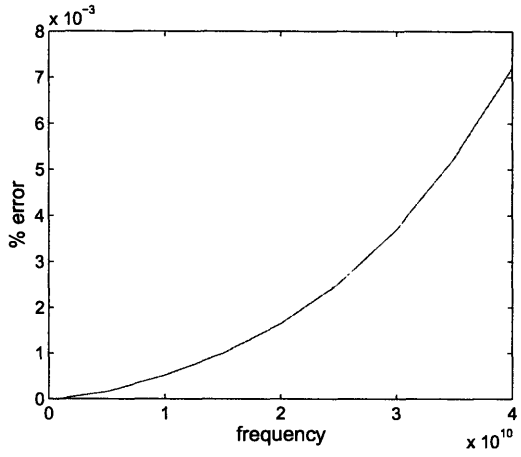

Figure 9-23: Error analysis for the usage of higher-order basis functions in comparison to the usage of piecewise-constant basis functions in the conductor array example in Fig. 9-22.

ber of basis functions, which translates to a reduction of 169× in the computational cost of near-distanced interactions when solving the system in a pre-corrected PFFT scheme. Flop count analysis in Table 9.6 confirms such claim. For the use of higher-order basis functions, the cost of constructing P and I matrices are reduced by a factor of 17, the cost of D matrix construction is comparable to that of piecewise-constant basis functions, but the cost of pre-correction is reduced by a factor of 170 and the cost of solving the system using an iterative method is reduced by a factor of 108.

	piecewise-constant	Higher-order	reduction factor
# filaments	832	64	13
P and I matrices	2.3e5	1.3e4	17.7
D matrix	2.8e9	1.6e9	1.8
Pre-correction matrix	1.7e10	1.0e8	170
Iterative solve	1.3e8	1.2e6	108.3

Table 9.6: Flop count for the assembly of each pFFT stage for filament potential calculations of the conductor array example at frequency=1GHz.

To further demonstrate the versatility of our solver, we can compare the impedances

extracted for the trapezoidal example to those extracted for the case where the conductors have rectangular cross-sections ($1.2\mu m$ thick and $0.8\mu m$ wide). Such configuration is shown in Fig. 9-24. The simulation setup is such that resistance and inductance are extracted

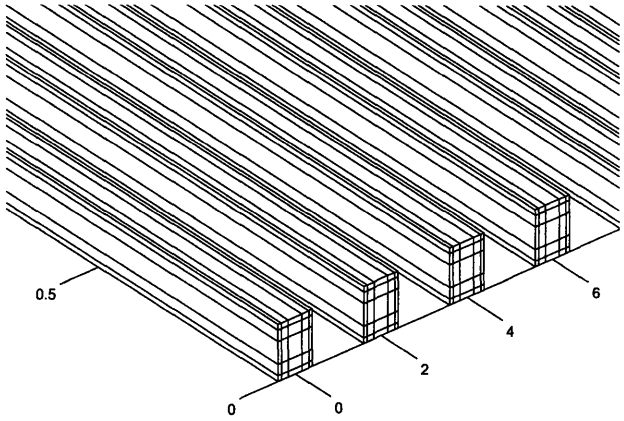

Figure 9-24: An array of 8 conductors with rectangular cross-sections. Each conductor is $300\mu m$ in length with a cross-sectional dimension of $1.2\mu m$ in thickness and $0.8\mu m$ in width. Separation distance between the conductors is $2\mu m$.

under the condition where the two center conductors are shorted at one end, while capacitance extractions are performed under an open-circuit condition. The resulting resistance, inductance, and capacitance comparisons are shown in Fig. 9-25.a, b, and c, respectively.

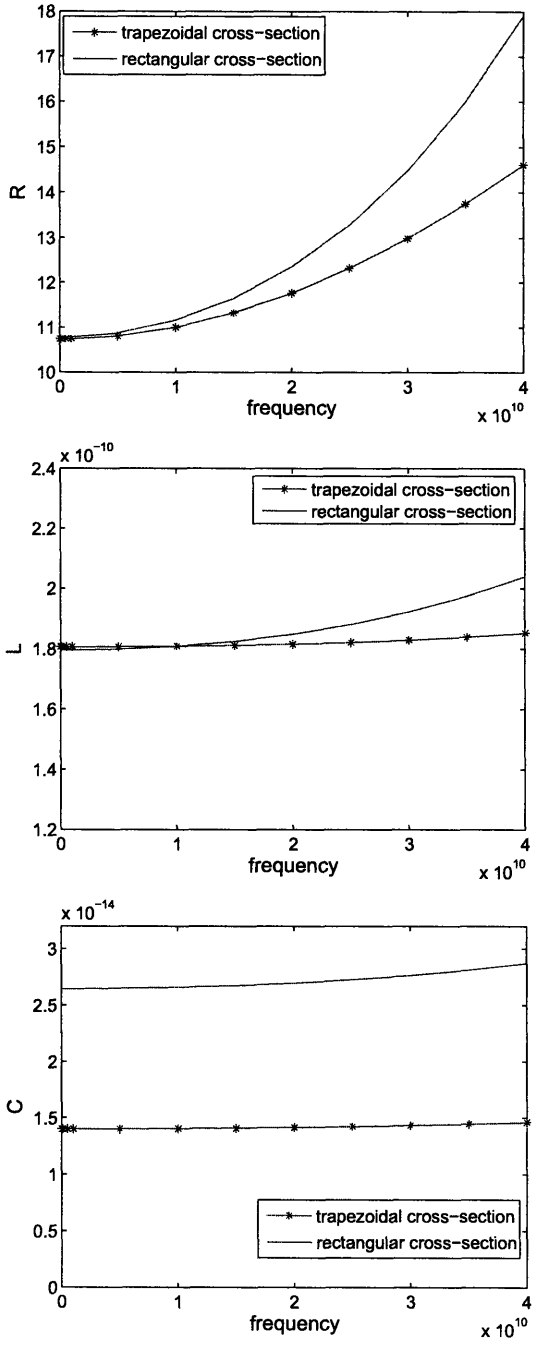

Figure 9-25: Comparisons of (a) resistance, (b) inductance and (c) capacitance between the 8-conductor array with trapezoidal cross-sections in Fig. 9-22 and the array structure in Fig. 9-24 with rectangular cross-sections.

Chapter 10

Conclusion

In this thesis, we have offered a systematic treatment on the subject of 3D full-wave interconnect impedance extractions, accounting for frequency-related effects as well as effects invoked by the presence of a planar conducting substrate. Our research effort has culminated into the practical implementation of an electromagnetic solver that contains the following innovative features:

- Incremental contribution to the existing MPIE solver through the incorporation of layered Green's functions in order to capture substrate effects. The use of these layered Green's functions obviates the necessity of explicit substrate volume or surface discretization. Using the complex image theory, we can approximate each scalar Green's function component as a series of full-wave, closed-form kernels.

- Much of the computational efficiency of this solver is obtained from the implementation of a set of accelerated integration schemes tailored to the collection of closed-form kernels derived from the application of the complex image theory. Both the 3D filament integrations and 2D panel integrations of the complex image kernels in the solver can be reduced to a sum of 1D integrals over segments contouring either the filament volumes or panel surfaces.

- In addition to system setup acceleration, further efficiency is gained at the system solve level through the implementation of specialized high-order basis functions tailored to each conductor's cross-section shape. These basis functions are frequency independent within a pre-specified range of frequency values; yet they parameterize

the frequency-dependent nature of a conductor's cross-sectional current distribution with much fewer degrees of freedom than the use of traditional basis functions. It has been conclusively shown that reducing the number of basis functions in this manner would reduce the cost of resolving near-distanced interactions by $O(n^2)$ when a pre-corrected FFT scheme coupled with an iterative solver is used to obtain the solutions.

- Furthermore, the pre-corrected FFT scheme is modified and extended in this thesis in order to accommodate the dyadic nature of the Green's function kernels encountered in the substrate modeling problem.

Bibliography

[1] M.I. Aksun. "A Robust Approach for the Derivation of Closed-Form Green's Functions." *IEEE Trans. Microwave Theory and Tech.*, Vol. 44, No. 5, May 1996.

[2] Banos, Jr. "Dipole radiation in the presence of conducting half space" Pergamon, Oxford, 1966.

[3] M. Beattie, L. Pileggi. "Inductance 101: Modeling and Extraction." *Design Automation Conference,* Las Vegas, NV, June 2001.

[4] E. Charbon, R. Gharpurey, P. Miliozzi, etc. Substrate Noise Analysis and Optimization for IC Design. *Kulwer Academic Publishers,* 2001.

[5] C. Chen, T. Lee, N.Murugesan and S. Hagness. "Generalized FDTD-ADI: An Unconditionally Stable Full-Wave Maxwell's Equations Solver for VLSI Interconnect Modeling." *Computer Aid Design,* 2000.

[6] W.C. Chew. "Waves and Fields in Inhomogeneous Media" IEEE Pr, 1995.

[7] M. Chou. *Fast Algorithms for III-Conditioned Dense-Matrix Problems in VLSI Interconnect and Substrate Modeling,* Doctoral thesis, M.I.T, 1998.

[8] Y.L. Chow, I.N. El-behery. "An Approximate Dynamic Spatial Green's Function for Microstriplines." *IEEE Trans. on Microwave Theory and Techniques,* vol MIT-26, No.12, Dec. 1978.

[9] Y.L. Chow, J.J. Yang, D.G. Fang and G.E. Howard. "A Closed-Form Spatial Green's Function for the Thick Microstrip Substrate." *IEEE Trans. Microwave Theory Tech.*, Vol. 39, No. 3, March 1991.

[10] K.M. Coperich, A.E. Ruehli, and A. Cangellaris. "Enhanced skin effect for partial-element equivalent-circuit (PEEC) models." *IEEE Trans. on Microwave Theory and Techniques,*, Vol. 48, No. 9, Sept. 2000.

[11] L. Daniel, A.Sangiovanni-Vincentelli, and J. White. "Proximity Templates for Modeling of Skin and Proximity Effects on Packages and High Frequency Interconnect." *ICCAD,* San Jose, CA, Nov. 10-14, 2002.

[12] L. Daniel, A.Sangiovanni-Vincentelli, and J. White. "Using Conduction Modes Basis Functrions for Efficient Electromagnetic Analysis of On-chip and Off-chip Interconnect." *DAC,* Las Vegas, June 18-22, 2001.

[13] L. Daniel. *Simulation and Modeling Techniques for Signal Integrity and Electromagnetic Interference on High Frequency Electronic Systems.* Doctoral thesis, University of California at Berkeley, 2003.

[14] G. Dural and M.I. Aksun. "Closed-Form Green's Functions for General Sources and Stratified Media". *IEEE Trans. Microwave Theory Tech.,* Vol. 43, No. 7, July 1995.

[15] R.W. Dutton. "The Role of TCAD in Parasitic Analysis of ICs." *Proceedings ESSDERC 1993,* pp75-81, 1993.

[16] J.Fan, J.L. Drewniak, H. Shi and J.L. Knighten. "DC Power-Bus Modeling and Design With a Mixed-Potential Integral-Equation Formulation and Circuit Extraction." *IEEE Trans. Electromagnetic Compatibility,* Vol. 43 , No. 4 , Nov. 2001.

[17] D.G. Fang, J.J. Yang, and G.Y. delisle. "Discrete Image Theory for Horizontally Electric Dipoles in a Multilayered Medium." *IEE Proc. Pt. H,* Vol. 135, No. 5, Oct. 1988.

[18] D. Gope, A. Ruehli, and V. Jandyala. "Surface-based PEEC formulation for modeling conductors and dielectrics in time and frequency domain combined circuit electromagnetic simulations." *IEEE 13th Topical Meeting on Electrical Performance of Electronic Packaging,* 2004.

[19] L. Greengard. *The Rapid Evaluation of Potential Fields in Particle Systems.* M.I.T. Press, Cambridge, Ma, 1998.

[20] R. Gharpurey and S. Hosur. "Transform Domain Techniques for Efficient Extraction of Substrate Parasitics." , 1997.

[21] T.M. Grzegorczyk. *Integrated 3D Antennas for Milimeter-wave Applications:Theoretical Study and Technological Realization* Ph.D. thesis, Ecole Polytechnique Federale De Lausanne, 2000.

[22] A.W. Glisson and D.R. Wilton. "SImple and efficient numerical methods for problems of electromagnetic radiation and scattering from surfaces." *IEEE Trans. Antennas Propagat.,* vol. AP-28, pp.593-603, Awpr. 1980.

[23] R.F. Harrington. *Field Computation by Moment Methods.* MacMillan, 1968.

[24] J.V. Hese. "Accurate Modeling of Spiral Inductors on Silicon for Wireless RF IC Designs." *TechOnLine,* Nov. 2001.

[25] F. Hilderbrand. *Introduction to Numerical Analysis.* TMH Edition, 1979.

[26] L.T. Hildebrand and D.A. McNamara. "A Guide to Implementation Aspects of the Spatial-domain Integral Equation Analysis of MicroStrip Antennas." *Appl. Comput. Electromagn. Soc. J.,* vol 10, no.1, pp. 40-51, 1995.

[27] N. Hojjat, S. Safavi-Naeini, and Y.L. Chow. "Numerical Computation of Complex Image Green's Functions for Multilayer Dielectric Meida: near-field zone and the interface region." *IEE Proc.-Microwave and Antenna Propag.*, vol. 145, no.6, Dec. 1998.

[28] N. Hojjat, S. Safavi-Naeini, R. Faraji-Dana, and Y.L. Chow. "Fast Computation of the Nonsymmetrical Components of the Green's Function for Multilayer Media using Complex Images." *IEEE Trans. Antennas Propagat.,* Vol. 145, no.4, Aug. 1998.

[29] Y. Hua and T.K. Sarkar. "Generalized Pencil-of-function method for Extracting Poles of and EM System from its Transient Response." *IEEE Trans. Antennas Propagat.*,vol. Ap-37, pp.229-234, feb.,1989.

[30] J.Huang, B. Song, J.K. White and Z. Zhu. "Improving the Robustness of a Surface Integral Formulation for Wideband Impedance Extraction of 3D Structures." *IEEE/ACM conference on computer-aided design,* San Jose, California. Nov. 4-8, 2001.

[31] E.S. Hung and S.D. Senturia. "Generating Efficient Dynamical Models for Microelectromechanical Systems from a Few Finite-Element Simulation Runs." *IEEE Journal of Microelectromechanical Sys.*, vol. 8, no.3, Sep. 1999.

[32] J.D. Jackson. *Classical Electrodynamics.* John Wiley, NY, 1975.

[33] M. Kamon, N. Marques, and J. White. "FastPep: A Fast parasitic Extraction Program for Complex Three-Dimensional Geometries." *Proc. of the IEEE Conference on Computer-Aided Design,* San Jose, Nov. 1997.

[34] M. Kamon, M.J.Tsuk and J.K. White. "FASTHENRY: a multipole-accelerated 3-d inductance extraction program." *IEEE trans. microwave theor. tech.,* vol. 42, no.9, Sept. 1994.

[35] S. Kapur and D.E. Long. "IES3: efficient electrostatic and electromagnetic simulation." *Computing in Science and Engineering,* Vol 5, no. 4, Oct.-Dec. 1998.

[36] R. Kipp and C.H. Chan. "Complex Image Method for Sources in Bounded Regions of Multilayer Structure." *IEEE Trans. on Microwave Theory and Techniques*, vol. 42, no.5, May, 1994.

[37] J.A. Kong. *Electromagnetic Wave Theory.* EMW Publishing, Cambridge, MA, 2000.

[38] H. Lan. "A CAD-Oriented Modeling Approach of Frequency-Dependent Behavior of Substrate Noise Coupling for Mixed-Signal IC Design." *Int. Symp. on Quality Electronic Design,* 2003.

[39] I.V. Lindell and E. Alanen. "Exact Image Thoery for the Sommerfeld Half-space Problem-Pt.1: Vertical Magnetic Dipole." *IEEE Trans.,* AP-32, pp.126-132, 1984.

[40] I.V. Lindell and E. Alanen. "Exact Image Thoery for the Sommerfeld Half-space Problem-Pt.2: Vertical Electric Dipole." *IEEE Trans.,* AP-32, pp.841-849, 1984.

[41] I.V. Lindell, E. Alanen, A.T. Hujanen. "Exact Image Thoery for Field Calculation in Horizontally Layered Medium above a Conducting Ground Plane." *IEE Proc. H, Microwaves, Antenna & Propag.*,pp.297-304, 1986.

[42] J.R. Long and M.A. Copeland. "The Modeling, Characterization, and Design of Monolithic Inductors for Silicon RF IC's." *IEEE Journal of Solid-state Circuits.*, Vol 32, No.3, Mar. 1997.

[43] N. Marques, M. Kamon, J.K. White, and L.M. Silverira. "A mixed nodal-mesh formulation for efficient extraction and passive reduced-order modeling of 3D interconnects." *Proc. of the IEEE/ACM DAC*, San Francisco, CA, June 1998.

[44] K.A. Michalski. "Electromagnetic Scattering and Radiation by Surfaces of Arbitrary Shape in Layered Media, Part I: Theory." *IEEE Trans. Antennas Propagat.,* Vol.38, No. 3, March 1990.

[45] K.A. Michalski and J.R. Mosig. "Multilayered Media Green's Functions in Integral Equation Formulations." *IEEE trans. Antennas Propagat.,* Vol.45, No.3, march 1997.

[46] K.W. Morton and D.F. Mayers. *Numerical Solution of Partial Differential Equations, An Introduction.* Cambridge University Press, 2005.

[47] J.R. Mosig and F. Gardiol. "A Dynamic Radiation Model for Microstrip Structures." *In P.Hawkes, Ed., Advances in Electronics and Electron Physic,* Academic Press, 1982, pp.139-247.

[48] J.R. Mosig and F. Gardiol. "Analytical and Numerical Techniques in the Green's Function Treatment of Microstrip Antennas and Scatterers." *Inst. Elect. Eng. Proc.*, (part H) 130(2):175-182.

[49] J.R. Mosig, R. C. Hall, and F.E. Gardiol. "Numerical Analysis of Microstrip Patch Antennas." *in handbook of Microstrip Antennas,*, London 1989.

[50] J.R. Mosig. "On the Calculation of Green's Functions arising in the Mixed Potential Integral Equation Formulation of Multilayered printed Antennas." *LEMA-EPFL*, May 1996.

[51] K. Nabors and J. White. "Fastcap: A multipole accelerated 3D capacitance extraction program." *IEEE Transactions on Computer-Aided Design of Integrated Circuits and Systems,* Vol.10, no. 11, Nov. 1991.

[52] A. Niknejad and R. Meyer. "Analysis, Design, and Optimization of Spiral Inductors and Transformers for Si RF IC's." *IEEE J. Solid-State Circuits,* Vol. 33, No. 10, Oct. 1998.

[53] A. T. Patera, D. V. Rovas, and L. Machiels. "Reduced-Basis Output-Bound Methods for Elliptic Partial Differential Equations" *SIAG/OPT Views-and-News,* 11:1, 4-9, 2000.

[54] J. Peters. *Design of High Quality Factor: Spiral Inductors in RF MCM-D.* Master's thesis, M.I.T., Sept. 2004.

[55] J.R. Phillips. *Rapid Solution of Potential Integral Equations in Complicated 3-dimensional Geometries.* Ph.D. thesis, M.I.T., 1997.

[56] J.R. Phillips and J.K. White. "A Precorrected-FFT Method for Electrostatic Analysis of Complicated 3D Structure." *IEEE Transactions on Computer-Aided Design of Integrated Circuits and Systems,* pg. 1059-1072, 1997.

[57] A. Rong, A.C. Cangellaris, and L. Dong. "Comprehensive Broad-Band Electromagnetic Modeling of On-Chip Interconnects With a Surface Discretization-Based Generalized PEEC Model." *IEEE Transactions on Advanced Packaging,* Vol. 28, no.3, Aug. 2005.

[58] A. Rong, and A.C. Cangellaris. "Comprehensive Broad-Band Electromagnetic Modeling of On-Chip Interconnects With a Surface Discretization-Based Generalized PEEC Model." *IEEE Transactions on Advanced Packaging,* Vol. 28, no. 3, Aug. 2005.

[59] A.E. Ruehli. "Equivalent Circuit Models for Three Dimensional Multiconductor Systems." *IEEE Trans. Microwave Theory Tech.,* Vol. 22, March 1974.

[60] A.E. Ruehli. *Circuit Analysis, Simultaion and Design.* North-Holland, 1987.

[61] A. Polycarpou. "The Finite-Element method for Modeling Circuits and Interconnects for Electronic Packaging." *IEEE Trans. Microwave Theory Tech.,* Vol. 45, No. 10, Oct. 1997.

[62] R.M. Shubair and Y.L. Chow. "A Closed-form Solution of Vertical Dipole Antennas above a Dielectric Half-space." *IEEE Trans. on Antennas and Propag,* vol. 41, no.12, Dec. 1993.

[63] T. Shibata. "Characterization of MIS Structure Coplanar Transmission Lines for Investigation of Signal Propagation in Integrated Circuits." *IEEE Trans. on Microwave Theory and Techniques,* vol. 38, No. 7. July 1990.

[64] P. Silvester. "TEM Wave Properties of Microstrip Tranmission Lines." *Proc. Inst. Elec. Eng.*, vol. 115, pp. 43-48, Jan. 1968.

[65] P. Silvester. "Modal network theory of skin effect in flat conductors." *Proc. of IEEE,* Vol 54, No. 9, Sept. 1966.

[66] T. Smede, N.P. van der Meijs, and A.J. van Genderen. "Extraction of Circuit Models for Substrate Cross-talk." ,1995.

[67] A. Sommerfeld. "Partial Differential Equations in Physics." Academic Press, NY, 1964.

[68] J.M. Song, C.C. Lu, W.C. Chew, and S.W. Lee. Fast illinois slover code (fisc). *IEEE Computational Magazine,* vol. 40, no.3, June 1998.

[69] G. Strang and G.Fix. "An Analysis of the Finite Element Method." Prentice-Hall Englewoood Cliffs, NJ, 1973.

[70] D.K. Su, et.al. "Experimental Results and Modeling Techniques for Substrate Noise in Mixed-Signal Integrated Circuits." *IEEE Journal of Solid-State Electronics*, Vol. 28, No. 8, pp.420-30, 1993.

[71] J. Tan. "Full Wave Analysis of Transmission Lines in a Multilayer Substrate with Heavy Dielectric Losses." *IEEE Trans. Components, Packaging and Manufacturing Technology,* Vol. 19, No. 3, Aug. 1996.

[72] L. Trefethen. *Numerical Linear Algebra*, SIAM, Philadelphia, 1997.

[73] M.J. Tsuk and J.A. Kong. "A hybrid method ofr the calculation of the resistance and inductance of transmission lines with arbitrary cross section." *IEEE Trans. on Microwave Theory and Techinques,* Vol 39, No. 8, Aug. 1991.

[74] B. Van der Pol. "Theory of the Reflection of the Light from a Point Source by a Finitely Conducting Flat Mirror, with an Application to Radiotelegraphy." *Physica,* Vol.2, pp. 843-853, 1935.

[75] N.K. Verghese and D.J. Allstot. "SUBTRACT: a program for the efficient evaluation of substrate parasitics in integrated circuits." *Proceedings of the 1995 IEEE/ACM international conference on Computer-aided design,* Pp. 194 - 198, California, 1995.

[76] J.R. Wait. "Electromagnetic waves in stratified media" Oxford Univ Pr, 1996.

[77] J. Wang, J. Tausch and J.K. White "A wide frequency range surface integral formulation for 3-D RLC extraction." *International Conference on Computer-Aided Design,* pp.453-457, San Jose, CA, 1999.

[78] D. Wilton, S.M. Rao, A.W. Glisson, etc. "Potential Integrals for Uniform and Linear Source Distributions on Polygonal and Polyhedral Domains." *IEEE Trans. Antennas Propagat.,* Vol. AP 32, no.3, March, 1984.

[79] A. Weisshaar, H. Lan, and A. Luoh. "Accurate Closed-form Expressions for the Frequency-Dependent Line Parameters of On-Chip Interconnects on Lossy Silicon Substrate." *IEEE Trans. on Advanced Packaging,* vol. 25, No. 2, May 2002.

[80] J.J. Yang, Y.L. Chow, D.G. Fang. "Discrete Complex Images of a Three-dimensional Dipole Above and Within a Lossy Ground." *IEE PROC-H,* Vol. 138, No. 4, Aug. 1991.

[81] H. Ymeri, B. Nauwelaers, K. Maex, S. Vandenberghe, and D. Roest. "New Analytic Expressions for Mutual Inductance and Resistance of Coupled Interconnects on Lossy Silicon Substrate." *Si Monolithic Integrated Circuits in RF Systems,* 2001.

[82] P. Yue and S. S. Wang.

[83] J. Zheng, V. Tripathi, and A. Weisshaar. "Characterization and Modeling of Multiple Coupled On-Chip Interconnects on Silicon Substrate." *IEEE Trans. Microwave Theory Tech.,* Vol. 49, No. 10, Oct. 2001.

[84] Z. Zhu, J. Huang, B. Song, J.K. White. "Algoritms in Fastimp: a Fast and Wide-band Impedance Extraction Program for Complicated 3D Structures." *Proc. of the IEEE/ACM International Conference on Computer-Aided Design,* pages 592-7, San Jose, CA, 2001.

[85] Z. Zhu. Efficient Integral Equation Based Algorithms for Parasitic Extraction of Interconnects with Smooth or Rough Surface *Ph.D. thesis,* M.I.T, August 2004.

[86] A. Zolfaghari, A. Chan and B. Razavi. "Stacked Inductors and Transformers in CMOS Technology." *IEEE Journal of Solid-state Circuits,*, Vol.36, No.4, April 2001.